STRUCTURAL, ELECTRICAL AND OPTICAL PROPERTIES OF *P*-TYPE ZNO EPITAXIAL FILMS

by

Arnold L. Allenic

A dissertation submitted in partial fulfillment
of the requirements for the degree of
Doctor of Philosophy
(Materials Science and Engineering)
in The University of Michigan
2008

Doctoral Committee:

Professor Xiaoqing Pan, Chair
Professor Richard M. Laine
Assistant Professor Jamie D. Phillips
Bing Liu, IMRA America, Inc.

© Arnold L. Allenic
All rights reserved
2008

Acknowledgements

I wish to thank my thesis advisor, Professor Xiaoqing Pan, for his mentoring, support and for the opportunities he gave me throughout this study. I would also like to thank the members of the committee, Professor Richard Laine, Professor Jamie Phillips and Dr. Bing Liu for their suggestions.

I am grateful to Dr. Yong Che and Dr. Zhendong Hu of IMRA America, Inc. for their directions and support. I am grateful to Dr. Guangyuan Zhao for sharing his vast knowledge of semiconductor science and teaching me the techniques of photoluminescence and X-ray diffraction. I am grateful to Professor Bruno Meyer, Dr. Michael Reshchikov and Dr. Joachim Sann for fruitful discussions on photoluminescence. I wish to thank Jose Azurdia for conducting thermal gravimetric analysis on my powders, Dr. Victor Rotberg for conducting nuclear reaction analysis on my nitrogen-doped ZnO samples and Dr. Steve Novak (Evans Analytical Group, Inc.) for measuring the phosphorus and nitrogen depth-profiles in my ZnO samples by secondary-ion mass spectroscopy. Finally, I wish to thank Dr. Shengbai Zhang for his suggestions and Dr. Linda Casson (Horiba Jobin-Yvon, Inc.) for her technical help with our photoluminescence system.

I would also like to acknowledge the contributions of Yanbin Chen and Dr. Haiping Sun, who imaged my samples by transmission electron microscopy (TEM), Michael Katz, who prepared the TEM specimens, Wei Guo, who assisted with growth, measurements and maintenance, Christopher Nelson, who built a data acquisition box used for electrical measurements, Weiming Wang, who fabricated mesas and Obiefune Ezekoye, who was in charge of the lab safety.

I also wish to thank Nancy Polashak for administrative assistance, Ying Qi for assistance with the XRD instruments and John Mears for assistance with machining.

Finally, I would like to acknowledge the financial supports of NSF/DMR 0308012 and IMRA America, Inc.

Table of Contents

Acknowledgements ii
List of Tables vi
List of Figures vii
List of Appendices xii
List of Constants xiii
Chapter

1. Introduction 1

2. Literature Background 7

2.1 Theoretical considerations for *p*-type doping 7
2.1.1 Candidate acceptor dopants in ZnO 7
2.1.2 Theory of doping and application to ZnO 7
2.2 Doping of ZnO 11
2.2.1 Defect chemistry of ZnO and *n*-type doping 11
2.2.2 *p*-type doping 12
2.3 Relationships between defects and physical properties of wide band gap semiconductors 14
2.4 ZnO epitaxy 16
2.4.1 Crystal structure of ZnO 16
2.4.2 Epitaxial growth 16
2.4.3 Crystal defects in wurtzite ZnO 19
2.5 Summary 20

3. Experimental Techniques 26

3.1 Epitaxial growth 26
3.1.1 Principles of thin film growth by PLD 26
3.1.2 PLD systems 28
3.1.3 Target and substrate preparation 29
3.2 Structure and microstructure characterization 29
3.2.1 X-ray diffraction 29

3.2.2 Atomic force microscopy 32
3.2.3 Transmission electron microscopy 32
3.3 Nuclear Reaction Analysis 33
3.4 Secondary-ion mass spectroscopy 34
3.5 Thermal gravimetric analysis 34
3.6 Optoelectronic properties 34
3.6.1 Spectrophotometry 34
3.6.2 Photoluminescence 35
3.6.2.1 Excitons and the near-band-edge region of the PL spectrum 35
3.6.2.2 Satellite transitions 38
3.6.2.3 Electron-phonon coupling 38
3.6.2.4 Donor-acceptor and free-to-bound transitions 39
3.6.2.5 Temperature dependence of PL transitions 40
3.6.2.6 Excitation intensity dependence of PL transitions 41
3.6.2.7 Apparatus 41
3.6.3 Hall analysis 42
3.7 Device fabrication and testing 45

4. Synthesis and Optoelectronic Properties of Nitrogen-Doped ZnO Films 55

4.1 Introduction 55
4.2 Nitrogen solubility in heteroepitaxial ZnO films 57
4.3 Effect of nitrogen doping on the optoelectronic properties of ZnO 57
4.4 Effect of nitrogen doping on the crystallinity and microstructure of ZnO 61
4.5 Conclusions 63

5. Microstructures and Optoelectronic Properties of Phosphorus-Doped ZnO Films 72

5.1 Introduction 72
5.2 Heteroepitaxial growth of P-doped ZnO on (0001) Al_2O_3 73
5.2.1 Introduction 73
5.2.2 Effect of phosphorus on the optoelectronic properties of ZnO 74
5.2.3 Temperature dependence of the phosphorus solubility 78
5.2.4 Effect of phosphorus on the crystallinity and microstructure of ZnO 78
5.2.5 Microscopic origin of *p*-type conduction in P-doped

ZnO 80
5.3 Homoepitaxial growth of P-doped ZnO on (0001) ZnO 82
5.3.1 Introduction 82
5.3.2 Results and discussion 82
5.3.3 Generalization of the model for *p*-type conduction in P-doped ZnO. 85
5.4 Effect of oxygen plasma on the optoelectronic properties of P-doped ZnO 85
5.4.1 Introduction 85
5.4.2 Results and discussion 86
5.5 Conclusions 89

6. Fabrication of ZnO-Based *p-n* and *p-i-n* Homojunctions 114

6.1 Introduction 114
6.2 ZnO substrates 115
6.3 Homojunction fabrication 117
6.4 Issues pertaining to electroluminescence 119
6.5 Conclusions 120

7. Thesis Conclusions 129

7.1 Effect of doping on the microstructure of ZnO 129
7.2 Effect of doping on the optoelectronic properties of ZnO 130
7.3 Impact of this work 130

8. Future Work Recommendations 132

8.1 Band gap engineering in the low doping limit 132
8.2 Epitaxial growth on alternative substrates for increased functionality 133
8.2.1 Epitaxy in non-polar directions 133
8.2.2 Epitaxy on YSZ and Si 133

Appendices 135

Bibliography 140

List of Tables

Table

2.1 Ionic radii and size mismatches ($\varsigma = r_{dopant} / r_{host} - 1$) with host atoms of potential acceptor dopants in ZnO. The ionic radii correspond to a coordination number of 4. The elements in italic introduce acceptors upon substitution of the host element in bold 21

2.2 Possible substrates/templates for ZnO epitaxy and their in-plane lattice mismatches 22

3.1 Dependences of various undesired voltages on current polarity and magnetic field orientation 46

4.1 Room-temperature electrical properties of undoped and N-doped ZnO films before and after annealing in O_2 at 600 °C. Each sample is 0.5 μm-thick 64

5.1 Room-temperature electrical properties of undoped and P-doped ZnO films before and after annealing in O_2 at 600 °C. Each sample is 0.5 μm-thick 90

5.2 Tilt angle, twist angle, and densities of threading dislocations in undoped ZnO, *n*-type PZO, and *p*-type PZO 91

5.3 Comparison of X-ray diffraction rocking curve half-widths and biaxial strains in *p*-type heteroepitaxial and homoepitaxial films 92

5.4 Electrical properties at room temperature of *n*-type and *p*-type heteroepitaxial and homoepitaxial PZO films. 93

5.5 Electrical properties at room temperature of undoped ZnO and P-doped ZnO films grown by oxygen plasma-assisted PLD. The film thickness is ~1 μm and the anneal temperature is 900 °C 94

5.6 Effect of the phosphorus concentration on the energy position, energy shift, intensity of the DA transition and on the activation energy of the acceptor 95

6.1 Electrical properties at room temperature of the ZnO substrates 121

List of Figures

Figure

1.1 Schematic illustration of a multi-layered *p-i-n* homojunction structure for optical device applications and challenges behind the growth of each layer 5

1.2 The exciton binding energy as a function of the band gap energy for compound semiconductors. Reproduced from Klingshirn, "Semiconductor Optics", page 166 6

2.1 Illustration of the doping asymmetry in ZnO, according to Ref. 54 and 57 23

2.2 Ball and stick model of the wurtzite structure 24

2.3 Wurtzite structure and application of the Thompson tetrahedron to the hexagonal close-packed lattice of ZnO. Only the Zn layers are represented 25

3.1 Illustration of the tilt and twist distributions for a mosaic ZnO film grown on (0001) Al_2O_3 47

3.2 Illustration of the (a) symmetric, (b) glancing incidence asymmetric and (c) skew symmetric XRD geometries 48

3.3 Hexagonal wurtzite structure viewed along (a) $[11\bar{2}0]_{ZnO}$ and (b) $[10\bar{1}0]_{ZnO}$ ... 49

3.4 Band diagram illustrating the radiative transitions of interest in this work 50

3.5 Illustration of excitons bound to (a) an ionized donor D^+, (b) a neutral donor D and (c) a neutral acceptor A 51

3.6 Intensity distributions of phonons assuming Huang-Rhys factors of (a) 0.5, (b) 1, (c) 5 and (d) 10 52

3.7 Van der Pauw geometry used for (a) conductivity and (b) Hall voltage measurements 53

3.8 (a) Theoretical Hall mobility in bulk ZnO assuming $n(300)=10^{15}$ cm^{-3}, $N_A=10^{14}$ cm^{-3}, $N_{DIS}=10^4$ cm^{-2} , and a two-donor and one-acceptor model to fit the charge balance equation. The five scattering mobility components used in this work

are also represented. (b) Effect of increasing dislocation density $N_{DIS}=10^{\alpha}$ cm^{-2} on the total Hall mobility 54

4.1 (a) Thermal gravimetric analysis of Zn_3N_2 powder in air and nitrogen atmospheres. (b) Temperature-dependent X-ray diffraction measurements conducted in air. The (i), (ii), (iii) and (iv) traces correspond to Zn_3N_2 powder annealed at 500 °C, 550 °C, 650 °C and 750 °C respectively 65

4.2 (a) Secondary-ion mass spectroscopy of nitrogen in a 500 nm-thick *p*-type nitrogen-doped ZnO fabricated at 300 °C. (b) Dependence of the nitrogen solubility in ZnO (open squares) and film crystallinity (circles) on the growth temperature, according to NRA and 0002 ZnO rocking curve measurements. The experimental error intrinsic to the NRA measurement is about 10%. 66

4.3 (a) Temperature dependences of the carrier concentration in *n*-type (squares) and *p*-type (circles) nitrogen-doped samples. The least-squares fit to the hole concentration in *p*-type ZnO yields E_A=105±5 meV. (b) Temperature dependences of the Hall mobilities. (c) Fit to the Hall mobility of a *p*-type sample using the Petritz model. The experimental error in these measurements is 7 % 67

4.4 Photoluminescence spectra at 6 K of (a) undoped ZnO, (b) *n*-type nitrogen-doped ZnO and (c) *p*-type nitrogen-doped ZnO fabricated at 300 °C. Note the DA transitions at 377.3 nm and 396.0 nm in the *p*-type film 68

4.5 (a) Symmetric XRD θ-2θ scan and (b) asymmetric $11\bar{2}4$ ϕ-scan of a nitrogen-doped ZnO sample deposited at 300 °C. All nitrogen-doped films grow epitaxially on the (0001) Al_2O_3 substrate in one step, contrary to other processes, which rely on the oxidation of as-deposited Zn_3N_2 films 69

4.6 Schematic drawing of the epitaxial orientation relationship between ZnO and the (0001) Al_2O_3 substrate 70

4.7 Bright-field low-magnification TEM images of (a) *p*-type nitrogen-doped ZnO fabricated at 300 °C and (b) *n*-type nitrogen-doped ZnO fabricated at 400 °C. Note the columnar grain microstructure of the *p*-type sample 71

5.1 (a) Resistivity, (b) Hall mobility and (c) carrier concentration at room temperature of various ZnO films as a function of the phosphorus concentration in the P_2O_5-doped ZnO sputtering target. The triangles correspond to T_G=800 °C, the circles to T_G=600 °C and the squares to T_G=600 °C, followed by annealing at T_A=600 °C. The arrows point to the *p*-type samples. (d) Field-dependent measurement of the Hall coefficient in *p*-type PZO deposited at T_G=600 °C and annealed at T_A=600 °C 96

5.2 Temperature dependences of the (a) conductivity, (b) Hall mobility and (c) carrier concentration of different ZnO films. The triangles, circles and squares

correspond to *p*-type PZO, *n*-type PZO and undoped ZnO respectively. (d) Fit to the charge balance equation for a *p*-type PZO heteroepitaxial film giving an acceptor activation energy of 120 meV 97

5.3 Transmittance spectrum at room temperature of a 2 μm-thick *p*-type PZO sample 98

5.4 PL spectra at 6 K of (i) *n*-type PZO grown at 800 °C, (ii) undoped ZnO grown at 600 °C, (iii) as-grown PZO at 600 °C, and (iv) *p*-type PZO grown at 600 °C. (b) Temperature dependence of the integrated intensity of the 371.5 nm transition. The circles are the experimental data and the solid line is the fit 99

5.5 Secondary-ion mass spectroscopy of phosphorus in heteroepitaxial PZO films grown at (i) 600 °C and (ii) 800 °C 100

5.6 (a) Typical θ-2θ scan of PZO films grown on (0001) Al_2O_3. (b) Corresponding $11\bar{2}4$ ZnO ϕ-scan showing the 6-fold symmetry of the wurtzite structure and the absence of rotation domains in PZO. (c) 0002 and (d) $10\bar{1}2$ ω-scans of heteroepitaxial PZO films grown at 600 °C (broad traces) and 800 °C (narrow traces) 101

5.7 TEM images of (a) undoped ZnO grown at 600 °C, (b) *n*-type PZO grown at 800 °C, and (c) *p*-type PZO grown at 600 °C. Note that the dislocation density increases with the increase of phosphorus doping 102

5.8 (a) HRTEM image showing the atomic structure of the interface between the PZO film grown at 600 °C and the sapphire substrate. (b) HRTEM image showing the existence of partial dislocations associated with nano-sized stacking faults in the 0001 plane of *p*-type PZO. (c) Interstitial dislocation loop and (d) corresponding simulation using a ball and stick model 103

5.9 Illustration of the formation mechanism of the P_{Zn}-$2V_{Zn}$ complex in ZnO using a ball and stick model. In (a) a perfect ZnO lattice with 4 basal double layers represented, (b) the formation of a phosphorus antisite is accompanied with the formation of two zinc vacancies and (c) a rearrangement of bond lengths around the antisite. See Ref. 33 for more details 104

5.10 Secondary ion mass spectroscopy of phosphorus in *p*-type homoepitaxial PZO 105

5.11 0002 θ-2θ X-ray diffraction pattern of *p*-type homoepitaxial PZO 106

5.12 (a) TEM image of *p*-type homoepitaxial PZO highlighting a high density of short segments of stacking faults. (b) High-resolution micrograph showing the atomic structure of a pair of partial dislocations belonging to a dislocation loop.... 107

5.13 Temperature dependences of (a) the carrier concentration and (b) the Hall mobility of homoepitaxial PZO films before annealing (triangles) and after annealing in O_2 (circles) 108

5.14 PL spectra at 12.5 K of (i) bulk ZnO, (ii) heteroepitaxial ZnO deposited on (0001) sapphire, (iii) *p*-type homoepitaxial PZO and (iv) *p*-type heteroepitaxial PZO. The comparison shows that the crystal defects induced by phosphorus doping quench the film near-band-edge luminescence 109

5.15 PL spectra at 12.5 K of undoped and P-doped ZnO, showing the existence of a violet luminescence band at 3.1099 eV in the P-doped sample grown by oxygen plasma-assisted pulsed laser deposition 110

5.16 (a) Integrated intensity of the DA transition as a function of the laser excitation intensity. The triangles are the experimental data points and the solid line is the fit using a power law. (b) Energy shift of the DA transition as a function of the excitation intensity. (c) Power dependence of the DA transition on the phosphorus concentration. The triangles are the experimental data points and the solid line is the fit using a power law 111

5.17 Temperature dependence of the DA transition. The triangles are the experimental data points and the lines are the corresponding fits using two Arrhenius processes 112

5.18 Evolution of the luminescence of P-doped ZnO as a function of the annealing temperature T_A. The violet band is entirely quenched at 900 °C 113

6.1 0002 ω-scans of the (a) S_1, (b) S_2 and (c) S_3 ZnO crystals. Note the large miscut in S_3 and the existence of low tilt angle boundaries 122

6.2 2×2 μm^2 AFM scans of the as-received surfaces of the (a) S_1, (b) S_2 and (c) S_3 ZnO crystals. The Z-height is 5 nm 123

6.3 Comparison of the NBE photoluminescence at 10 K of the ZnO substrates. Note the broader excitonic transitions and the higher background level in S_3 124

6.4 (a) Comparison between the I-V curves of *p-n* junctions grown on sapphire (dashed line) and ZnO (solid line). (b) I-V characteristics of a) Ti/Au contacts to the bottom *n*-type PZO layer and b) Ni/Au contacts to the top *p*-type PZO layer. c), d) and e) The rectifying I-V characteristics of the corresponding *p-n* homojunction measured over a period of eight months 125

6.5 Depletion width of the *p*-type layer as a function of the electron concentration in the *n*-type layer. In this work, the electron concentration of the *n*-type layer is at least 5×10^{18} cm^{-3} 126

6.6 (a) Cross-sectional illustration of the ZnO-based *p-n* homojunction. (b) Top-view of the mesa device. The outer ring provides two bonding pads for bottom contacting while the inner rings contacts on the *p*-type layer 127

6.7 NBE photoluminescence spectra at 300 K of the *p*-type layer grown on top of the device (solid curve) and of undoped ZnO grown on a ZnO substrate (dotted curve) 128

List of Appendices

Appendix

A Lattice parameters and epilayer strain analysis using asymmetric XRD measurements 135

B Scattering theory in ZnO epitaxial films 138

List of Constants

Fundamental constants

Avogadro number	N_A=6.02×10^{23} mol^{-1}
Bohr radius of the hydrogen atom	a_B=0.053 nm
Boltzmann's constant	k=8.6×10^{-5} eV·K^{-1}
Electron charge	e=1.6×10^{-19} C
Electron mass	m_o=9.1×10^{-31} kg
Permittivity of vacuum	ε_o=8.85×10^{-12} F·m^{-1}
Planck's constant	h=6.626×10^{-34} J·s
Reduced Planck's constant	$\hbar$=1.055×10^{-34} J·s
Rydberg energy of the hydrogen atom	R_y=13.6 eV

ZnO constants

Atomic mass	M =81.4 g·mol^{-1}
Debye temperature	T_o=837 K
Deformation potential	E_1=15 eV
Density	ρ=5.6×10^{3} kg·m^{-3}
Effective density of states in the conduction band	$N_c^{'}$=5.75×10^{20} m^{-3}
Effective density of states in the valence band	$N_v^{'}$=2.22×10^{21} m^{-3}
Electron effective mass	m_e^*=0.24×m_o kg
Hole effective mass	m_h^*=0.59×m_o kg
Infinite dielectric constant	ε_∞=3.75
Lattice parameters	a_{ZnO}=3.24982×10^{-10} m
	c_{ZnO}=5.20661×10^{-10} m
Occupied degeneracy factor (n-type)	g_1^n=2
Occupied degeneracy factor (p-type)	g_1^p=4
Piezoelectric coupling coefficient	P=0.21
Static dielectric constant	ε_s=8.75
Thermal expansion coefficient	α_{ZnO}^a= 6.5×10^{-6} K^{-1}
Unoccupied degeneracy factor (n-type)	g_0^n=1
Unoccupied degeneracy factor (p-type)	g_0^p=1

Velocity of sound	s=6.59×10^{3} m·s^{-1}

Other constants used in this work

Lattice parameters of Al_2O_3	$a_{Al_2O_3}$ =4.758×10^{-10} m
	$c_{Al_2O_3}$ =12.991×10^{-10} m
Thermal expansion coefficient of Al_2O_3	$\alpha^{a}_{Al_2O_3}$ =7.5×10^{-6} K^{-1}

Chapter 1

Introduction

The twenty-first century will see lighting technologies change dramatically. By 2025, fluorescent and incandescent illumination sources should be replaced by more efficient, long-lasting and versatile light sources offering more lumens per dollar, Watt, cm^2, and decreasing the consumption of energy for lighting by 29 %.[1] The core of such solid-state lighting device, illustrated in Fig. 1.1 in its simplest form, is a *p-i-n* junction, a relatively simple multilayered device formed by wide gap semiconductors, that emits light when an electric current is passed through it.

In the past decades, research in optoelectronics focused on the crystal growth and conductivity control of semiconductors such as SiC,[2] II-VI chalcogenides,[3] III-V compound semiconductors[4] and II-VI metal oxides.[5] Despite the successful fabrication of a SiC blue light-emitting diode (LED) and considerable research efforts devoted to the fabrication of *p*-type ZnSe and II-VI blue-green lasers, these two semiconductors were rapidly outshined by the superior electronic properties and light emission efficiency of nitride-based thin-film devices.[6] While Hall mobilities as high as 200 $cm^2/V\cdot s$ at 300 K were already achieved in undoped GaN/Al_2O_3,[7] AlN and GaN low-temperature buffer layers were developed to accommodate the large lattice and thermal expansion coefficient mismatches between nitride layers and sapphire substrates,[8,9] resulting in improved epilayer mobilities (600 $cm^2/V\cdot s$ at 300 K). Furthermore, the external quantum efficiency of nitride-based dies emitting in the blue was found to surpass that of SiC emitters (41% for non-polar InGaN/GaN LEDs vs. 0.03% for SiC LEDs).[2,10] Equally critical to the success of III-V nitrides was the achievement of stable *p*-type behavior and low resistivity (2 $\Omega\cdot$cm) in GaN layers doped with Mg.[11] These breakthroughs made

possible the fabrication of small size, high-brightness blue light-emitting devices and laser diodes.[12]

These devices find applications in high-storage capacity optical recording medias (e.g. blue-ray discs). There is also a large potential in lighting and illumination such as traffic signals, automobile interior panel lighting, but also high-resolution printers, video game consoles, ophtalmics and biophotonics.[13] In addition to light emitters, ultraviolet detectors are also needed to monitor the intensity of the radiation reaching the Earth and prevent skin cancer.[14]

In parallel with nitrides, oxide semiconductors continue to receive considerable attention due to their low cost of fabrication, chemical robustness and high thermal conductance.[5] Transparent conducting oxides such as Sn-doped In_2O_3 (ITO), Sb-doped SnO_2 (NESA), F-doped SnO_2 and Al-doped ZnO are usually fabricated on transparent substrates such as glass or sapphire.[15,16] These semiconductors are always *n*-type with a resistivity of 10^{-4}-10^{-5} Ω·cm and are widely used as transparent electrodes in thin film transistors, organic light-emitting diodes and solar cells. The lack of transparent *p*-type oxide material has always been a major obstacle to the fabrication of oxide-based *p-n* junctions such as those shown in Fig. 1.1.

ZnO is a II-VI transparent conducting oxide touted as a material of choice for short-wavelength optoelectronics. Similar to GaN, ZnO has a direct band gap of 3.37 eV at 300 K that can be engineered via dilute alloying with BeO,[17] MgO[18] and CdO,[19] while retaining the ZnO crystallographic structure. As shown in Fig. 1.2, the more tightly bound exciton in ZnO (59 meV) compared with other compound semiconductors (30 meV for GaN) opens the possibility for ZnO-based optical devices to operate well above 300 K (26 meV). Lasing in optically pumped ZnO has already been demonstrated at 300 K in high-quality epilayers[20-22], polycrystalline films (so-called "random lasers),[23] quantum well superlattices[24] and nanowire arrays.[25] Besides its suitable properties for optical applications, the attractiveness of ZnO also lies in its breakdown strength (on the order of 10-600 kV/cm depending on the varistor geometry),[26] high saturation velocity (3×10^7 cm/s for a 250 kV/cm field strength)[27] and bulk electron mobility[28] (~200 $cm^2/V\cdot s$ at 300 K). Furthermore, ZnO shows electron and proton radiation hardness capabilities, of potential use in high-irradiation conditions such as space-based environments.[29]

Finally, despite persisting issues of conductivity control,[30] group-I impurity self-diffusion and surface readiness for homoepitaxial growth,[31] ZnO single crystals are now commercially available with a "crystallinity-to-cost" ratio that strongly depends on the manufacturers.

ZnO and its ternary alloys have the potential to compete with III-V nitrides for optoelectronic applications. However, the fabrication of optical devices still suffers from the lack of *p*-type ZnO. The quest for stable, *p*-type ZnO is a challenging one because the electronic and optical properties of ZnO are very sensitive to minute concentrations of dopants, impurities, and to microscopic perturbations of the lattice.[32] It will be explained in chapter 2 that the reasons for the difficulties to dope ZnO *p*-type come from its asymmetric defect chemistry, ionicity, and the complex roles of impurities and crystal defects. Various acceptors and doping methods have been tested to achieve *p*-type conductivity. Though doping is known to induce point and extended defects in ZnO, there are few studies of the formation mechanisms and characterization of these defects, and of their effects on the epilayer macroscopic properties. Yet, the role of crystal defects in ZnO is a subject of considerable interest because the realization of good *p*-type conductivity will require an understanding of the interactions between acceptors and crystal defects, either native or doping-induced.

The objectives of this thesis are: (1) to synthesize stable *p*-type ZnO epitaxial films and achieve conductivity control; (2) to study the electrical and optical properties of the ZnO films; (3) to characterize the nature and formation mechanisms of crystal defects in order to understand and model the effects of doping on the microstructure and optoelectronic properties of *p*-type films; (4) to explore potential LED structures employing the *p*-type ZnO material developed in the fifth chapter of this thesis.

The thesis is outlined as follows: in chapter 2, theoretical considerations related to *p*-type doping of ZnO are presented and the role of defects on the macroscopic properties of wide band gap semiconductors such as ZnSe and GaN is surveyed. The crystal structure of ZnO and the crystal defects in ZnO are introduced. Chapter 3 deals with the experimental section of this thesis. In chapter 4, the microstructure and optoelectronic properties of *p*-type nitrogen-doped ZnO films fabricated by a new process are studied. In chapter 5, recent theoretical predictions[33] of the effect of phosphorus in ZnO are tested

and a model explaining the origin of *p*-type conductivity in heteroepitaxial and homoepitaxial phosphorus-doped ZnO films is proposed. In an effort to address the role of the chemical potential of oxygen and improve the luminescence yield of the layers, the effects of O_2 plasma used during growth on the optical properties of phosphorus-doped ZnO is also studied. In chapter 6, the synthesis of ZnO *p-n* homojunctions using the *p*-type material developed in chapter 5 is presented and some issues pertaining to electroluminescence are discussed. The main results of this work are summarized in the conclusion. A short chapter with future work recommendations concludes the thesis.

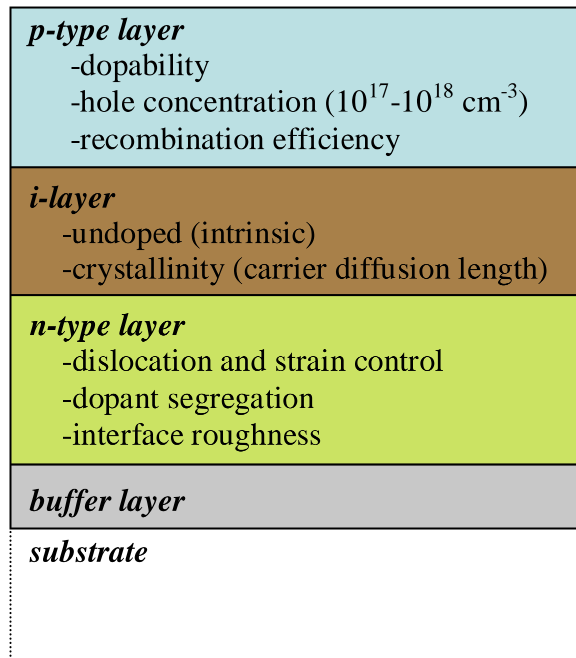

Figure 1.1 Schematic illustration of a multilayered *p*-*i*-*n* homojunction structure for optical device applications and challenges behind the growth of each layer.

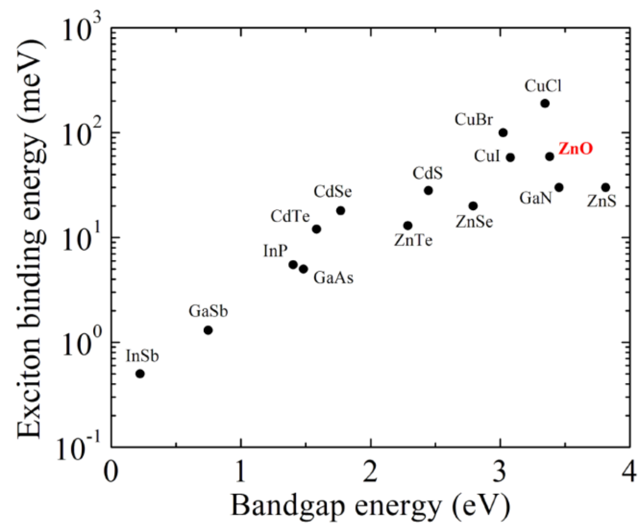

Figure 1.2 The exciton binding energy as a function of the band gap energy for compound semiconductors. Reproduced from Klingshirn, “Semiconductor Optics”, page 166.

Chapter 2

Literature Background

2.1 Theoretical considerations for *p*-type doping

2.1.1 Candidate acceptor dopants in ZnO

Candidate acceptors in ZnO are group-I elements (Li and Na) and group-V elements (N, P, As, Sb). Their ionic radii[34] and size mismatches with host elements are listed in Table 2.1.

The probability of substitution of a dopant in a lattice can be *predicted* by examining its size mismatch with the host atom, in analogy with the Hume-Rothery rules for metals.[35] Large-size dopants are unlikely to form substitutionals when there is appreciable elastic strain energy. N_O and Li_{Zn} substitutionals are theoretically the *best* candidate acceptor dopants. Other possible acceptor dopants include P, As, Sb and Bi on the oxygen site, Na on the zinc site but the size factor is very unfavorable. Note that the size mismatch of group-V antisites is relatively small. Besides substitutionals, dopants can be incorporated in the ZnO lattice in alternate forms such as complexes, as described in section 2.2.2.

2.1.2 Theory of doping and application to ZnO

The future technological importance of ZnO will depend on the ability to dope it *n*-type and *p*-type. For optical device applications, there is a need to fabricate stable *p*-type ZnO materials with hole concentrations in the 10^{17}-10^{18} cm^{-3} range. Yet, like in most III-V and II-VI compound semiconductors, obtaining *p*-type conductivity in ZnO is very difficult. ZnO,[36] ZnSe,[3] ZnS,[37] CdS,[38] GaN[39] and other oxides[40] are strong *n*-type conductors but are difficult to dope *p*-type. In contrast ZnTe can only be doped *p*-type.[41] CdTe is the only II-VI compound that can be doped *n*-type and *p*-type relatively easily.[42]

Practically, the challenges are to minimize the effect of compensation, enhance the solubility and ionization ratio of a shallow acceptor and minimize the density of defects in order to achieve desirable optoelectronic properties of practical use.[43] In the following paragraphs, important concepts such as dopant solubility, dopant activation, self- or doping induced compensation, passivation, unintentional doping, lattice instabilities and Fermi level pinning are discussed. Their influence on the *p*-type doping of ZnO is explained.

Stoichiometric wide gap semiconductors are electrical insulators. Conductivity is promoted extrinsically by the incorporation of dopants and impurities.[44] How the dopant incorporates the host determines the level of conductivity that can be achieved. The dopability of a semiconductor is usually limited by the dopant solubility.[45] The dopant solubility depends on the formation energy of the defect it forms, which is determined by the chemical potentials of the dopant and elements forming the lattice. A low solubility may result from the formation of a secondary phase at high doping levels, segregation, precipitation or substitution at the wrong lattice site. Doping methods such as co-doping and cluster-doping have emerged in the last few years to address the issue of low acceptor dopant solubility in ZnO.[46] Briefly, the intentional introduction of donors and acceptors in a specific ratio can enhance the acceptor solubility by minimizing the ionic potentials and lowering the Madelung energy (electrostatic energy of an ionic crystal given by the sum of pairwise interactions between ions treated as point charges). These methods predict that the issue of low acceptor solubility in ZnO can be overcome by introducing donors, which will lower both the lattice energy and the acceptor defect formation energy.

Yet, when the dopant is soluble, it may form a deep level that is not ionizable at room temperature. Deep levels increase the film resistivity and are sometimes responsible for photo- or hopping conduction.[47] If the dopant is shallow, the free carriers it produces may be compensated by oppositely charged defects or complexes.[48,49] Or, the shallow donor D (resp. acceptor A) may have a metastable geometric configuration and transform into a more stable but deeper level. If this happens upon binding with a point defect X, the resulting deep center is called a DX (resp. AX) center.[50]

Compensation in II-VI semiconductors has been widely studied and has several origins:[48-51] self-compensation by native defects, compensation by crystal defects induced by doping and compensation by extrinsic electron sources such as O-H complexes[65] or unintentional defects such as group-V antisites.

The formation energy of a neutral defect substituting to a host atom *at equilibrium* is defined as:[52]

$$E^{o} = E(lattice + defects) - E(lattice) + \sum_{i} \varepsilon_i \mu_i \qquad (2.1)$$

where μ_i is the chemical potential of element i and ε_i is positive if the atom is removed and negative if it is added to the lattice. For example, Eq. (2.1) predicts different evolutions of μ_P as a function of μ_O depending on whether P_2O_5 or Zn_3P_2 is used to dope ZnO with phosphorus.

The energy corresponding to the ionization of the defect to an excited state of charge q is equal to:

$$E^{q} = E^{o} + qE_F \qquad (2.2)$$

where E_F is the Fermi level energy.

For a donor D of charge $+q$, the activation reaction corresponds to:

$$D \rightarrow D^{q+} + qe^{-} \qquad (2.3)$$

For an acceptor A of charge $-q$, the activation reaction corresponds to:

$$A^{q-} + qh^{+} \rightarrow A \qquad (2.4)$$

In order to dope ZnO *p*-type, Fermi statistics requires that the energy barrier between the Fermi level and the valence band edge be as small as possible.[53] As the Fermi level energy decreases, the formation energy of native donors (q>0) decreases according to Eq. (2.2) and it becomes energetically favorable for the system to spontaneously form native donor defects (hole killers) that will annihilate holes created by the acceptor. The same reasoning is true with *n*-type doping. Therefore, there exists a maximum free carrier concentration in donor-doped or acceptor-doped ZnO, as a result of the spontaneous formation of oppositely charged defects driven by the minimization of the energy barrier between the Fermi level and the band edge. The Fermi level energy at which the free carrier concentration reaches a maximum is called the pinning energy.

The doping limit rule does not explain the asymmetry of ZnO or that of other II-VI compounds. More detailed studies have related the doping asymmetry to the relative positions of the pinning energies of the Fermi levels with respect to the band edges. A material for which the *n*-type (resp. *p*-type) pinning energy is much smaller (resp. larger) than the energy of the conduction (resp. valence) band edge cannot be doped *n*-type (resp. *p*-type).[54] Since the position of the Fermi level determines the spontaneous formation of compensating defects, there exists a theoretical maximum free carrier concentration. The rule is based on the fact that band-edge discontinuities in heterojunctions formed between doped semiconductors can be predicted.[55] In fact, the doping limit rule can be viewed as an extension to wide band gap semiconductors of the vacuum pinning rule, which was originally established by Walukiewicz for transition-metal-doped semiconductors.[56] Figure 2.1 is an illustration of the band structure of ZnO.[54,57] The pinning energies of the Fermi level for *n*-type and *p*-type doping are represented by the dashed lines. In ZnO, the *p*-type pinning energy $\varepsilon_F^{p,pin}$ was initially predicted to be around 1.5 eV above the valence band edge (E_V), suggesting that ZnO cannot be doped *p*-type at equilibrium.[54] However, recent calculations showed that the *p*-type pinning energy lies 0.1 eV inside the valence band.[57] The conduction band edge (E_C) is located about 1.3 eV below the *n*-type pinning energy $\varepsilon_F^{n,pin}$, therefore ZnO can be heavily doped *n*-type (degenerate semiconductor), in agreement with experimental results.

These theoretical considerations illustrate the major challenges behind *p*-type doping of ZnO: issues of low dopant solubility, hole compensation, deep level formation and acceptor ionization have to be experimentally addressed. In addition, an understanding of the dependence of these mechanisms on the process parameters is crucial. Chances to achieve *p*-type doping can be improved by designing growth conditions that destabilize the formation of compensating centers. These issues are addressed in chapter 4 for nitrogen-doped ZnO and in chapter 5 for phosphorus-doped ZnO films.

2.2 Doping of ZnO

2.2.1 Defect chemistry of ZnO and *n*-type doping

The epilayer conductivity type depends on the concentration and activity of native point defects and unintentional impurities. In this section, the intrinsic defect chemistry of ZnO is reviewed.

Zhang *et al.* reported that ZnO is intrinsically *n*-type under zinc-rich conditions.[36] Temperature-dependent Hall measurements have shown that zinc interstitials (Zn_i) are one of the three principal donor types in bulk ZnO crystals.[28] Recent reports have shown that the Zn_i-N_O complex (with a 0.9 eV binding energy) could be the most abundant donor in ZnO.[58] This complex forms because zinc interstitials are mobile at room temperature[59] and likely have to form complexes in order to become stable. Isolated oxygen vacancies (V_O), in contrast, form deep gap states.[36] Kohan *et al.* predicted that oxygen vacancies are the most abundant donors in ZnO[60], though neither zinc interstitials nor oxygen vacancies exhibit characteristics consistent with the high electron concentrations observed in undoped ZnO. A recent comprehensive study by Janotti *et al.* supports Kohan's predictions that native point defects in ZnO are very unlikely to be the cause of unintentional *n*-type conductivity.[61] Note that recent reports correlate the 3.366 eV photoluminescence (PL) transition (known as I_3, see section 3.6.2.1) with Zn interstitials.[62]

While hydrogen is known to systematically compensate the dominant carriers in GaN,[63] hydrogen is always a shallow donor in ZnO according to Van de Walle[64] and forms donor O-H complexes.[65] Recent calculations support[66] and question[67] the fact that hydrogen sitting in oxygen vacancies can form strong multicenter bonds responsible for the *n*-type conductivity observed in ZnO. It is however accepted that hydrogen electrically passivates nitrogen acceptors[68] and enhances their solubility in ZnO by forming N_O-H_i complexes which have formation energies smaller than that of the nitrogen acceptor alone.[69] The PL signature of hydrogen at 3.3628 eV (known as I_4) disappears after annealing in N_2 at 850 °C.[70] Hydrogen contamination is significant in organo-metallic vapor phase epitaxy,[68] yet there is little evidence that it is an issue in pulsed laser deposition.

The concentration of background donors and acceptors in ZnO crystals and epilayers depends on the growth conditions and on the purity of the starting materials. The reduction of donor defects is a major challenge that has been underestimated because of the drive to produce *p*-type ZnO. With the control of impurities and the reduction of the defect concentration via the growth on high-temperature annealed buffer (HITAB) layers, ZnO epitaxial films have very high mobilities (440 $cm^2/V\cdot s$) at room temperature,[71] surpassing the highest values achieved for bulk crystals (~200 $cm^2/V\cdot s$).

Conductive ($\sigma=10^4$-10^5 $S\cdot cm^{-1}$) and transparent *n*-type ZnO can be obtained via substitutional doping of group-III elements (Al, Ga, In) to the zinc site.[5,16,72] Al-doped ZnO is a transparent conducting oxide widely used to replace ITO and NESA. However, for ZnO *p-n* homojunction applications, doping with Ga is preferred[73,74] because the diffusivity of Ga in ZnO is smaller than that of Al. Note that Ga and Al impurities, commonly found in commercial sources, are also a source of unintentional *n*-type conductivity in ZnO. The photoluminescence fingerprints of the Al, Ga and In donors in ZnO are known as I_{6a}, I_8 and I_9 respectively.[70]

The zinc vacancy is a shallow acceptor that prevails in materials grown under oxygen-rich conditions.[75] It is electrically compensated by hole killers (V_O and Zn_i) that form readily under both zinc-rich and oxygen-rich conditions. Tuomisto *et al.* have shown evidence using positron annihilation spectroscopy that the zinc vacancy is an abundant acceptor in undoped ZnO material.[76] It will be shown in chapter 5 that zinc vacancies complex with other defects to stabilize shallow acceptors and that P-doping favors the formation of zinc vacancies under oxygen-rich growth conditions.

2.2.2. *p*-type doping

Lithium is amphoteric in ZnO and forms substitutionals to the zinc sites (acceptors) and interstitials (donors).[77] Its thermal instability favors electron compensation in hydrothermally grown ZnO material, resulting in semi-insulating layers or substrates.[30,78,79] This is a major obstacle to the realization of *p*-type conductivity in homoepitaxial layers fabricated on Li-containing substrates such as hydrothermally-grown ZnO substrates.

Nitrogen has a small ionic radius mismatch with oxygen and should in principle readily substitute into oxygen sites.[77,80] The most encouraging results for nitrogen-doped ZnO layers include (1) the development of growth methods that address the issue of low solubility,[73] (2) the possibility to dope layers uniformly with >10^{19} nitrogen atoms per cm^3,[78] (3) the outdiffusion of hydrogen in layers annealed *ex situ*[70] and (4) the minimization of compensation by the use of NO, N_2O or NO_2 or N_2/O_2 plasmas or more complex nitrogen sources.[81,82] Yet, in most cases, issues of low solubility, low rate of substitution to the oxygen site, compensation by doping-induced defects such as $(N_2)_O$ and N_O-$(N_2)_O$,[83] passivation by hydrogen[68] and poor stability of the *p*-type conductivity due to photoconductivity[84] have lead researchers to question the efficiency of nitrogen doping.

As an alternative to nitrogen, doping with larger-size (measured in terms of ionic radius) group-V elements such as P, As and Sb has been studied.[85-90] Puzzling observations of *p*-type conductivity in ZnO doped with these elements have stimulated theoretical investigations into the electronic structures of the defects induced by P, As or Sb in ZnO.[33,91] In ZnO doped with As or Sb, the most stable acceptor is a complex that forms under oxygen-rich conditions between a group-V antisite and two zinc vacancies.[33] Such energy-lowering interactions increase the solubility of the acceptor and maximize the formation energies of native compensating donors. For ZnO doped with P, calculations show that depending on the dopant source (P_2O_5, P_2O_3 or Zn_3P_2) and growth conditions (O-rich vs. O-poor), the dominant acceptor under oxygen-rich conditions can be the zinc vacancy or the P_{Zn}-$2V_{Zn}$ complex.[91] There is still no compelling evidence for the existence of such complexes in ZnO. However, recent measurements based on the channeling emission techniques by Wahl *et al.* give evidence for As (3+) substitution for Zn (2+) in As-implanted ZnO single crystals.[92]

Furthermore, in pulsed laser deposition, it is the plume composition that determines the film stoichiometry. Whether choosing between P_2O_5 and Zn_3P_2 will influence the growth kinetics or dopant incorporation mechanism remains to be experimentally demonstrated. Finally, it is interesting to note that Zn_3P_2, Zn_3Sb_2 and Zn_3As_2 are *p*-type semiconductors. Whether the existence of such impurity phases in ZnO (less than 1 at. %) can lead to *p*-type conduction is another open question.

While much research has been carried out on *p*-type ZnO, the crystal defects induced by acceptor dopants have not been studied in details. Although reasonable *p*-type conductivity has been reported,[73,78,85,86] there is little understanding of the role of crystal defects on the onset of *p*-type conductivity. The literature also reveals strong temperature dependences of the conductivity type and dopant solubility. Thus, it is crucial to determine the relationships between the processing conditions (dopant source, growth and annealing temperatures) and the structural changes in the epilayers to explain the conductivity type change from *n*- to *p*-type and the optical properties. These will be studied in chapters 4 and 5.

There have been few studies relating the crystal defects to the luminescence and electrical transport properties of acceptor-doped ZnO epilayers. One of the objectives of this thesis is to address this lack by offering more understanding of the relationships between *p*-type doping, defect formation and the optical and electrical signatures of these defects. Therefore, it is of interest to review the effects of defects on the properties of wide band gap semiconductors.

2.3 Relationships between defects and physical properties of wide band gap semiconductors

The epitaxial growth of II-VI and III-V semiconductors on highly-mismatched substrates ($\delta>0.05$) generally proceeds by the coalescence of islands and results in epilayers containing 10^8-10^{12} cm^{-2} threading dislocations and stacking faults depending on the process and substrate treatment employed.[93] The dislocations are often clustered in local regions of the epilayer, leaving large volumes defect-free. Besides the theoretical limitations summarized in section 2.1.2, the main difficulty in achieving *p*-type conductivity in ZnO comes from the effects of crystal defects and their interactions with dopants.

In most semiconductors, dislocations introduce electrostatic and strain fields that scatter carriers and reduce the carrier mobility. In particular, dislocations with an edge component introduce acceptor centers along their lines, which capture free electrons.[94] It is also widely accepted that threading dislocations in GaN-based devices provide charge leakage pathways.[95]

Crystal defects introduce unusual optical transitions, referred to as Y-line transitions. First discovered by Dean in ZnSe,[96] these transitions have been observed in CdTe,[97] ZnTe[98] and GaN[99] samples and have been attributed to bound excitons localized at defects such as stacking faults,[100] screw dislocations,[101] inversion domain boundaries,[102] surface defects,[103] or at point defects gettered by these defects. These strongly localized transitions are assigned by exclusion principles based on careful systematic and comparative photoluminescence spectroscopy studies (see section 3.6.2 for details on how to conduct such studies).

Dislocations cause optical devices to malfunction. The external quantum efficiency of AlGaAs light-emitters drops from 6% to 0.5% when the dislocation density increases from 10^3 to 10^6 cm^2.[104] The dislocations force rapid recombination of electrons with holes, without conversion of their energy into light (non-radiative recombination). The non-radiative nature of dislocations is presumed to arise from their possession of deep electronic states, which trap radiative recombination. The dislocations reduce the minority carrier diffusion length and when the spacing between them is comparable to the exciton diffusion length, the luminescence efficiency decreases.[105] Dislocations also cause degradation during device operation. According to the recombination-enhanced defect reaction model,[106] the energy liberated into the solid upon non-radiative recombination can be utilized to drive diffusion and promote defect reactions. The transport of point defects can drive the motion of dislocations. In arsenide- and phosphide-based devices, it was found that the cause of rapid degradation was the multiplication of dislocations through their climb and glide.[107] Studies have also shown that the degradation mechanism of ZnSe-based devices occurs via propagation of misfit dislocations (the so-called dark line defects) into the active region via climb.[108]

Contrary to ZnSe-, AlGaAs- and AlGaInP-based devices, outstanding internal quantum efficiencies have been measured in GaN devices despite the large dislocation densities. Substantial minority carrier injection and radiative recombination occur without the need for a high degree of perfection in GaN epilayers. Under device operation, the mobility of dislocations in GaN is about 10^{-21}-10^{-27} times lower than in GaAs.[109] The negligible dislocation climb motion in GaN may be one of the reasons for the remarkable longevity of GaN light emitters.

2.4 ZnO epitaxy

2.4.1 Crystal structure of ZnO

Most binary II-VI compound semiconductors crystallize in the cubic zincblende or hexagonal wurtzite structure. ZnO, as the mineral zincite, crystallizes under normal conditions in the wurtzite structure shown in Fig. 2.2. The wurtzite structure (space group $P6_3mc$)[110] can be described by the stacking of close packed double layers of 0001 planes in the 0001 direction. For ideal stacking, the sequence repeats itself as aAbB, where each letter designates a stacking plane, and with the convention that upper- and lower-case letters indicate Zn and O planes respectively. The primitive unit cell contains four ions, two anions and two cations, with the corresponding basis vectors: $(0,0,0)$, $(a/\sqrt{3},0,c/2)$ for the cations, and $(a/\sqrt{3},0,c/8)$, $(0,0,5c/8)$ for the anions. In an ideal hcp lattice, the ratio c/a is equal to $\sqrt{8/3}$. In practice, depending on the position of the interstitial cations occupying the tetrahedral sites, the c/a ratio may deviate from ideality. The deviation from ideality is usually given by the symbol u, which corresponds to the relative displacement between the anion and cation hcp sublattices along the c-axis. Note that there is a relationship between u and the c/a ratio:

$$u = \frac{1}{4} + (\frac{a}{c\sqrt{3}})^2 \quad (2.5)$$

In this thesis, the following lattice parameters are taken as reference for bulk ZnO: u=0.3797, c_{ZnO}=5.2066 Å, a_{ZnO}=3.2498 Å and the Zn-O bond length is 1.94 Å.

Since the wurtzite structure lacks inversion symmetry, the basal plane of ZnO is polarized. The lattice polarity has a crucial effect on the material growth process, properties and impurity incorporation.[111] By convention, ZnO is Zn-polar when the Zn-O bond along the $+c$ direction points from O to Zn. Thus, $000\bar{1}$-ZnO is $-c$ polar and O-terminated while 0001-ZnO is $+c$ polar and Zn-terminated.

2.4.2 Epitaxial growth

The interface formed between a layer and a substrate is either coherent, semi-coherent or incoherent.[112] When the layer matches the substrate perfectly, the interface is coherent; there is continuity of the lattices across the interface. This requires the same atomic configuration and happens with homoepitaxial growth. A semi-coherent interface

is characterized by a network of misfit dislocations which form periodically along the interface to take up the disregistry. These dislocations, usually of the edge-type, accommodate the lattice misfit. Finally, when the lattice mismatch is large (>5%), the interface is incoherent. It is obvious that in order to minimize interfacial strain effects on the layer properties, the interface should be as coherent as possible.

Due to the fact that large area wafers of Al_2O_3 can be fabricated at low cost, the most widely used substrate for ZnO epitaxy is (0001) Al_2O_3. While this substrate has the advantage of being transparent in the visible and chemically robust, it is crystallographically mismatched with ZnO. Indeed, the corundum structure is rhombohedral while the zincite structure is hexagonal. Thus, in addition to the thermal mismatch (~-13%), a large lattice mismatch (~18.4%) exists between (0001) Al_2O_3 and (0001) ZnO.

In order to minimize the interfacial mismatch, a nucleation layer can be used. When the nucleation layer is ZnO, it is normally deposited at low temperature (LT) and under high oxygen pressure. The low growth temperature limits the mobility of surface adatoms resulting in a three-dimensional growth that will ensure uniform coverage of the substrate surface. The high oxygen pressure enhances three-dimensional growth. Note that oxygen-rich conditions are preferred for the growth of insulative ZnO nucleation layers. These will not -if resistive enough- interfere with the electrical measurements of the main layer. Note that some groups have used semi-insulative Li-doped ZnO as nucleation layers, yet the thermal instability of Li is an issue.[78] Nucleation layers may or may not be annealed at high temperature before growth of the main layer depending on whether this step will degrade the surface topology and reduce the number of nucleation sites. Note that for GaN epitaxy, the growth of GaN LT nucleation layers usually follows a step of nitridation of the surface of Al_2O_3. In analogy with GaN epitaxy, the surface of Al_2O_3 can be pre-treated with an oxygen plasma in order to expose a fresh O-monolayer. To summarize, the role of a ZnO nucleation layer is to relieve the interfacial strain, supply nucleation centers and promote lateral two-dimensional growth of the main ZnO layer. As a result, the properties of the main layer are enhanced though, quite obviously, these properties also depend strongly on the stoichiometry, surface morphology and

microstructure of the LT nucleation layer, which themselves mostly depend on the II-VI ratio and substrate temperature.

Nearly lattice-matched materials exist for improved heteroepitaxy of ZnO. For example, InGaN containing 22% indium[113] or $ScAlMgO_4$. $ScAlMgO_4$ is an hexagonal oxide compound that can be viewed as a superlattice formed by alternating stacks along the *c*-direction of (111) $(ScO)_y$ rocksalt layers and (0001) $(Mg,Al)O_x$ wurtzite layers.[114] It has the following lattice parameters: a_{SCAM} =3.246 Å, c_{SCAM} =25.195 Å and a lattice mismatch with ZnO equal to ~0.09% when the growth is hexagon-on-hexagon. $ZnO/ScAlMgO_4$ layers show superior optical[115] and electronic transport[71] properties. Yet, one issue with such substrate is the difficulty to find suppliers. As an alternative, it is worth noting that the lattice mismatch between ZnO and GaN is ~1.8% while that between ZnO and AlN is 4.3%. Thus, ZnO is a suitable substrate for GaN epitaxy, GaN/Al_2O_3 a suitable template for ZnO epitaxy and AlN a suitable nucleation layer for ZnO epitaxy on (111) Si.

Several other materials have been tested as potential substrates for ZnO heteroepitaxy. A first group consists of (111)-oriented cubic substrates such as MgO, Si or YSZ.[116] The issue with (111) MgO is that the surface energy of the (111) surface is the highest among (100), (110) and (111). Thus, the (111) face is extremely difficult to cleave and prepare for epitaxy. As an alternative, (111) MgO templates can be grown on (0001) sapphire substrates by molecular-beam epitaxy.[117] These templates dramatically reduce the mosaicity of the ZnO epilayers and suppress the formation of rotation domains. These domains sometimes appear in ZnO/Al_2O_3 because of the difficulty to obtain an ideal sapphire substrate with well-defined termination. Two types of rotation domains have been observed, namely 21.8° and 30° domains.[118] These can be eliminated by nitridation of the sapphire surface[119] or pre-treatment with Ga.[120] Growth of ZnO on (111) YSZ has been little investigated despite the fact that this substrate offers an atomically smooth surface, which is desirable for multi-layered or MgZnO/ZnO heterostructure growth. Other possible substrates include Al_2O_3 (with the $(1\bar{1}02)$ *r*-, $(10\bar{1}0)$ *m*- or $(11\bar{2}0)$ *a*- surfaces), (0001) SiC,[121] (100) $LiAlO_2$,[122] (0001) $LiNbO_3$,[123]

fused quartz and polycrystalline glass. Table 2.2 provides a non-exhaustive list of possible substrates for ZnO epitaxy.

2.4.3 Crystal defects in wurtzite ZnO

As discussed in section 2.3, ZnO epitaxial films grown on (0001) sapphire substrates contain a high density of threading dislocations. The Burgers vectors of the dislocations in hexagonal close-packed semiconductors can be deduced using an approach similar to the Thompson tetrahedron used in face-centered cubic semiconductors, as shown in Fig. 2.3.[124] When the Burgers vector is not a translation of the lattice, the dislocation is referred to as partial. Assuming the line of the dislocation is parallel to the growth direction (threading dislocation), the examination of the bi-pyramid leads to the following dislocation types in ZnO films grown on sapphire:[125]

-edge dislocations with a Burgers vector equal in magnitude to any edge of the Thompson tetrahedron's basal plane: $\vec{\boldsymbol{b}}_e = 1/3 < 11\bar{2}0 >$ (6 possibilities, e.g. $\overrightarrow{AC}$).

-screw-type dislocations with a Burgers vector equal in magnitude to the *c*-axis: $\vec{\boldsymbol{b}}_s = < 0001 >$ (2 possibilities, e.g. $\overrightarrow{TS}$).

-mixed-type dislocations with a Burgers vector that is a combination of the above two: $\vec{\boldsymbol{b}}_m = \vec{\boldsymbol{b}}_e + \vec{\boldsymbol{b}}_s$ (12 possibilities, e.g. $\overrightarrow{AD}$).

-partial basal dislocations with a Burgers vector $\vec{\boldsymbol{b}}_{sp} = 1/3 < 01\bar{1}0 >$ (6 possibilities, e.g. $\overrightarrow{A\sigma}$). These dislocations are known as Shockley partial dislocations.

-partial dislocations with a Burgers vector equal in magnitude to one-half of the *c*-axis: $\vec{\boldsymbol{b}}_{fp} = 1/2 < 0001 >$ (4 possibilities, e.g. $\overrightarrow{\sigma S}$). These dislocations are known as Frank partial dislocations.

-partial dislocations with a Burgers vector that is a combination of the above two: $\vec{\boldsymbol{b}}_{fsp} = 1/6 < 02\bar{2}3 >$ (24 possibilities, e.g. $\overrightarrow{AS}$).

In addition to dislocations, at least four types of stacking faults have been predicted in wurtzite GaN and ZnO.[126,127] Some faults are formed by the removal of a basal layer followed by slip along $1/3 < 10\bar{1}0 >$, resulting in the aAbB*aAbBcC*bBcCbB sequence. Another type of fault produces a slip of $1/3 < 10\bar{1}0 >$, resulting in the aAbB*aAbBcCaA*cCaA sequence. The third type of faults corresponds to an aA or bB

layer occupying the wrong position and has been proposed by Stampl *et al*.[126] The fourth type of fault proceeds by the insertion of a basal layer, which results in the aAbB*aAbBcC*aAbBaAbB sequence. For details on the atomic arrangements of the faults, the reader is invited to consult Ref. 126. Note that these faults differ by the amount of cubic bonds (*aAbBcC* stacking as in the zincblende structure) they introduce. The first three faults are referred to as intrinsic while the latter type of fault is referred to as extrinsic.

2.5 Summary

In this chapter, theoretical and experimental difficulties in doping ZnO *p*-type have been reviewed. The effects of crystal defects in wide gap semiconductors have been studied and the defects forming in undoped ZnO have been reviewed. The main challenges in the synthesis of *p*-type ZnO are to obtain electronic and optical properties of practical use for device application. While the electronic quality of an epilayer is usually measured by its Hall mobility, free carrier concentration and resistivity, the optical quality is measured by its photoluminescence output and absorption. These quantities are defined in chapter 3. Crystal defects in acceptor-doped ZnO are however often overlooked even though they can be detrimental to these properties. In chapters 4 and 5, *p*-type ZnO epilayers are fabricated and the relationships between processing, structural defects and optoelectronic properties are studied.

Table 2.1 Ionic radii and size mismatches ($\varsigma = r_{dopant} / r_{host} - 1$) with host atoms of potential acceptor dopants in ZnO.[34] The ionic radii correspond to a coordination number of 4. The elements in italic introduce acceptors upon substitution of the host element in bold.

Element	*Ionic Radius (Å)*	*ς (%)*
Zn (+2)	0.60	
Li (+1)	0.59	-2
Na (+1)	0.98	63
P (+3)	0.58	-3
As (+3)	0.60	~0
Sb (+3)	0.76	27
O (-2)	1.38	
N (-3)	1.71	24
P (-3)	2.12	54
As (-3)	2.22	61
Sb (-3)	2.45	78

Table 2.2 Possible substrates/templates for ZnO epitaxy and their in-plane lattice mismatches with ZnO.

Substrate material	*Surface orientation*	*Lattice mismatch (%)*
InGaN (22% In)	(0001)	~0
$ScAlMgO_4$	(0001)	0.09
GaN	(0001)	1.8
AlN	(0001)	4.3
SiC	(0001)	5
$LiNbO_3$	(0001)	8.5
Al_2O_3	(0001)	18.4
Sc_2O_3	(111)	6.6
MgO	(111)	9
YSZ	(111)	10.6
Lu_2O_3	(111)	11.4
Gd_2O_3	(111)	15
Si	(111)	15.4
CaF_2	(111)	15.8
$LiAlO_2$	(100)	3
Al_2O_3	*r*-plane	1.7
Al_2O_3	*m*-plane	0.08

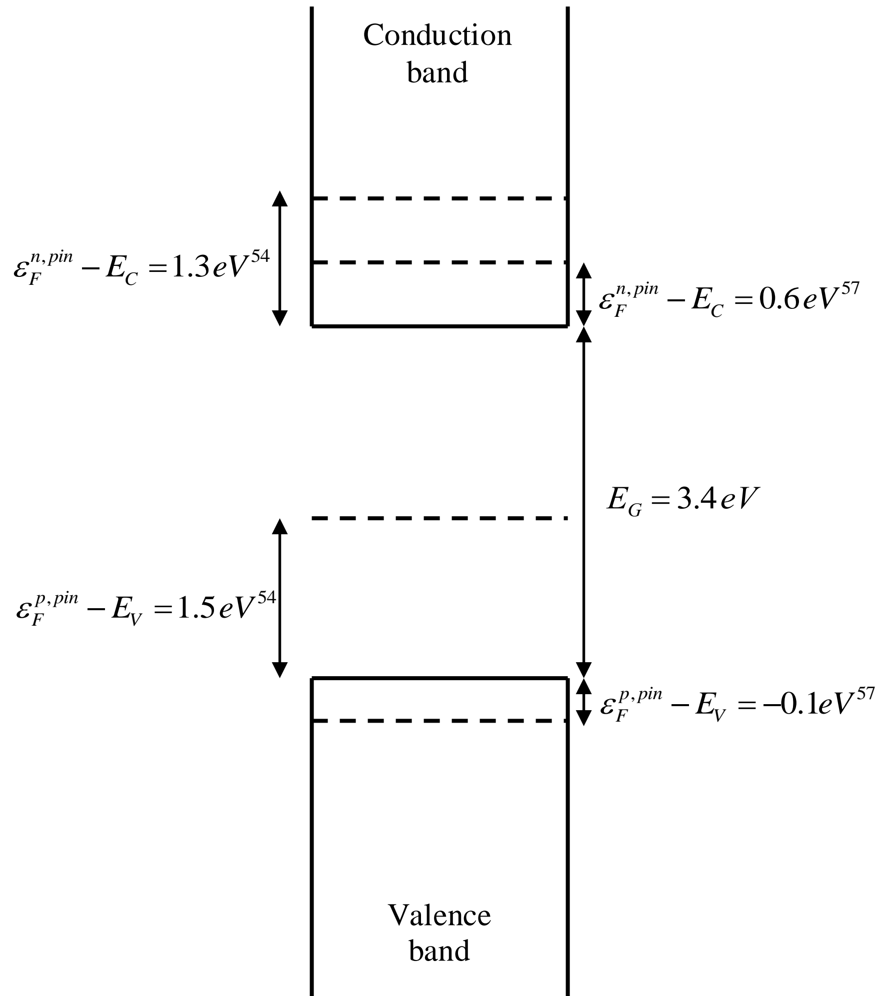

Figure 2.1 Illustration of the doping asymmetry in ZnO, according to Ref. 54 and 57.

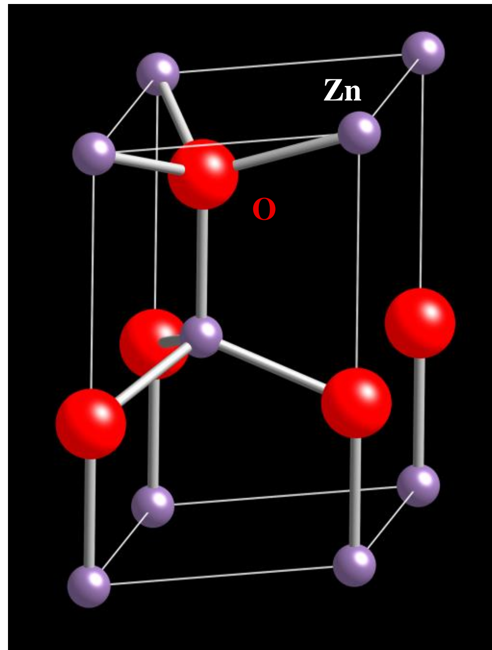

Figure 2.2 Ball and stick model of the wurtzite structure.

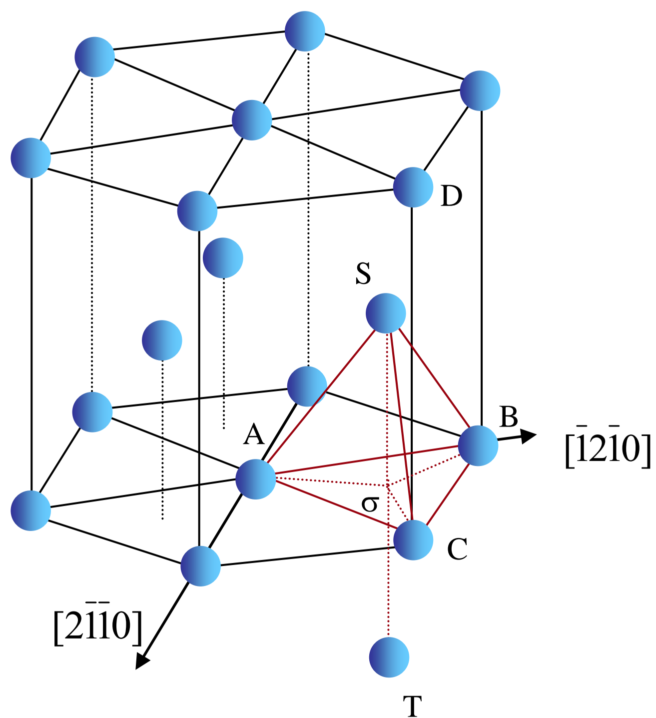

Figure 2.3 Wurtzite structure and application of the Thompson tetrahedron to the hexagonal close-packed lattice of ZnO. Only the Zn layers are represented.

Chapter 3

Experimental Techniques

3.1 Epitaxial growth

Epitaxy can be defined as oriented overgrowth, *i.e.* crystal growth on another crystal with single, well defined, related orientation relationships. The epilayers studied in this work were fabricated by pulsed laser deposition (PLD).

3.1.1 Principles of thin film growth by PLD

Pulsed laser deposition is a thin film growth method that consists of three steps:[128] (1) the interaction of the pulsed laser beam with a ceramic target usually in the form of a sintered pellet (ablation); (2) the formation and expansion of the laser-induced plasma and (3) the deposition of the film on a substrate maintained at a certain temperature (growth temperature).

The success of superconducting thin film growth by PLD in 1987 led to the development of this technique[129] and to its wide use in research laboratories. The most obvious advantage of PLD over molecular beam epitaxy or organo-metallic vapor phase epitaxy is that it allows a direct transfer of stoichiometry from the target to the film. Thus, multicomponent films can be conveniently grown by congruent vaporization of a single ceramic pellet, which only requirement should be to have the desired stoichiometric proportions. In addition, PLD is a versatile epitaxial route that allows the rapid growth of almost any kind of material over a wide range of gas ambients, pressures, substrate temperatures, laser power densities (fluences) and repetition rates.

For a ZnO target irradiated with a laser pulse having a t_p =22 ns temporal width, the heat diffusion length L in the target is:[130]

$$L = \sqrt{\frac{\kappa t_p}{C}} \qquad (3.1)$$

where κ and C are the thermal conductivity and volume heat capacity in ZnO respectively. Taking κ=1.3 W/cm·K[131] and $C=1.7\times10^{-3}$ J/cm^3·K,[132] we find L~40 µm. The absorption length δ in ZnO for a 248 nm pulse (KrF excimer laser) is 40 nm,[132] corresponding to $L/\delta \sim 10^3$ and showing that heat diffusion with PLD in the nanosecond regime is not negligible. This issue, though it can have important consequences on the composition of the target, will be ignored in this thesis.

In addition, there are at least two intrinsic issues with PLD: first, the low purity of the ceramic target, which usually needs to be prepared by mixing powders, followed by uniaxial or isostatic pressing and sintering. Such process introduces impurities which may have undesired effects in the film such as unintentional conduction and excitonic broadening. The second issue is the formation of micron-scale particles at the film surface (droplets). These droplets are induced by the ejection of molten liquid from the ablation front (splashing).[129] Though ZnO sublimes at its melting point (2248 K), it has been shown that the existence -for a very brief time- of a molten state accounts for the ejection of liquid droplets.[133] Note that it can be difficult to scale up PLD to large-size wafers (2" and above) while maintaining uniform substrate coverage, layer composition and thickness. For that reason, sputtering (radio-frequency or direct-current depending on the target conductivity) is a good alternative to PLD.

The growth rate in PLD can be controlled by optimizing process parameters such as the target-substrate distance, the laser fluence, repetition rate, and the oxygen backfill pressure. The latter controls the mean-free path of species composing the plume, their kinetic energies and the plume angular distribution.

Ultrafast PLD, which employs low-energy laser pulses in the picosecond or femtosecond regimes, has been suggested as a method to overcome the problem of droplet formation. This happens because the pulse width is shorter than the electron-phonon timescale in solids (typically on the order of a few ps). In other words, thermal effects in the target can be neglected. Yet, the high pulse power density (~10^{15} W/cm^2)

caused by the brevity of the pulse (~100 fs) induces high kinetic energy (~1 keV) species in the plume,[134] which can sputter the film surface and increase its roughness.

3.1.2 PLD systems

Two PLD systems are used in this study. A description of the first PLD system can be found in Ref. 135. The second PLD system is an ultra-high vacuum system manufactured by Thermionics Northwest, Inc. The main chamber is a stainless steel 22" diameter cylindrical chamber evacuated by a Varian V-551 turbopump backed with a Varian Triscroll dry-pump. The chamber base pressure is less than 5×10^{-9} mbar. A load-lock chamber (LLC) is used to transfer substrates and targets in and out. The LLC is evacuated by a Pfeiffer TMU-071P air-cooled turbomolecular pump backed with a Pfeiffer MVP 035-2 diaphragm pump. The substrate manipulator is equipped with an XYZ stage. The XY micrometers allow a ± 0.5" travel and the Acme drive allows a Z travel of 4". In addition, 360° of continuous polar motion are provided by a two-stage differentially pumped rotary seal (RNN). This allows fine positioning of the substrates in the vacuum chamber. Substrates are radiatively heated at temperatures up to 1100 ºC by a $Pt_{0.8}/Rh_{0.2}$ filament. A type-K thermocouple is placed beneath the filament to monitor the heater temperature. The substrate assembly is also equipped with a motorized magnetic feedthrough for azimuthal rotation of the substrate during growth. The target gearbox is operated on a dual-axis rotary feedthrough. One axis is used for vertical clocking of the targets and the other axis is used for spinning. The substrate-target distance is adjustable between 1.5" and 2.5". The vacuum level is monitored in each chamber by a Pfeiffer compact full range gauge consisting of Pirani and cold cathode systems able to measure from 10^3 mbar to 3×10^{-9} mbar.

The chamber is equipped with a radio-frequency (RF) plasma source (HD-25, Oxford Applied Research, Inc.) for plasma-assisted growth. The atomic source consists of an alumina discharge zone subject to an inductively-coupled RF excitation of up to 600 W. Nitrogen or oxygen gases are introduced into the discharge zone and ionized. Neutral atoms exit from the cavity through a series of aperture holes whereas ions remain confined in the plasma. The distance between the focal point of the substrate plane and the atomic source is 150 mm. For O_2 plasma-assisted growth, the O_2 pressure in the

cavity was set to 6.6×10^{-5} mbar and the plasma power was set to 275 W. The chamber was then backfilled with 8×10^{-5} mbar O_2.

The laser is an excimer KrF gas laser (Compex 205, Lambda-Physik, λ=248 nm) that consists of a laser tube filled with a Krypton-Helium-Fluorine-Neon premix (3.82 % - 1.68 % - 0.09 % - 94.41 %). The nominal pulse width is 22 ns. The output beam has a 22×8 mm^2 rectangular profile, is steered using mirrors made of fused silica coated with MgF_2 and focused onto the target by a bi-convex spherical lens (f=18") at a fluence of ~1.7 J/cm^2.

3.1.3 Target and substrate preparation

Commercial targets of desired stoichiometric proportions are purchased from Praxair, Inc. and SCI, Inc. A smooth surface and a high density are the desirable features of a target in order to minimize splashing.[129] Prior to growth, the targets were polished with SiC grit paper in order to expose a smooth surface and pre-ablated in order to remove contaminants.

All substrates used in this study are both side epi-ready. (0001)-oriented Al_2O_3 (sapphire) substrates were purchased from Crystec Kristalltechnologie GmbH. (0001)-oriented ZnO substrates were purchased from Crystec Kristalltechnologie GmbH, Cermet, Inc. and MTI, Inc. Before being loaded in the PLD chamber, the substrates were ultrasonically cleaned in acetone and methanol (two sequences), rinsed with de-ionized water and blown dry with N_2 gas. Prior to growth, the substrates were baked in vacuum at 800 ºC for twenty minutes.

All films were deposited with the laser repetition rate set to 5 Hz and the fluence set to 1.7 J/cm^2. The growth rate was 1 Å/s at 600 ºC.

3.2 Structure and microstructure characterization

3.2.1 X-ray diffraction

All ZnO layers were studied by a combination of X-ray diffraction (XRD) techniques. The measurements were conducted using two diffractometers: a triple axis BEDE-D1 diffractometer having a monochromatic Cu-Kα (λ=1.5405Å) radiation source

operated at 40 kV and 40 mA, and a Rigaku-Rotaflex rotating anode four-circle diffractometer with the same radiation source operated at 40 kV and 100 mA.

The structural quality of the ZnO epilayers was quantified by the full-width at half-maximum (FWHM) values of the rocking curves around the 0002 and $10\bar{1}2$ surface normals. A rocking curve (or ω-scan) plots the diffracted X-ray intensity as a function of ω and is measured by rocking the sample over a small angular range while fixing the open detector to the 2θ Bragg angle of the reflection. Only the orientation of the diffraction vector is varied. The scan speed and step size were chosen according to the sharpness of the rocking curve. The BEDE diffractometer was used for rocking curve measurements with the first (022) Si channel cut collimator (CCC) crystal in the path of the X-ray beam for improved resolution. A horizontal circular slit (5 mm in radius) and a vertical divergence slit (500 μm in width) were inserted in the X-ray beam path, resulting in a spot size on the order of 4 mm^2.[136] Double-sided tape was used to mount the sample on the sample holder. The open beam X-ray intensity was 1.7×10^5 counts per second (cps) at 30 kV and 20 mA. The sample was positioned in the X-ray beam path by adjusting the X and Y axes of the sample holder and measuring ω-scans at ϕ=0° and ϕ=180°. A tilt optimization (χ-scan) was performed prior to measuring the rocking curve. This step is especially critical when the rocking curve is sharp.

More detailed characterization was performed by studying the mosaic structure formed by ZnO films heteroepitaxially grown on (0001) sapphire substrates. This structure is schematized in Fig. 3.1. The epilayer mosaicity is characterized by four parameters, the tilt angle (angular rotation perpendicular to the growth plane), the twist angle (angular rotation within the growth plane), the lateral coherent length and the vertical coherent length. The four parameters are taken as a measure of the epilayer crystallinity.

Figure 3.2 illustrates the various XRD geometries used to evaluate these parameters. The asymmetric geometry is used to measure planes that are not parallel to the sample surface.

The epilayer tilt is determined by a Hall-Williamson analysis,[137] which is a plot of the FWHM values of the rocking curves of symmetric reflections as a function of the reflection order. The tilt angle is equal to the slope of:

$$FWHM \times \frac{\sin(\theta)}{\lambda} = f(\frac{\sin(\theta)}{\lambda}) \quad (3.2)$$

while the lateral coherent length can be obtained by extrapolating the curve to θ=0°. For ZnO grown on (0001) sapphire, a Hall-Williamson analysis consists of three rocking curve measurements, around the 0002, 0004 and 0006 reflections. The epilayer twist is determined by plotting the FWHMs of the rocking curves measured in skew symmetric geometry as a function of the lattice plane inclination angle ψ (skew plot). The angle χ formed between any two $hk\overline{h+k}l$ and $de\overline{d+e}g$ planes in the hexagonal close-packed lattice is given by:

$$\cos(\chi) = \frac{hd + ke + \frac{1}{2}(he + kd) + \frac{3}{4}gl(\frac{a_{ZnO}}{c_{ZnO}})^2}{\sqrt{(h^2 + k^2 + hk + \frac{3}{4}l^2(\frac{a_{ZnO}}{c_{ZnO}})^2)} \cdot \sqrt{(d^2 + e^2 + de + \frac{3}{4}g^2(\frac{a_{ZnO}}{c_{ZnO}})^2)}} \quad (3.3a)$$

To determine the angle ψ between a $hk\overline{h+k}l$ lattice plane and the 0002 basal plane, a more simple equation can be used:

$$\tan(\psi) = \sqrt{\frac{4}{3}} \frac{\sqrt{h^2 + k^2 + hk}}{l} \frac{c_{ZnO}}{a_{ZnO}} \quad (3.3b)$$

The twist angle is determined by an extrapolation of the skew plot to ψ=90° as the BEDE diffractometer can only incline samples up to 43°.[138] The vertical coherent length is approximately the layer thickness.

θ-2θ scans of heteroepitaxial ZnO epilayers were measured using the Rigaku diffractometer. In a θ-2θ scan, both the sample and detector are rotated with respect to the X-ray beam. Only the diffraction vector magnitude is varied. The scan speed was set to 5 deg/min and the increment was set to 0.01 deg. The alignment was verified by the intensity of the 0006 reflection of Al_2O_3, which diffracts ~3×10^4 cps at 40 kV and 100 mA. θ-2θ scans of homoepitaxial ZnO layers were measured using the BEDE diffractometer set in high-intensity mode (first CCC crystal out of the beam path). A 200 µm slit was used to align the detector to the 2θ Bragg angle of the reflection studied.

Asymmetric ϕ-scans and reciprocal space maps (RSMs) were measured in the glancing incidence geometry using the BEDE diffractometer set in high-intensity mode. It is useful to note that in ZnO, the normal to the $(11\bar{2}4)$ plane is the $[11\bar{2}0] = [110]$

direction and that this direction forms a 30° angle with the $[10\bar{1}0]=[210]$ direction. More details on these methods are available in appendix A.

3.2.2 Atomic force microscopy

The film surface was studied by atomic force microscopy using a Nanoscope III (Digital Instruments, Inc.). The cantilevers (µmasch, NSC15/AlBS) are made of Si_3N_4 and have their backside coated with Al. The microscope was operated in tapping mode to avoid damage and scraping of the film surface. The vertical offsets induced by artifacts such as sample tilt, scanner drifting or image bow were removed by a third-order flattening performed using the control software. This was done prior to conducting section and roughness analyses using the control software.

3.2.3 Transmission electron microscopy

Cross-sectional transmission electron microscopy (TEM) specimens were prepared by a standard procedure that includes mechanical grinding, polishing, precision dimpling and ion milling. Typically, the TEM specimen is ~100 µm-thick before dimpling. After dimpling, the thinnest area is ~30 µm-thick. Finally, ion milling using two argon guns set at ~4 kV is used to make the specimen electron transparent. The beam energy is progressively lowered as the specimen becomes more transparent in order to prevent damage. An optical microscope can be used to monitor the interface formed between the Si sacrificial layer and the ZnO surface. Ideally, the hole formed in the sacrificial layer should lightly impinge on the ZnO surface, however this usually depends on the amount of glue at the interface. More details on the sample preparation procedure can be found in Ref. 139.

To determine the cutting direction in ZnO layers grown on *c*-plane Al_2O_3, pole figures of an asymmetric reflection of ZnO and Al_2O_3 had to be measured. A $10\bar{1}4$ pole figure of Al_2O_3 features 3 poles at an inclination angle χ~38°. A $10\bar{1}1$ pole figure of ZnO features 6 poles at χ~62°, which altogether form an hexagon. The ZnO samples were thus cut along the edge of the hexagon in order to be imaged along the $[10\bar{1}0]$

direction. The samples cut along the $[1\bar{1}00]$ direction were imaged using the $[11\bar{2}0]$ zone axis.

A JEOL 3011 microscope was used to image the samples. The electron beam was set along the $[10\bar{1}0]$ and $[11\bar{2}0]$ zone axes of ZnO, the latter offering better atomic resolution of the ZnO lattice. Schematic atomic arrangements of the ZnO hexagonal wurtzite structure viewed along these two directions are shown in Fig. 3.3.

3.3 Nuclear reaction analysis

In backscattering spectrometry, the energy and number of elastically backscattered ions are measured to determine the sample stoichiometry and depth-profile elements of interest.[140] To determine the elemental concentration of nitrogen (Z=7) in nitrogen-doped ZnO films, nuclear reaction analysis (NRA) was used. An NRA spectrum plots the total counts of incident $^2H_1$ ions scattered by the sample surface as a function of energy. NRA has a spatial resolution on the order of the nanometer[140] and has been widely used to depth-profile hydrogen in semiconductors or establish absolute nitrogen concentration in steels.[141]

Measurements were performed at the Michigan Ion Beam Laboratory by Dr. Victor Rotberg using a 1.7MV Tandetron Accelerator. The sample surface was cleaned with acetone and methanol. The samples were then mounted with their surface normal parallel to the incident beam and were irradiated with a 1.4 MeV $^2H_1$ ion beam. The nuclear reaction was $^{14}N(d,\alpha)\ ^{12}C$. Charged α particles were detected by a semiconductor detector set at θ=150° and subtending a solid angle of Ω=5 msr. The concentration of nitrogen atoms per unit volume N was calculated using:[140]

$$N = Y / [t \cdot \sigma(\theta) \cdot \Omega \cdot N_{inc}] \qquad (3.4)$$

where Y represents the total counts of the detected ions (or yield), t is the sample thickness, $\sigma(\theta)$ is the scattering cross-section at the angle θ and N_{inc} is the total number of incident ions. The yield Y was calculated from the area under the peak produced by α particles, which usually appears on the high-energy side of the NRA spectrum.

3.4 Secondary-ion mass spectroscopy

The dopant depth-profiles were measured by secondary-ion mass spectroscopy at Evans Analytical Group, Inc. (EAG) by Dr. Steve Novak. The conversion factor used to convert the signal intensity to the dopant (nitrogen or phosphorus) concentration was derived from the concurrent analysis of a reference sample (nitrogen- or phosphorus-implanted ZnO). The reference sample is an ion-implanted sample fabricated at EAG. The depth scale was calibrated by using the known depth of the peak in the implanted reference sample to calculate the sputtering rate. The experimental error is about 10-15%. The measurement is done by raster scanning the beam over a $300 \times 300\ \mu m^2$ area and accepting ions from the central $105 \times 105\ \mu m^2$ area. The measurement is destructive and leaves a crater in the film. The detection limits of nitrogen and phosphorus in ZnO are 10^{17} at/cm^3 and 10^{18} at/cm^3 respectively.

3.5 Thermal gravimetric analysis

Thermal gravimetric analysis was performed on a SDT 2960 instrument (TA Instruments, Inc., New Castle, DE). The sample was prepared by uniaxially pressing ~40 mg of Zn_3N_2 powder into a 3 mm diameter pellet. The pellet was loaded in a platinum pan. The data was collected upon heating the pellet between room temperature and 1200 °C at 10 °C/min under a continuous flow of 60 ml/min of synthetic air or nitrogen. The instrument was allowed to air cool back to room temperature under constant air flow. The measurement was used to study the weight loss of the Zn_3N_2 powder as a function of temperature.

3.6 Optoelectronic properties

3.6.1 Spectrophotometry

Transmittance spectra were acquired over a 300-1000 nm range using a Varian Cary 50 UV-Vis spectrophotometer. The substrate backside was first cleaned with acetone and methanol. The sample surface was illuminated at normal incidence. A background correction was performed prior to recording the spectra. The film thickness t can be estimated by a count of the interference fringes. The following formula is used:[142]

$$t = \frac{m}{2\left|\frac{n_{ZnO}(\lambda_1)}{\lambda_1} - \frac{n_{ZnO}(\lambda_2)}{\lambda_2}\right|} \quad (3.5)$$

where m in the number of fringes in the $[\lambda_1, \lambda_2]$ wavelength range and $n_{ZnO}(\lambda)$ is the refractive index of ZnO at λ. For an incident electromagnetic wave parallel to the epilayer c-axis ($E // c$), a first-order Sellmeier equation was used as the dispersion equation of the refractive index: [143]

$$n_{ZnO}(\lambda) = \sqrt{2.85 + \frac{0.87\lambda^2}{\lambda^2 - 0.319^2}} \quad (3.6)$$

with λ in µm.

3.6.2 Photoluminescence

Photoluminescence (PL) is the emission of an optical radiation by a solid following photonic excitation.[144] Photoluminescence is a three-step process including the photo-generation of electron-hole pairs by absorption of the incident radiation in the near-surface region, the radiative recombination of electron-hole pairs, and the escape of the resulting photon. In direct band gap semiconductors, above band gap excitation has a penetration depth on the order of 1 µm. Figure 3.4 illustrates the various recombination processes in semiconductors, as described in the book by Landsberg.[145] In this section, the concepts of free and bound excitons are explained and the radiative transitions illustrated in Fig. 3.4 are described. The PL analysis techniques used throughout this study are then presented.

3.6.2.1 Excitons and the near-band-edge region of the PL spectrum

The concept of exciton in covalent solids was developed by Wannier in 1937.[146] An exciton is a particle that consists of an electron and a hole, both moving in extended orbits with a correlated motion, hence the concept of electron-hole pair. Put simply, an exciton is a bound state of an electron-hole pair. An exciton falls into two categories: the free exciton, existing as a hydrogenically bound electron-hole pair, and the bound exciton, composed of a free exciton molecularly bound to a defect.

In the hydrogenoid approach, free excitons are created in optical absorption transitions occurring at discrete energy levels E_n below the band gap.

$$E_n = E_G - \frac{m^* e^4}{2\hbar^2 \varepsilon_s^2 \varepsilon_o^2 n^2} + \frac{\hbar^2 \vec{K} \cdot \vec{K}}{2(m_e^* + m_h^*)} \quad (3.7)$$

where E_G is the band gap energy and m^* is the reduced mass of the exciton defined as:

$$\frac{1}{m^*} = \frac{1}{m_e^*} + \frac{1}{m_h^*} \quad (3.8)$$

The third right-hand side term in Eq. (3.7) is the exciton kinetic energy and involves the wave vector $\vec{K}$ of the quasi-particle in translation. The ground state of the free exciton corresponds to n=1. The ground state energy of the free exciton is thus smaller than the band gap energy by the free exciton binding energy, which has been experimentally determined to be 59 meV in ZnO. The spectrum of the bound states is illustrated in Fig. 3.4. Note that 59 meV translates into a ratio $m^*/m_o \approx 0.33$ and an excitonic Bohr radius a_B^{ZnO} equal to:

$$a_B^{ZnO} = \frac{\varepsilon_s}{m^*/m_o} a_B \approx 1.4\ nm \quad (3.9)$$

The Bohr radius of such free exciton, also termed Wannier exciton, is larger than the lattice constants of ZnO, hence the validity of the effective mass approach. Yet, it is relatively small, hence the difficulty to achieve confinement in modulated structures.

In this work, we use for the electron effective mass $m_e^* = 0.24 \times m_o$ and for the hole effective mass $m_h^* = 0.59 \times m_o$ (though for the latter, reports of $m_h^* = 0.78 \times m_o$ exist)[147].

The valence band in wurtzite ZnO is split into three subbands by the combined effects of spin-orbit interaction and of the crystal field. The three upper valence bands result in three intrinsic excitonic states (within ~45 meV)[70] commonly denoted A, B and C excitons and labeled as X_A, X_B and X_C respectively. The standard method to determine their energy is reflectance spectroscopy. Note that the energy positions of free excitons vary substantially depending on the epilayer strain.

Excitons can bind to neutral or ionized point defects and form bound exciton complexes. There exist several types of bound excitons, as illustrated in Fig. 3.5. For example, an exciton bound to a neutral donor (D^0X) consists of a donor ion, two electrons

and a hole.[148] Ionized acceptors are unlikely to bind excitons since a neutral acceptor and a free electron are energetically more favorable.[149] The binding energy of the bound exciton (localization energy) is equal to:

$$E_{loc} = E_{FX} - E_{BX} \tag{3.10}$$

where E_{FX} and E_{BX} are the free exciton and bound exciton energies in the ground state respectively. For that reason, bound exciton lines fall generally on the low-energy side of free excitons. The localization energy E_{loc} can be measured directly from the PL spectrum or derived by temperature-dependent measurements.

According to a rule established by Haynes for excitons in silicon,[150] the energy required to free an exciton from a defect is a linear function of the energy required to free a carrier bound to the same defect:

$$E_{loc} = a + bE_i \tag{3.11}$$

where E_i is the energy needed to ionize the defect. Depending on the compound semiconductor, several proportionality constants have been derived for excitons bound to donors and acceptors. Meyer *et al.* obtained a=-3.8 meV and b=0.365 for neutral donors in ZnO[70] while Gutowski *et al.* obtained a=-0.021 meV and b=0.244.[151] For acceptors, a=0 meV and b~0.1.[149]

Experimentally, the near-band-edge PL spectrum of undoped ZnO crystals features several sharp and structured transitions, labeled I_0 to I_{11}, within a 3 nm-wide wavelength region. These are due to the recombination of excitons bound to ionized and neutral defects. Much research has focused on the identification of the donors and acceptors associated with these transitions.[70] Recent findings show that I_0, I_1 and I_2 are ionized donor states associated with I_{6a}, I_8 and I_9 respectively, increasing to seven out of twelve the number of unambiguously identified excitons in ZnO.

Finally, a general rule of thumb is that the localization energy of acceptors in ZnO can lie anywhere between 16 and 30 meV. In fact, in the case of nitrogen-induced acceptors, some groups have reported E_A=160-260 meV based on the observation of donor-acceptor (DA) luminescence,[152-155] in good agreement with Haynes rule and localization energies of about 16-26 meV.

3.6.2.2 Satellite transitions

A two-electron transition is a replica of a donor bound exciton that occurs at a lower energy. An electron orbiting around the nucleus of a donor may jump from the 1*s* ground state (n=1) to an excited energy state (n>1) 2*s*, 2*p* etc. In the hydrogenoid approach, the newly formed exciton recombines at an energy E_n given by:

$$E_n = E_{DX} - E_D(1 - \frac{1}{n^2}) \tag{3.12}$$

The same concept holds for acceptor bound excitons, which can produce two-hole transitions;[156] these transitions are rarely observed in ZnO.

3.6.2.3 Electron-phonon coupling

Every optical transition involves the creation of one or more phonons. For an optical transition accompanied with phonon creation, the photon energy $h\upsilon_{m,n}$ is given by:

$$h\upsilon_{m,n} = E_{ZPL} - mE_{LO} - nE_{TO} \tag{3.13}$$

where E_{ZPL} is the transition energy of the zero-phonon line (ZPL), m is the number of created longitudinal optical (LO) phonons, E_{LO} is the energy of the LO phonon, n is the number of created transverse optical (TO) phonons and E_{TO} is the energy of the TO phonon. In ZnO, the coupling to TO-phonons is generally so weak that TO-phonon replicas do not appear in the PL spectrum. LO-phonons in ZnO have a frequency of 591 cm^{-1}, corresponding to a 71.5 meV energy.

The strength of the coupling is measured by the Huang-Rhys factor S,[157] which corresponds to the mean number of phonons. S is determined by a Poisson distribution:

$$I_n = I_0 \frac{S^n}{n!} \tag{3.14}$$

where I_n is the intensity of the n-th phonon sideband and I_{ZPL} is the ZPL intensity. Depending on the electron-phonon coupling strength, the ZPL may or may not be visible, as evidenced by Fig 3.5, which shows various Poisson distributions for several values of the Huang-Rhys factor. An obvious example is the green luminescence in ZnO, commonly assigned to copper, and characterized by a zero-phonon line, which may or may not appear depending on the sample.[143]

In the Fröhlich coupling model, the Huang-Rhys factor S and the Bohr radius a_B of the electron or hole bound to the defect are related:[158]

$$S = \frac{2^{1/2} e^2}{\pi^{1/2} a_B \hbar\omega}\left[\frac{1}{4\pi\varepsilon_\infty} - \frac{1}{4\pi\varepsilon_s}\right] \tag{3.15}$$

3.6.2.4 Donor-acceptor and free-to-bound transitions

A DA pair is a polycentric complex that involves an electron bound to a donor and a hole bound to an acceptor such that their wavefunctions overlap. The recombination energy of a DAP E_{DAP} is given by:[159]

$$E_{DAP}(r) = E_G - (E_D - \frac{e^2}{4\pi\varepsilon_s\varepsilon_o r}) - E_A \tag{3.16}$$

where E_G is the band gap energy, r is the pair separation and the third term on the right-hand side is the Coulomb energy of the ionized defects after recombination. Donors and acceptors are localized at lattice sites, thus r can only assume discrete values. The DA pair appears as a set of discrete lines corresponding to the allowed values of r. An estimation of the pair separation is given by:

$$r^3 \sim (\frac{3}{4\pi N}) \tag{3.17}$$

where N is the concentration of ionized donors or acceptors depending on their ratio and is proportional to $[N]$ via the ionization ratio.

N is difficult to measure by steady-state PL spectroscopy but can be determined by time-resolved PL. A crude approximation is to set $r \rightarrow \infty$ and graphically determine the corresponding transition energy $E_{DAP}(\infty)$. Using Eq. (3.16), E_A can be calculated.

A more accurate approach to determine E_A is to conduct temperature-dependent measurements. As the measurement temperature increases, the donor ionizes its electrons into the conduction band. The transition of a free electron from the conduction band to a neutral acceptor level A^0 is referred as (e,A^0) transition and its energy is given by:

$$E_{(e,A^0)} = E_G - E_A + \frac{kT}{2} \tag{3.18}$$

where E_A is the acceptor ionization energy and T is the temperature of the free electron in the conduction band. These transitions are dominant at intermediate temperatures or at

room temperature depending on E_A. There exists a temperature at which Eq. (3.16) and Eq. (3.18) can be combined and E_A determined.

3.6.2.5 Temperature dependence of PL transitions

The temperature dependence of the band gap energy can be fitted by several equations. The semi-empirical Varshni equation gives:[160]

$$E_G(T) = E_G(0) - \alpha \frac{T^2}{T+\beta} \tag{3.19}$$

where $E_G(0)$, α and β are fitting parameters. Modified versions of this equation exist:[161]

$$E_G(T) = E_G(0) - \alpha \frac{T^4}{(T+\beta)^3} \tag{3.20}$$

The main limitation of the Varshni equation is that it does not provide a good fit to the experimental data when the measurement temperature range is much less than the Debye temperature (taken as 837 K in this work).[162] The following equation has been proposed by Manoogian and Wooley:[162]

$$E_G(T) = E_G(0) + \lambda T^s + \mu\theta(\coth(\frac{\theta}{2T}) - 1) \tag{3.21}$$

where θ is related to the Debye temperature and s, λ and μ are fitting parameters.

In this work, the experimental data was well fitted by Eq. (3.19).

The temperature dependence of the integrated intensity of a bound exciton BX can usually be fitted to:

$$\frac{I_{BX}}{I_o} = \frac{1}{1 + \sum_i^N C_i \exp(-\frac{E_i}{kT})} \tag{3.22}$$

where N is the number of Arrhenius steps in the quenching process, E_i and C_i are fitting parameters. In most cases, N =1 or N =2. When N =2, the activation energy E_1 driving quenching at low temperature represents the exciton binding energy while the activation energy E_2 driving quenching at high temperature corresponds to the defect ionization energy. Usually, $C_1 << C_2$.

3.6.2.6 Excitation intensity dependence of PL transitions

The lifetime and concentration of defects in ZnO are finite therefore it is possible to saturate defect-related luminescence when using high excitation intensities.

The luminescence intensity I of a near-band-edge PL transition is proportional to F^{β}, where F is the laser excitation intensity and β is a dimensionless exponent. For bound excitons, $1<\beta<2$, while for DA or free-to-bound transitions, $\beta<1$.[163]

A characteristic of DA transitions is to blueshift under increasing excitation intensity. Indeed, the number of occupied donor and acceptor centers increases; their average distance necessarily decreases, which shifts the band peak energy toward the blue because of the Coulomb energy term.[149]

Note that power-dependent PL can be used to determine the acceptor concentration in n-type ZnO, as shown by Reshchikov *et al*.[164]

3.6.2.7 Apparatus

The ZnO samples were loaded in a closed-cycle He cryostat (ARS, Displex, CS-202) operated between 10 and 300 K. Conductive copper tape was used to mount the samples onto the holder. The angle between the sample surface normal and the laser beam was ~20 deg. The cryostat was first evacuated to a pressure of 10^{-5} mbar by a Pfeiffer TSH-071E turbopumping station. The compressor was turned on after 15 min. The luminescence was excited by a He-Cd laser (Kimmon, IK3501R-G, λ=325 nm, 100 mW), focused onto the entrance slit of a 1 m monochromator (HORIBA Jobin-Yvon, 1000M) and detected by a photomultiplier tube (Hamamatsu, R928) operating in photon counting mode.

The photoluminescence was measured between 350 and 700 nm using a 0.1 nm increment and a 1 second acquisition time. The sizes of the monochromator and PMT slits were adjusted between 50 and 400 μm in order to prevent PMT saturation (occurring at 2×10^{6} cps). The near-band-edge emission of the epilayers, which contains useful information on bound exciton complexes, is measured between 350 and 400 nm. In that range, the quantum efficiency of the photomultiplier tube (PMT) is almost constant (25 %), thus the relative intensities of the PL transitions can be directly compared. Note that between 400 and 700 nm, the quantum efficiency of the PMT drops from 25 % to 8 %.

Thus, care must be taken upon interpreting spectral features in the high wavelength region or comparing their intensities with those of transitions in the near-band-edge region.

A laser line filter with a 1.2 nm bandwidth was used to filter wavelengths around the 325 nm radiation of the He-Cd laser. A long wave pass edge filter was placed in front of the entrance slit of the monochromator. Its transmission was above 95 % between 330 and 430 nm but dropped to 40 % at 450 nm. Again, care must be taken upon comparing intensities of low- and high-energy transitions. This filter was also found to introduce interference fringes between 450 and 700 nm. These fringes contained no information on the sample measured and were strictly related to the set-up.

For power-dependent PL measurement, the excitation laser intensity F was varied from 10^{-3} to 5×10^{-1} W/cm^2 using neutral density filters.

The volume sampled by PL spectroscopy is typically on the order of several hundreds of μm^3 depending on the exciton diffusion length. Therefore, the PL spectrum averages out the contributions of regions with defects and without defects. The spectral resolution of the monochromator is 0.008 nm. In this thesis, energy values -in eV- are given with 4 significant decimals; wavelengths -in nm- are given with 2 significant decimals. Depending on the sharpness of the optical transition, only one significant decimal may be used for the wavelength. Throughout this study, the following relationships between photon energy E and wavelength λ are used:

$$E = \frac{hc}{\lambda} \tag{3.23a}$$

$$\frac{\Delta\lambda}{\lambda} = -\frac{\Delta E}{E} \tag{3.23b}$$

3.6.3 Hall analysis

Combined conductivity and Hall voltage measurements are widely used methods for quantitative evaluation of electrical properties of semiconductors. Hall-effect analysis was performed using the Van der Pauw geometry[165-166] illustrated in Fig. 3.6. The validity of the method requires uniformly thick films of connex topology. For 0.5 cm^2 square samples, triangular contacts with a size around 0.5 mm introduce an error less than 1% for resistivity measurements and about 7% for Hall voltage measurements.[167] The finite-

contact-size issue is the reason why other geometries have been proposed to improve on the accuracy of electrical measurements.[168]

The conductivity σ is determined by eight measurements of voltage without magnetic field.

The apparent carrier concentration n_H (or p_H) is determined by eight measurements of voltages, four under a positive magnetic field ($+B$) and four under a negative magnetic field ($-B$). These eight measurements are needed to eliminate undesired voltages arising from misalignment (V_M), Seebeck (V_S), Nernst (V_N), Righi-Leduc (V_R) and Ettingshausen (V_E) effects.[168] The Ettingshausen voltage cannot be eliminated; in ZnO, its contribution is usually negligible.[169] Refer to Table 3.1 for more details.[169]

The carrier type is determined by the sign of the averaged Hall voltage (V_H). Resistive samples tend to produce weak signals on the order of μV. Artificial voltage spikes can significantly impact the final Hall voltage and give considerable scatter of the data. Other issues may arise from mixed conduction, photoconductivity or surface conduction effects. Surface conduction usually results in the Hall coefficient going through a minimum.

The Hall mobility μ_{H} is derived from n_H (or p_H) and σ:

$$n_H\ (or\ p_H) = \frac{\sigma}{e\mu_{\mathrm{H}}} \tag{3.24}$$

It is convenient to set the Hall factor equal to 1 so that the drift mobility μ equals the Hall mobility μ_{H}, and the carrier concentration n (or p) equals the apparent carrier concentration n_H (or p_H).

Hall analysis at low temperature yields quantitative information about the electrically active impurities and scattering mechanisms in a semiconductor.[170] The temperature dependence of the carrier concentration is determined by the ratio of the acceptor level density, N_A, to the donor level density, N_D, *i.e.* the compensation ratio, and the activation energies of each level. It can be fitted by solving the charge balance equation (CBE):[169]

$$n + \sum_k N_{Ak}^{-} = p + \sum_k N_{Dk}^{+} \tag{3.25}$$

where n and p are the electron and hole concentrations, and N_{Ak}^{-} and N_{Dk}^{+} are the concentrations of single ionized acceptors and donors.

The temperature dependence of the drift mobility provides information on the mechanisms scattering the free carriers. The drift mobility can be expressed as a function of the scattering relaxation time τ:

$$\mu = \frac{e}{m_e^*}\frac{\langle \tau^2 \rangle}{\langle \tau \rangle} \tag{3.26}$$

where:[169]

$$\langle \tau^k \rangle = \frac{\int_0^{+\infty} \tau^k(E) E^{\frac{3}{2}} e^{-\frac{E}{kT}} dE}{\int_0^{+\infty} E^{\frac{3}{2}} e^{-\frac{E}{kT}} dE} \tag{3.27}$$

The relative strength of each scattering mechanism determines the temperature dependence of the total drift mobility. The various mobility components of interest in this work are described in Appendix B. The theoretical Hall mobility of bulk ZnO given by Eq. (B.8) is plotted in Fig. 3.7(a) along with its five scattering components, assuming a two-donor and one-acceptor model to fit the CBE and N_{DIS}=10^4 cm^{-2}, N_A=10^{14} cm^{-3} and $n(300)$=10^{15} cm^{-3}. The effect of dislocation scattering on the total Hall mobility is shown in Fig. 3.7(b). Dislocation scattering can no longer be ignored when N_{DIS}>10^8 cm^{-2} as phonon scattering progressively vanishes under the effect of increasing dislocation scattering.

The Hall measurement set up uses a Keithley 220 programmable current source and a Hewlett Packard 6517A high input impedance voltmeter. The magnetic field is 0.22 T. A commercial MMR apparatus equipped with a 0.67 T permanent magnet and supplied by IMRA America was also used. The angle between the sample surface normal and the magnetic field is 90 deg.

Ohmic contacts to the ZnO films were made with pressed indium annealed at 300 °C under N_2 flow. Au leads were attached to the indium contacts for convenient contacting with the cryostat and MMR station wires.

3.7 Device fabrication and testing

The ZnO mesas were fabricated by Weiming Wang in three steps including two metal lift-off steps and one mesa etching step. The metal lift-off process sequence can be described as follows: the surface of the homojunction is cleaned following a standard procedure and baked at 150 °C for 2 minutes to rid the surface of solvent residues. A hexamethyldisilazane ($[CH_3Si]_2NH$) preparation is spin-coated (Solitec 5110) for 30 seconds at 4000 rpm in atmosphere onto the homojunction surface to promote photoresist adhesion. A 1 μm-thick negative photoresist (AZ-5214) is spin-coated for 30 seconds at 3000 rpm. A soft-bake 5 to 10 °C below the photoresist crosslinking temperature (105 °C in this process) is conducted to remove solvents and cure the photoresist. The photoresist is then exposed to 20 mW/cm^2 UV light (Cl_2, 405 nm) for 4 sec using a Karl Suss MJB-3 mask aligner. A post-exposure bake is carried out at 115 °C for three minutes. This step, critical for "image reversal", is used to cross-link the photoresist and eliminate its photo-sensitivity. It is followed by a flood exposure step to make the masked areas soluble to the developer solution (MF-319). The sample is then immersed in the MF-319 developer to remove the soluble photoresist. Metal electrodes are sputtered onto the exposed ZnO surfaces: 20 nm / 80 nm for Ti / Au on *n*-type ZnO and 20 nm / 80 nm Ni / Au on *p*-type ZnO and lifted off in acetone for 10 minutes. The residual photoresist is dissolved in acetone in a regular glass beaker and the homojunction cleaned following a standard procedure.

For mesa-etching, the above sequence is identical until electrode sputtering. After development, the ZnO exposed area is etched in HF (JT Baker, 49%, electronic grade). The etch-rate was found to be strongly dependent on the microstructure of the film, typically between 50 nm / min to 300 nm / min. Highly dislocated films were found to etch faster. Following etching, the sample was cleaned following a standard procedure.

The current-voltage characteristics were collected using a probe station connected to a Keithley 236 source-measure unit able to source voltage and measure current or vice versa.

Table 3.1 Dependences of various undesired voltages on current polarity and magnetic field orientation.

Current polarity	B	V_H	V_M	V_S	V_E	V_N	V_R
+	+	+	+	+	+	+	+
+	-	-	+	+	-	-	-
-	+	-	-	+	-	+	+
-	-	+	-	+	+	-	-

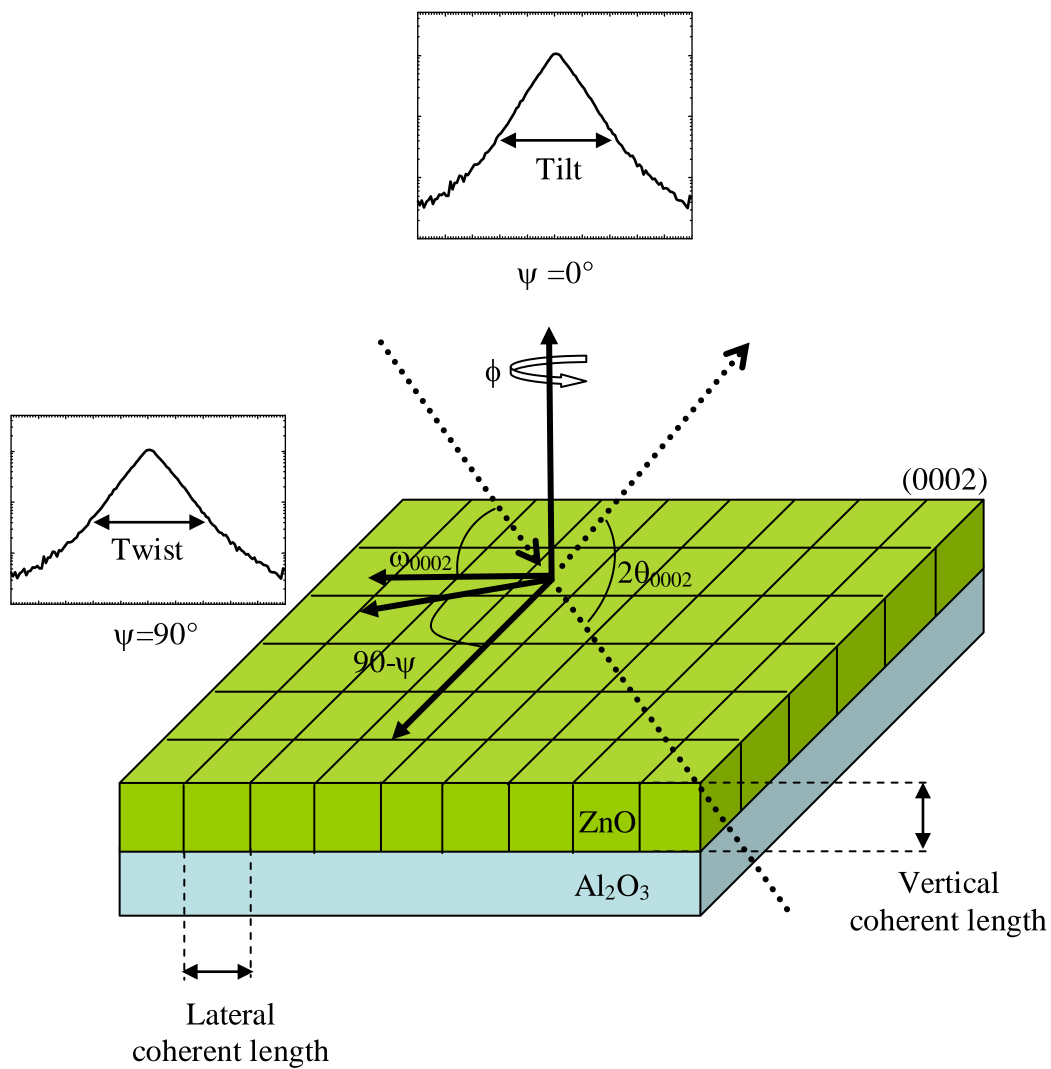

Figure 3.1 Illustration of the tilt and twist distributions for a mosaic ZnO film grown on (0001) Al_2O_3.

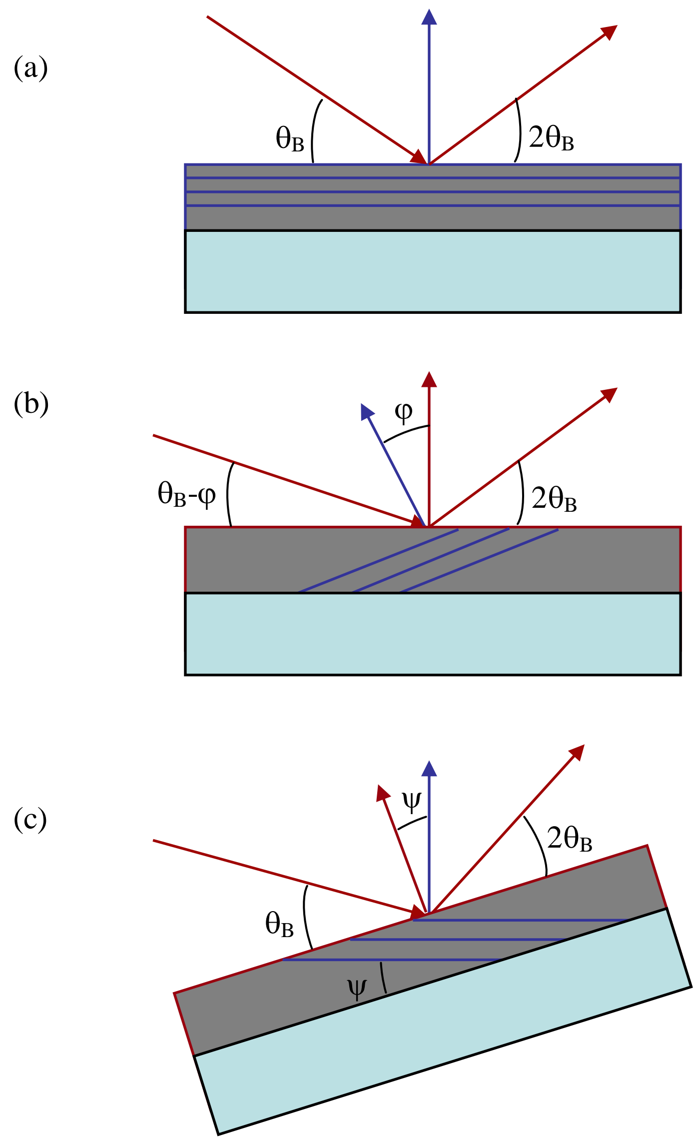

Figure 3.2 Illustration of the (a) symmetric, (b) glancing incidence asymmetric and (c) skew symmetric XRD geometries.

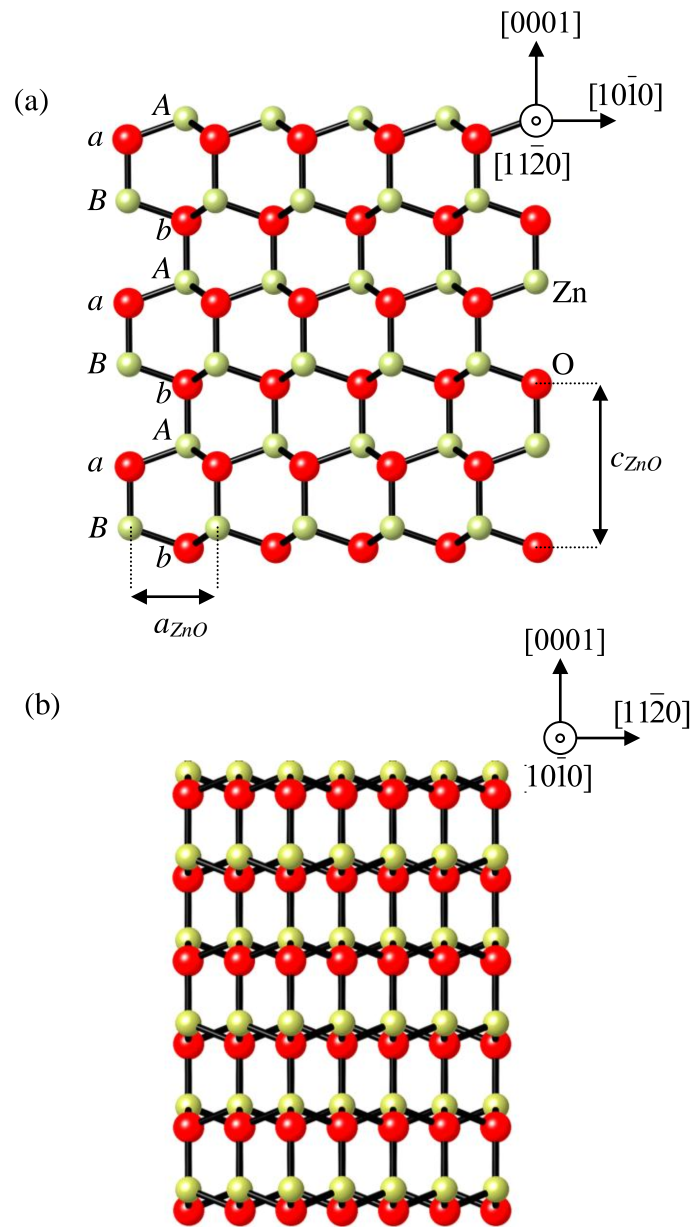

Figure 3.3 Hexagonal wurtzite structure viewed along (a) $[11\text{-}20]_{ZnO}$ and (b) $[10\text{-}10]_{ZnO}$.

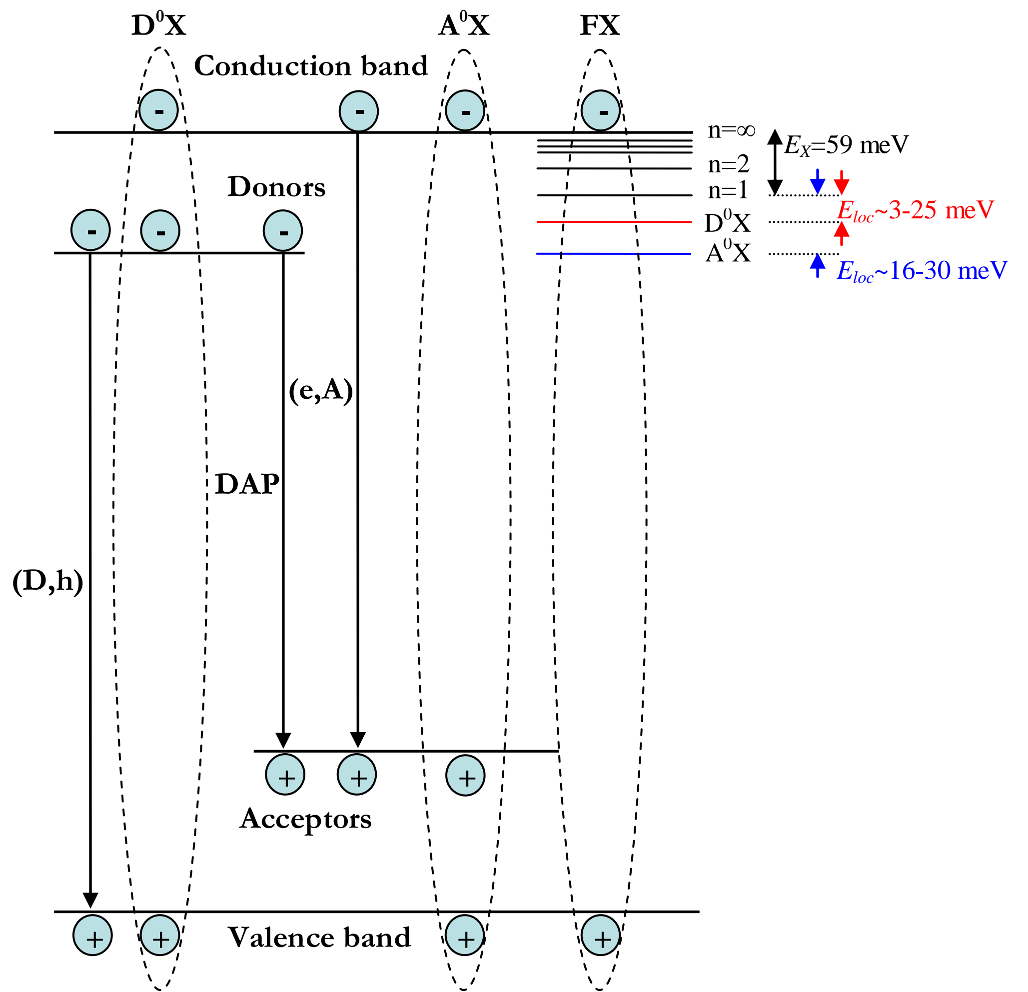

Figure 3.4 Band diagram illustrating the radiative transitions of interest in this work.

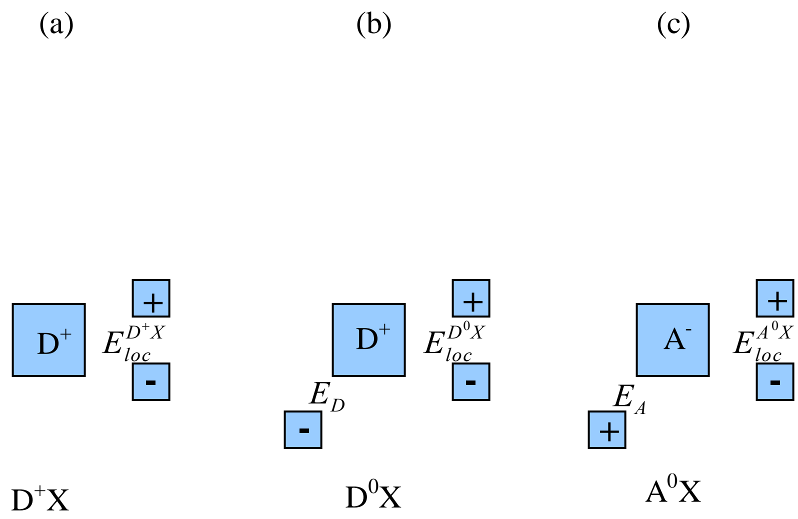

Figure 3.5 Illustrations of excitons bound to (a) an ionized donor D^+, (b) a neutral donor D and (c) a neutral acceptor A.

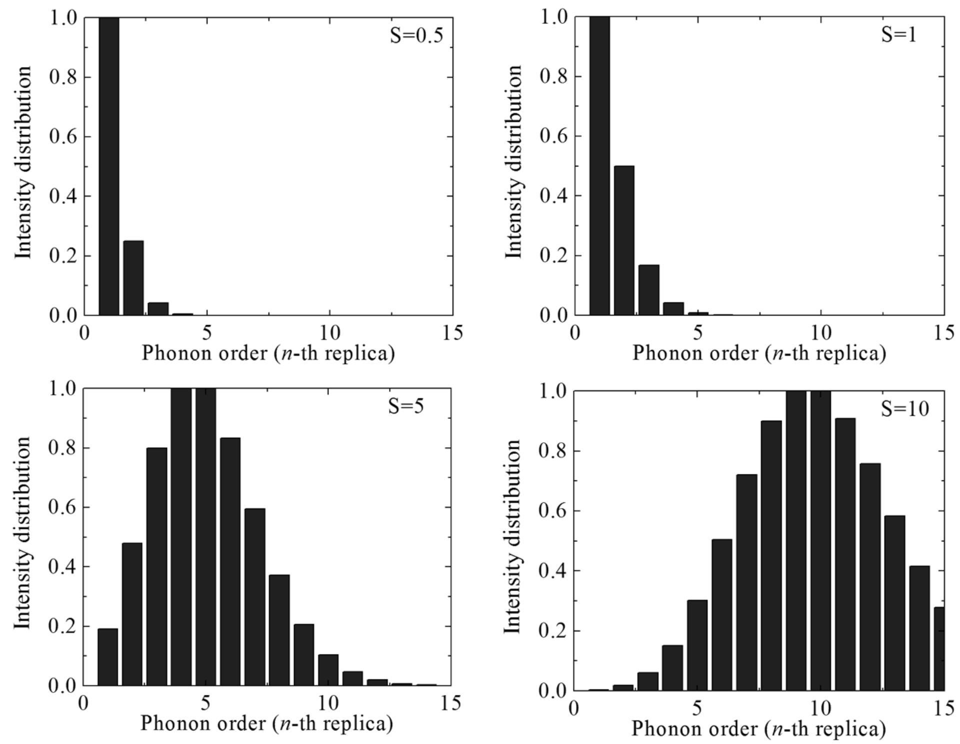

Figure 3.6 Intensity distributions of phonons assuming Huang-Rhys factors of (a) 0.5, (b) 1, (c) 5 and (d) 10.

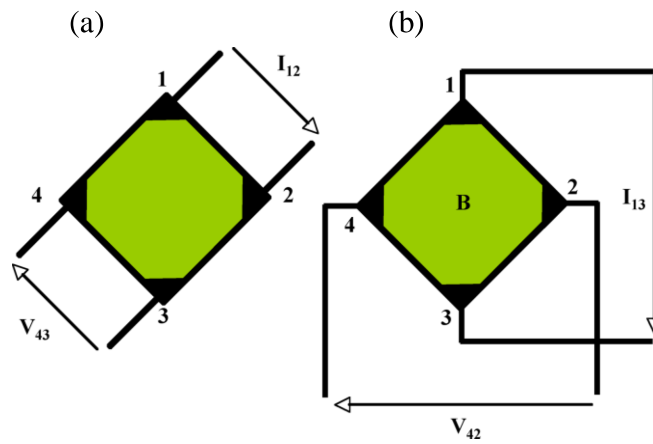

Figure 3.7 Van der Pauw geometry used for (a) conductivity and (b) Hall voltage measurements.

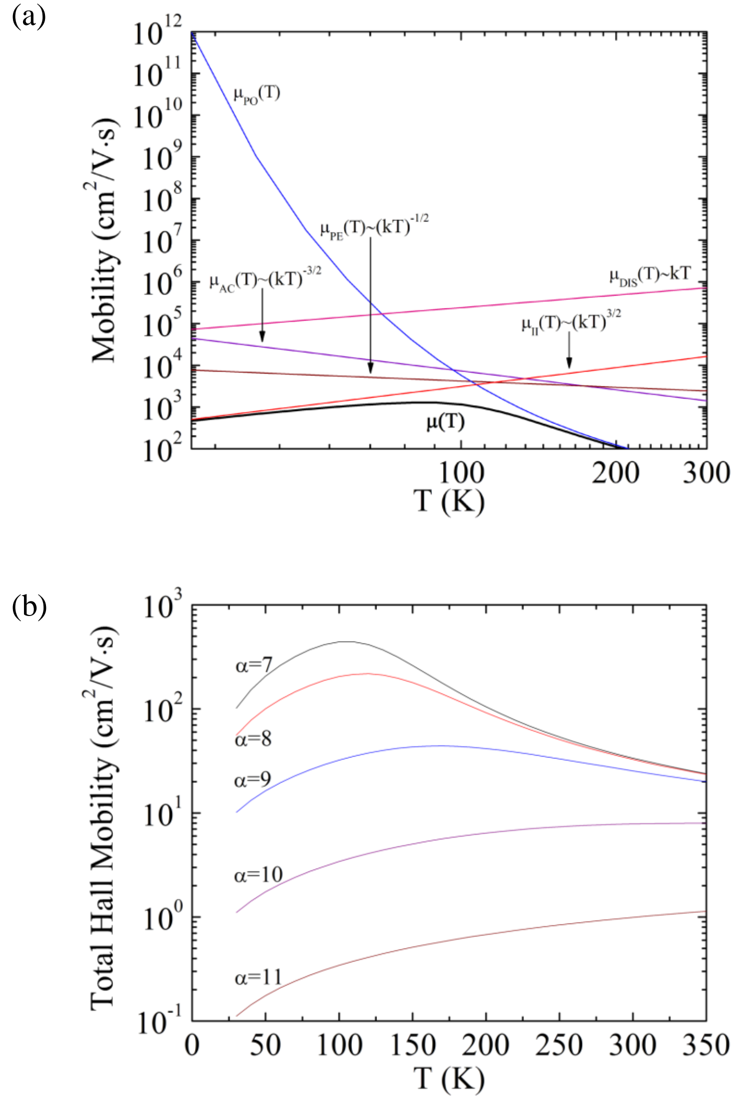

Figure 3.8 (a) Theoretical Hall mobility in bulk ZnO assuming n(300)=10^{15} cm^{-3}, N_A=10^{14} cm^{-3}, N_{DIS}=10^4 cm^{-2}, and a two-donor and one-acceptor model to fit the charge balance equation. The five scattering mobility components used in this work are also represented. (b) Effect of increasing dislocation density N_{DIS}=10^{α} cm^{-2} on the total Hall mobility.

Chapter 4

Synthesis and Optoelectronic Properties of Nitrogen-Doped ZnO Films

4.1 Introduction

Because the valence band maximum lies close to the *p*-type pinning energy, ZnO is relatively resistant to shallow acceptor doping.[57] Despite recent reports of ZnO-based light-emitting devices,[73] the fabrication of *p*-type ZnO using nitrogen as dopant is still limited by various issues such as the low solubility of nitrogen, compensation due to the intrinsic band structure of ZnO,[49,56] and passivation by hydrogen.[68] Theoretically, the substitution of oxygen by nitrogen gives the shallowest acceptor among group-V elements, with an activation energy of 400 meV.[77] Because of compensation and passivation issues, a high nitrogen concentration is required in order to produce hole concentrations on the order of 10^{17}-10^{18} cm^{-3}. Yet, there is a marked trade-off between nitrogen solubility and crystallinity since ZnO films of good epitaxial quality require high growth temperatures while the nitrogen solubility generally decreases with the growth temperature.

Nitrogen-doped ZnO films have been fabricated by various methods. Plasma-assisted growth, which relies on the dissociation of nitrogen gases such as N_2, N_2O or NO, has been in some cases successful in fabricating *p*-type ZnO.[73,78] However, the competitive kinetics between reactions involving nitrogen and its radicals during growth results most of the time in the incorporation of undesired nitrogen-related donors such as $(N_2)_O$ or N_O-$(N_2)_O$.[83,171] Electron paramagnetic resonance studies have also shown that molecular nitrogen (N_2^-) can act as an acceptor in ZnO crystals,[172] illustrating the difficulty in controlling how nitrogen distributes in ZnO.

As an alternative to plasma-assisted growth, oxidation of Zn_3N_2 has been used to

fabricate nitrogen-doped ZnO films,[173] however the film crystallinity and the reproducibility of the *p*-type conductivity were poor.

This chapter reports the fabrication of *p*-type ZnO thin films by pulsed laser ablation of a Zn-rich Zn_3N_2 target with which the low nitrogen solubility issue can be overcome.[174] The target choice is determined by the kinetics of pulsed laser ablation. Briefly, because of the characteristically high kinetic energies of the plume ions, nitrogen-doped epitaxial ZnO films can be grown directly on Al_2O_3 at low temperatures. Nitrogen concentrations as high as 10^{20} atoms/cm^3 are measured in the films grown at 300 °C and decrease by two orders of magnitude when the growth temperature is further increased to 500 °C. While all as-grown ZnO films show *n*-type conductivity, the films deposited at 300 °C and annealed in oxygen at 600 °C become *p*-type. To understand these observations, the microstructures of both undoped and nitrogen-doped samples were studied by transmission electron microscopy (TEM). It was found that the *p*-type films consist of columnar grains with a high density of defects within the grains while the films grown at 400 °C under the same conditions have more homogeneous microstructures. Results of low-temperature photoluminescence (PL) and Hall-effect measurements of N-doped ZnO and undoped ZnO films are compared to delineate the effects of nitrogen doping. Two doping-induced acceptor levels are evidenced in *p*-type samples.

Thermal gravimetric analysis (TGA) and temperature-dependent X-ray diffraction (XRD) were used to investigate the thermal stability of the Zn_3N_2 powder in air. Figure 4.1(a) shows that the Zn_3N_2 phase gradually transforms into ZnO above 500°C in synthetic air, while it decomposes into Zn metal in nitrogen ambient. Temperature-dependent XRD measurements shown in Fig. 4.1(b) are consistent with the TGA results. The Zn_3N_2 anti-bixbyite phase gradually transforms into the zincite phase at around 550 °C in air. A 20 at% Zn-doped Zn_3N_2 pellet was therefore sintered at 500 °C for 8 h in air. Zinc powder was added to consolidate the target during firing and to create zinc-rich growth conditions, which favor nitrogen incorporation.[77] The epitaxial films discussed in this study were deposited on (0001) Al_2O_3 substrates in 5 mtorr O_2 at a rate of 5 Å/s and had thicknesses of 300-500 nm. For comparison purposes, undoped ZnO films were fabricated by laser ablation of an undoped ZnO target under the same growth conditions.

The substrate temperatures during growth were 300 °C and 400 °C.

4.2 Nitrogen solubility in heteroepitaxial ZnO films

The nitrogen concentration was determined by secondary-ion mass spectroscopy (SIMS). The data was calibrated by simultaneous measurement of a nitrogen-implanted reference sample. Figure 4.2(a) shows the SIMS measurement of a *p*-type sample deposited at 300 °C. The sample is uniformly doped at a nitrogen concentration of about 9.5×10^{19} at/cm^3. The nitrogen concentration was also measured by nuclear reaction analysis (NRA). NRA has been widely used to depth-profile hydrogen in semiconductors due to its ability to detect light elements.[141] The nuclear reaction used was $^{14}N(d,\alpha)\ ^{12}C$. NRA results are in good agreement with the SIMS results: as shown in Fig. 4.2(b), the concentration of nitrogen in the films decreases from 1.5×10^{20} at/cm^3 to about 10^{18} at/cm^3 as the growth temperature is increased from 150 °C to 400 °C. At growth temperatures above 400 °C, the nitrogen concentration was below the SIMS sensitivity limit for nitrogen (10^{17} cm^{-3}). The observation that the nitrogen solubility rapidly decreases when the growth temperature increases is consistent with Ref. 175. It shows that both the solubility and mechanism of incorporation of nitrogen depend on the film microstructure, which itself is a strong function of the growth temperature (see section 4.4).

4.3 Effect of nitrogen doping on the optoelectronic properties of ZnO

Table 4.1 summarizes the electrical properties at room temperature of nitrogen-doped and undoped ZnO samples, before and after annealing in 1 atm. O_2 for one hour. As-deposited nitrogen-doped ZnO samples show *n*-type conductivity. Films deposited at 300 °C have mobilities typically less than 1 cm^2/V·s whereas those deposited at 400 °C have mobilities comparable with those of undoped ZnO (~25 cm^2/V·s). The ZnO films deposited at 300 °C, followed by annealing at 600 °C in O_2, are *p*-type with a resistivity of 28 Ω·cm, a mobility of 0.5 cm^2/V·s and a hole concentration of 4.9×10^{17} cm^{-3}. These electrical properties are reasonable in comparison with other reports.[73,78] The films deposited at 400 °C remain *n*-type after annealing.

The reasons for the large nitrogen solubility and the moderate level of hole conduction in our nitrogen-doped ZnO films may come from the kinetics of pulsed laser

deposition (PLD). Extensive experimental and theoretical studies of PLD have shown that in addition to electrons and ions, the laser-induced plume also contains clusters of the target material of different sizes.[129] Kukreja *et al.* used time of flight spectroscopy to demonstrate the existence of $(ZnO)_n$ clusters, with n up to 20, in a plume induced by ultraviolet laser ablation of ZnO at a fluence of 0.12 J/cm^2.[176] One unique aspect of our growth process comes from the ablation of the Zn-doped Zn_3N_2 target, which creates Zn-N clusters in the plume. These clusters can directly incorporate the ZnO film while it grows and contribute to the formation of the desired Zn-N bonds, which are otherwise difficult to form due to the larger electronegativity difference between Zn and O. Since O is more electronegative than N, the film grows as ZnO. On the other hand, the film contains N-N and N-O bonds, which can act as compensating donors.[177]

Temperature-dependent measurements of the carrier concentration in *n*-type and *p*-type films are shown in Fig. 4.3(a). The measured electron concentration in *n*-type samples is nearly independent of temperature in the range considered, indicating that the material is degenerate. The charge balance equation (CBE) was used to fit $n(T)$. For an *n*-type sample, assuming a single acceptor / multiple (m) donor model, and $n >> p$:[169]

$$n(T) + N_A = \sum_{i=1}^{m} \frac{N_{D_i}}{1 + \frac{n(T)}{\phi_i(T)}} \tag{4.1}$$

where N_A is the residual acceptor level density, N_{D_i} are the donor concentrations and, under the assumption that the donor activation energies are temperature independent:

$$\phi_i(T) = \frac{g_{0\,i}^n}{g_{1\,i}^n} N_c^{'} T^{\frac{3}{2}} e^{-\frac{E_{D\,i}}{kT}} \tag{4.2}$$

$$N_c^{'} = 2\frac{(2\pi m_e^* k)^{\frac{3}{2}}}{h^3} \tag{4.3}$$

Assuming $m=1$, the fit gave N_D=5.5×10^{19} cm^{-3}, N_A=10^{16} cm^{-3} and a very shallow donor level (E_D<< 1 meV), suggesting that the Fermi level lies in the conduction band. The activation energy (E_A) of the acceptor in *p*-type samples can be determined by a fit to $p(T) \propto T^{3/2} \exp(-E_A / kT)$.[169] The least-squares fit between 100 K and 300 K shown in Fig. 4.3(a) gives E_A=105±5 meV, a value consistent with recent reports,[71] yet much smaller than that predicted by theory.[77] Note that this result is consistent with the

hydrogenoid model of the acceptor dopant, which under the effective mass approach gives an acceptor activation energy E_A equal to:

$$E_A = \frac{R_y}{\varepsilon_s^2}\frac{m_h^*}{m_o} = 105\,meV \tag{4.4}$$

A 105 meV acceptor corresponds to an ionization ratio of 1.7×10^{-2}, which is slightly larger than $[p]/N = 5\times10^{-3}$, suggesting compensation of the hole carriers, in agreement with Ref. 177. The identity of such acceptor is unknown at this point.

The temperature dependences of the Hall mobility are shown in Fig. 4.3(b). Scattering in *n*-type nitrogen-doped ZnO grown at 400 °C is dominated by impurity scattering, which is consistent with the high dopant concentration measured by SIMS. In contrast, the hole mobility in *p*-type films grown at 300 °C decreases throughout the whole temperature range. According to the Petritz model,[178] the grain boundary scattering-dependent mobility satisfies $\mu(T)\sqrt{T} \propto \exp[-E_B/kT]$, where E_B is the energy of the potential barrier created between two crystallographic grains. As shown in Fig. 4.3(c), a good fit to the mobility can be obtained between 200 K and 300 K using the Petritz model with E_B=14±2 meV. The physical meaning of the potential barrier is difficult to interpret based on the high density of defects in the films, which can also act as scattering sources. Yet, because the material contains a high density of grains with narrow lateral coherent lengths (see section 4.4), it is reasonable to assume that grain boundary scattering is the dominant scattering source at high temperatures.

Photoluminescence spectra, at 6 K, of undoped ZnO, as-grown nitrogen-doped ZnO and *p*-type nitrogen-doped ZnO fabricated at 300 °C are compared in Fig. 4.4. The PL spectrum of undoped ZnO is dominated by three recombination lines at 368.2 nm (3.3673 eV), 368.5 nm (3.3646 eV) and 368.9 nm (3.3609 eV) assigned to donor-bound excitons. The free A-exciton at 366.7±0.1 nm (3.3811 eV) and B-exciton at 365.4±0.2 nm (3.3931 eV) are observed. The PL spectrum of *n*-type N-doped ZnO spectrum is dominated by two D^oX transitions at 367.9 nm (3.3701 eV) and 368.5 nm (3.3646 eV) accompanied by a pronounced transition at 371.7 nm (3.3356 eV). This transition can be assigned to a *Y*-line or to a two-electron transition associated with the ground state of a D^0X. The associated donor activation energy E_D=47±2 meV was calculated using Eq. (3.12).

The D^oX transitions were found to quench at 70 K. The thermal decay of the integrated intensity of the D^oX recombination line was fitted between 6 K and 70 K to a single Arrhenius process using:

$$\frac{I_{DX}}{I_o} = \frac{1}{1 + C\exp(-\frac{E}{kT})} \qquad (4.5)$$

A fitting parameter of C=2.5×10^2 and a localization energy (E_{loc}) of 14.6 meV were found. Based on Haynes rule for donors,[70,150] the donor activation energy E_D can be calculated from:

$$E_D = \frac{E_{loc} - a}{b} \qquad (4.6)$$

where a=-3.8 meV and b=0.365. Calculations give E_D=50.4 meV in good agreement with the previous calculation.

After annealing, the integrated intensity of the D^oX transition quenched and broadened dramatically and a pronounced recombination line having an intensity stronger than that of the D^oX line and peaking at ~396.0 nm (3.1309 eV) is observed. A second broad, yet weaker, transition can be distinguished at around 377.3 nm (3.2861 eV).

As discussed in section 3.6.2.4, a characteristic of DA transitions is that they blueshift under increasing excitation intensity. The emission maximum of the 396.0 nm band was found to shift to the blue with increasing excitation. The transition was assigned to a DA transition involving nitrogen. This observation demonstrates the successful introduction of an acceptor in the epilayer. There have been several reports of DA recombination in nitrogen-doped ZnO samples,[152-155] and activation energies of 165-266 meV have been calculated for the nitrogen acceptor. The acceptor binding energy E_A can be determined from the energy position of the DAP under the approximation of zero Coulomb energy ($r \rightarrow \infty$). Graphically, $E_{DAP}(\infty)$=3.106±0.03 eV can be determined, which using Eq. (3.16) gives E_A=280±30 meV, in good agreement with Ref. 179. A 280 meV acceptor corresponds to an ionization ratio of 1.9×10^{-5} at room temperature, which is less than the calculated ionization ratios based on Hall-measurement results, suggesting that a shallower acceptor may also generate holes.

The 377.3 nm transition was also assigned to a donor-acceptor transition. Graphically, $E_{DAP}(\infty)$=3.284±0.01 eV was determined, corresponding to E_A=102±10 meV. This result is consistent with the activation energy determined by temperature-dependent Hall-effect measurements. It also supports the relatively low hole concentration measured in the films since according to the intensities of the DA recombinations, the shallowest acceptor is also the least abundant one.

No acceptor-bound excitonic transition was observed in *p*-type ZnO. It is obvious that the presence of acceptors in a semiconductor, intentional or not, will systematically produce DA recombinations. The concept of neutral acceptor-bound excitons (A^0X) in ZnO is however very different and still under extensive debate. Experiments show that acceptors in ZnO tend to be deep,[179-182] and therefore unlikely to localize an exciton. Even if they did, the bound exciton would be relatively stable against recombination. Finally, rigorous analysis of A^0X transitions, *i.e.* the unambiguous distinction between D^0X and A^0X transitions, calls for magnetic resonance spectroscopy based on the Zeeman effect. However, the Zeeman splitting is relatively hard to measure experimentally in ZnO films doped heavily with acceptors.[70]

4.4 Effect of nitrogen doping on the crystallinity and microstructure of ZnO

Figure 4.5(a) shows a θ-2θ scan of the *p*-type sample deposited at 300 °C. All reflection peaks correspond to the basal planes of ZnO and Al_2O_3. No peaks from other ZnO planes or impurity phases (such as Zn_3N_2 or Zn) were detected. These results demonstrate that nitrogen-doped ZnO films are directly fabricated on the sapphire substrate, in contrast with Ref. 173 and 183 where polycrystalline films are obtained from oxidation of the Zn_3N_2 phase. The full-width at half-maximum (FWHM) value of the ZnO 0002 rocking curve was respectively 0.79° and 0.54° when the substrate temperature was 300 °C and 400 °C.

ϕ-scan measurements of the ZnO $11\bar{2}4$ reflection shown in Fig. 4.5(b) show the six-fold symmetry of the wurtzite structure and an in-plane broadening of 3.7°. The degree of in-plane rotation between the ZnO and Al_2O_3 lattices was found to be 30°, corresponding to a $[2\bar{1}\bar{1}0]_{ZnO} \| [10\bar{1}0]_{Al_2O_3}$ and a lattice mismatch of 18.4 %. The epitaxial orientation relationship between ZnO and Al_2O_3 is determined as:

$(0001)[2\bar{1}\bar{1}0]_{ZnO} \| (0001)[10\bar{1}0]_{Al_2O_3}$ and schematized in Fig. 4.6, where it is seen that the hexagonal zinc plane in ZnO matches the oxygen sublattice of sapphire.

From the XRD studies, it can be concluded that the epitaxial quality of our *p*-type nitrogen-doped sample is much higher than that of films produced by oxidation of Zn_3N_2,[173,183,184] which are either polycrystalline or textured out-of-plane with 0002 rocking curves broader than 2°. It is difficult to understand how such polycrystalline films doped with high concentrations of nitrogen can produce hole mobilities as high as 91.5 $cm^2/V \cdot s$[183] or 111 $cm^2/V \cdot s$.[184] In our work, pulsed laser ablation of a Zn-rich Zn_3N_2 target in an O_2 environment appears to be a reliable method of fabricating single phase, epitaxial ZnO films uniformly doped with nitrogen.

The observed microstructures are consistent with the measurements of the Hall mobility in *n*- and *p*-type films. Figure 4.7(a) is a cross-sectional TEM image of the *p*-type N-doped ZnO film deposited at 300 °C. It can be seen that the microstructure consists of columnar grains having widths of 10-20 nm. The grains are slightly tilted with respect to each other and account for the more pronounced mosaicity observed by X-ray diffraction. The grain boundaries and the high density of defects within the grains account for the low mobility electrical transport as they provide additional scattering centers. In addition, these may explain the level of nitrogen doping (10^{20} at/cm^3) as the nitrogen atoms may be pinned at the high-energy internal surfaces induced by planar defects such as boundaries. In contrast, the microstructure of nitrogen-doped ZnO samples grown at 400 °C and above is relatively uniform and does not show a high density of grains (Fig. 4.7(b)). Rather, the films consist of threading dislocations formed due to the large lattice mismatch between ZnO and Al_2O_3.

These studies reveal that nitrogen causes significant microstructural changes by itself. One possible reason for the differences in microstructure and nitrogen concentration is the thermal stability of the Zn-N bond. Most Zn-N bonds decompose on heating at the substrate surface at T_G=400 °C so that Zn preferentially binds with O, leaving less than 10^{17} cm^{-3} nitrogen atoms in the film. This is consistent with the temperature-dependent XRD measurements of Zn_3N_2 powder. In contrast, at T_G=300 °C, the Zn-N clusters at the substrate surface are stable and segregate to the boundaries between ZnO grains, resulting in a ZnO film doped with nitrogen.

According to Ref. 58, the films deposited at 300 °C may contain shallow Zn_i-N_O donor complexes, which on annealing in O_2 decompose into Zn interstitials and N_O acceptors. The decomposition is driven by the high mobility of interstitial zinc in ZnO. The onset of *p*-type conductivity after annealing may thus originate from the gettering of zinc interstitials at crystal defects such as grain boundaries, and the ionization of N_O acceptors. A comparison between the microstructures of films deposited at 300 °C and 400°C reveals that highly defective microstructures can produce low-mobility hole transport because of numerous and complex interactions between extended defects, donors and acceptors. While the 105 meV acceptor is likely to be the N_O substitutional, the identity of the 280 meV defect is unknown at this point.

4.5 Conclusions

In conclusion, nitrogen-doped *p*-type ZnO epitaxial films were fabricated by pulsed laser ablation of a Zn-doped Zn_3N_2 target. The films deposited at 300 °C are uniformly doped with 10^{20} nitrogen at./cm^3. While as-grown films are degenerate *n*-type, films deposited at 300 °C and annealed at 600 °C in O_2 are *p*-type with a resistivity of 28 Ω·cm, a mobility of 0.5 cm^2/V·s and a hole concentration of 4.9×10^{17} cm^{-3}. At least two doping-induced acceptor levels at 105 and 280 meV were identified in *p*-type nitrogen-doped ZnO. Transmission electron microscopy studies show that the microstructure of N-doped ZnO deposited at 300 °C consists of columnar grains. The onset of *p*-type conductivity after annealing may originate from gettering of zinc interstitials at grain boundaries and ionization of nitrogen acceptors. In terms of stability, the *p*-type films suffer from photoconductivity issues, most likely because of the abundance of the deep 280 meV nitrogen-induced level. The resistivity changes by as much as 20% under room light exposure and the carrier type can fluctuate because of the generation of electron-hole pairs. The applicability of such *p*-type material into optical devices is questionable because the reliability of the device would have to depend on the level of hole conduction. These conclusions stimulate the search for a better acceptor, such as phosphorus. Chapter 5 focuses on the effects of phosphorus doping on the microstructure and optoelectronic properties of ZnO.

Table 4.1 Room-temperature electrical properties of undoped and N-doped ZnO films before and after annealing in O_2 at 600 °C. Each sample is 0.5 μm-thick.

Sample	T_G (℃)	*Carrier type*	*Resistivity (Ω·cm)*	*Carrier density (cm^{-3})*	*Hall mobility ($cm^2/V{\cdot}s$)*
ZnO as-grown	300	*n*	2.8×10^{-2}	1.5×10^{19}	15
NZO as-grown	300	*n*	2.3×10^{0}	1.0×10^{18}	2.7
NZO annealed	300	*p*	2.8×10^{1}	4.9×10^{17}	0.5
ZnO as-grown	400	*n*	7.0×10^{-1}	3.2×10^{17}	28
NZO as-grown	400	*n*	9.0×10^{-2}	3.0×10^{18}	23
NZO annealed	400	*n*	1.7×10^{0}	1.7×10^{17}	22

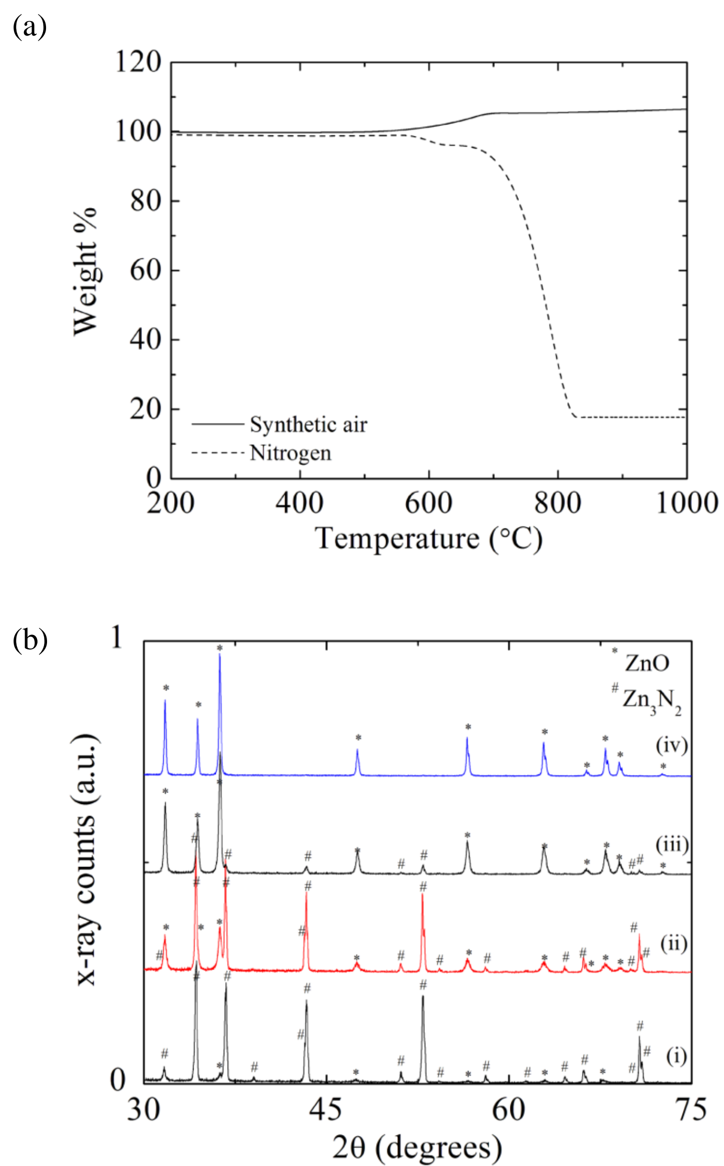

Figure 4.1 (a) Thermal gravimetric analysis of Zn_3N_2 powder in air and nitrogen atmospheres. (b) Temperature-dependent X-ray diffraction measurements conducted in air. The (i), (ii), (iii) and (iv) traces correspond to Zn_3N_2 powder annealed at 500°C, 550°C, 650°C and 750°C respectively.

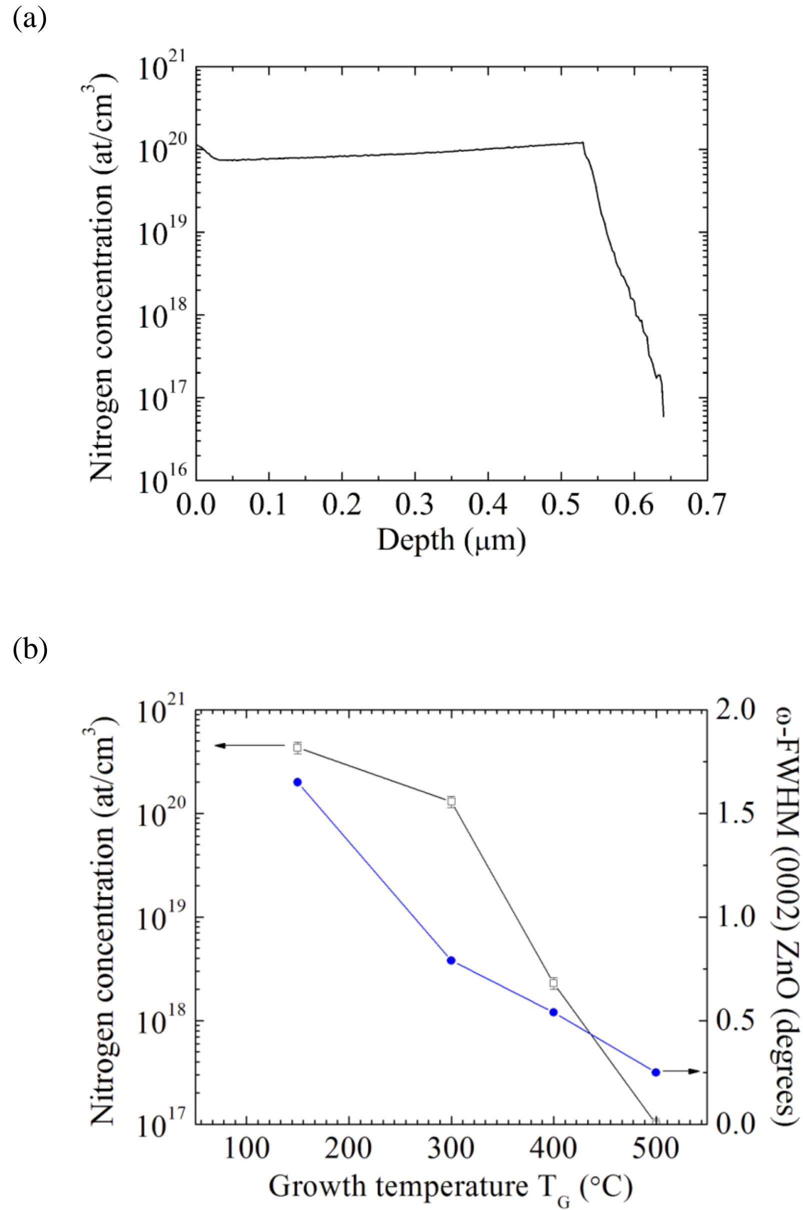

Figure 4.2 (a) Secondary-ion mass spectroscopy of nitrogen in a 500 nm-thick *p*-type nitrogen-doped ZnO fabricated at 300°C. (b) Dependence of the nitrogen solubility in ZnO (open squares) and film crystallinity (circles) on the growth temperature, according to NRA and 0002 ZnO rocking curve measurements. The experimental error intrinsic to the NRA measurement is about 10%.

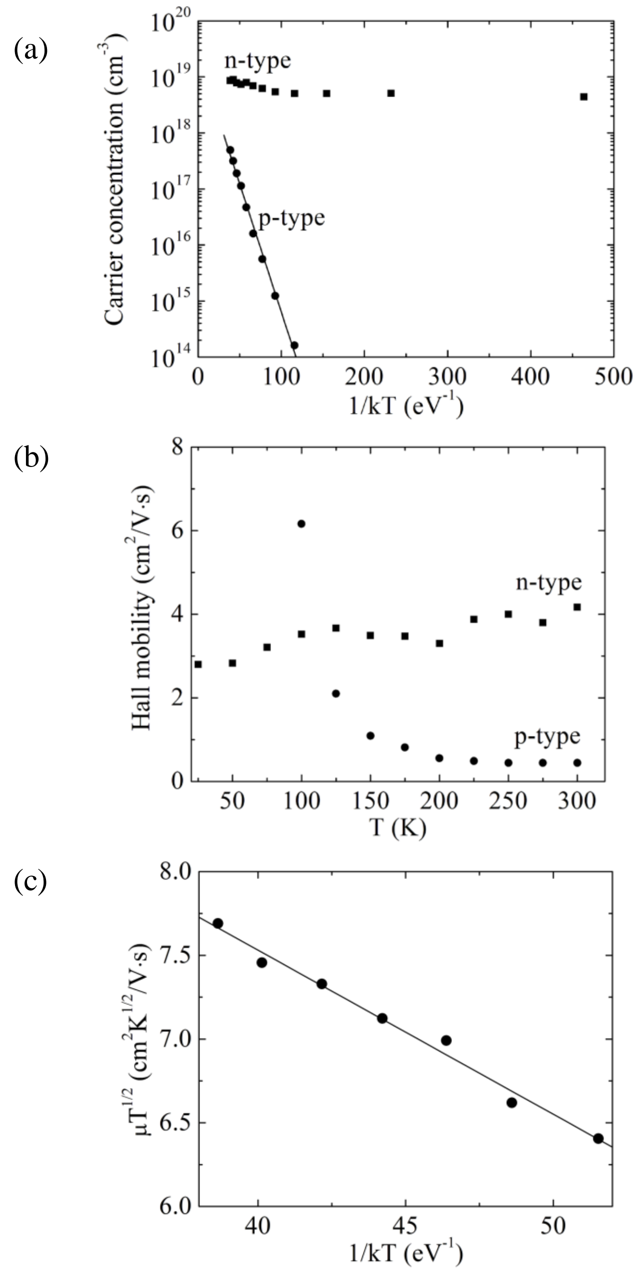

Figure 4.3 (a) Temperature dependences of the carrier concentration in *n*-type (squares) and *p*-type (circles) nitrogen-doped samples. The least-squares fit to the hole concentration in *p*-type ZnO yields E_A=105±5 meV. (b) Temperature dependences of the Hall mobilities. (c) Fit to the Hall mobility of a *p*-type sample using the Petritz model. The experimental error in these measurements is 7 %.

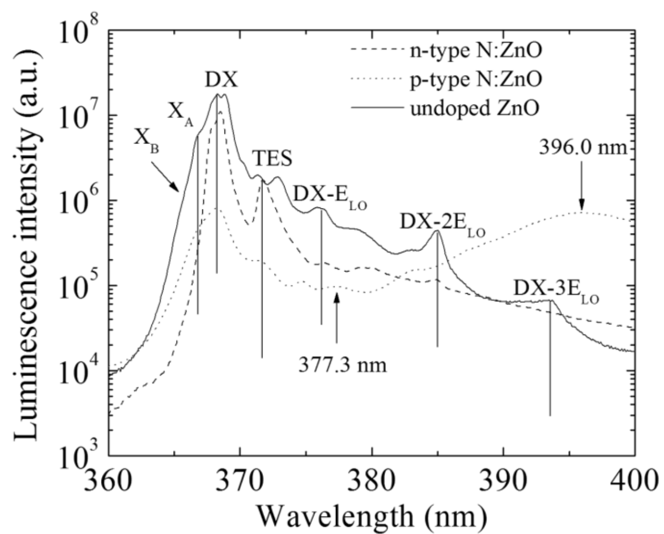

Figure 4.4 Photoluminescence spectra at 6 K of (a) undoped ZnO, (b) *n*-type nitrogen-doped ZnO and (c) *p*-type nitrogen-doped ZnO fabricated at 300°C. Note the DA transitions at 377.3 and 396.0 nm in the *p*-type film.

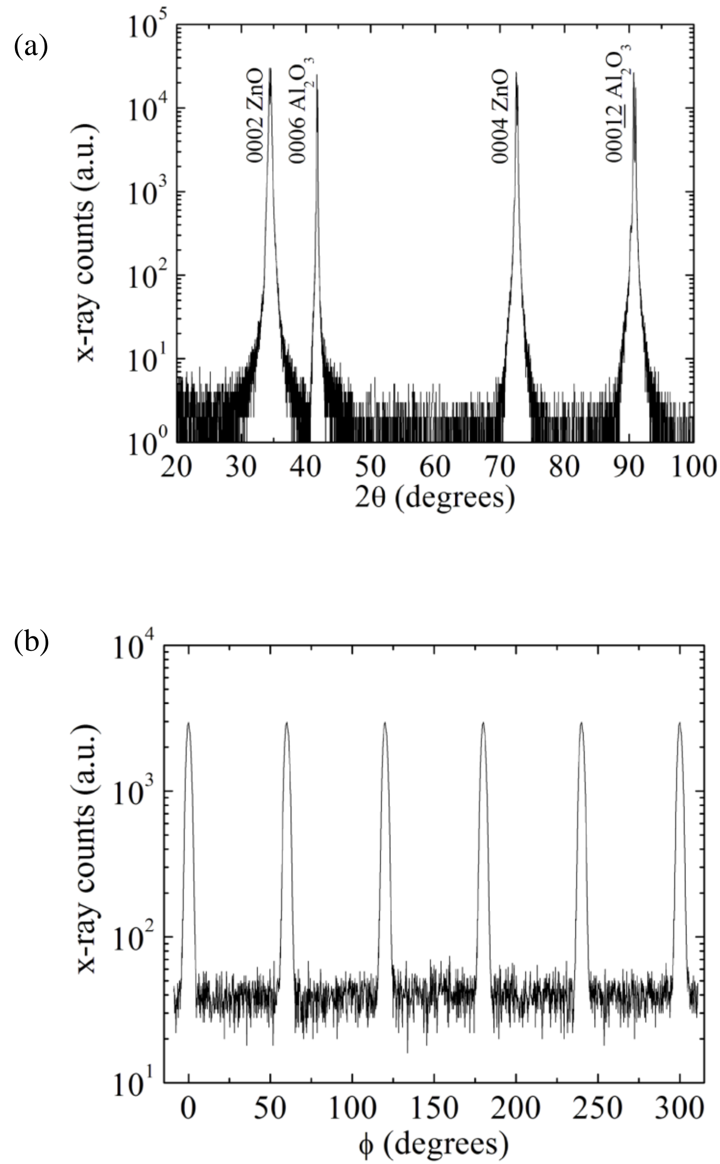

Figure 4.5 (a) Symmetric XRD θ-2θ scan and (b) asymmetric 11-24 ϕ-scan of a nitrogen-doped ZnO sample deposited at 300°C. All nitrogen-doped films grow epitaxially on the (0001) Al_2O_3 substrate in one step, contrary to other processes, which rely on the oxidation of as-deposited Zn_3N_2 films.

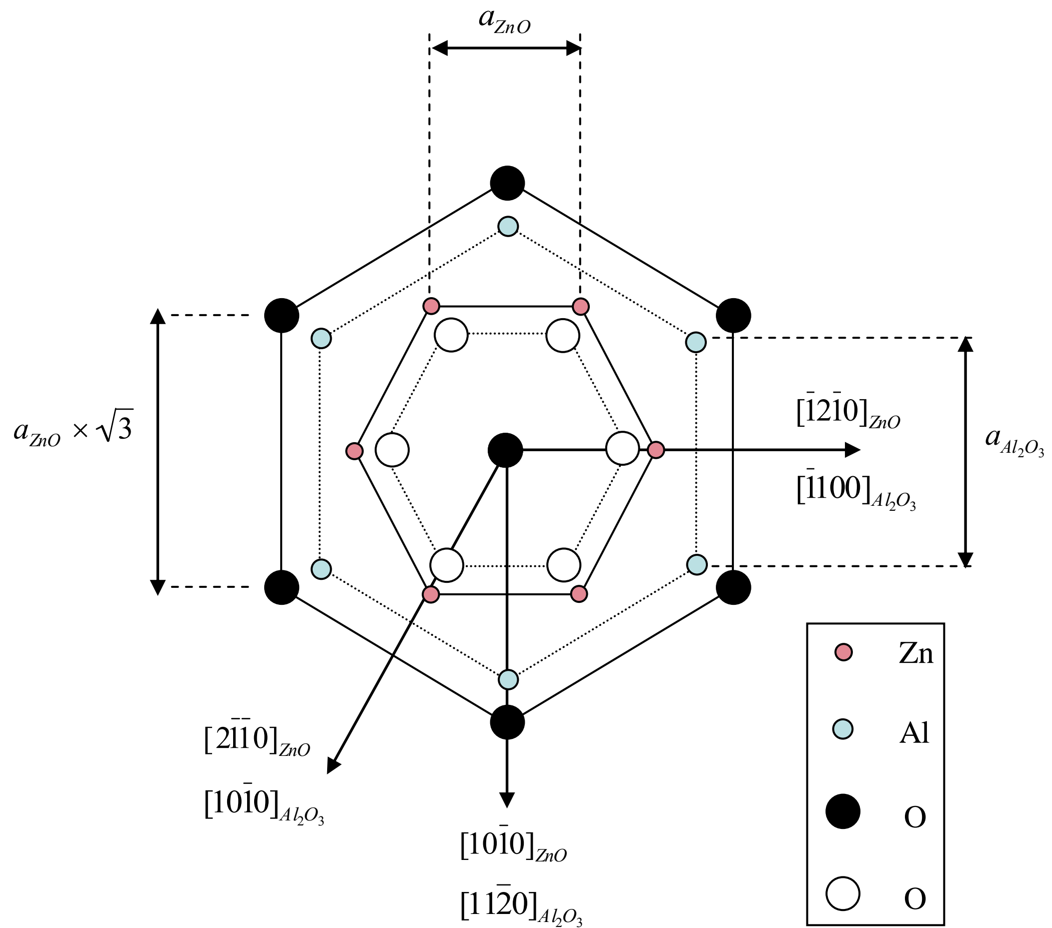

Figure 4.6 Schematic drawing of the epitaxial orientation relationship between ZnO and the (0001) Al_2O_3 substrate.

(a)

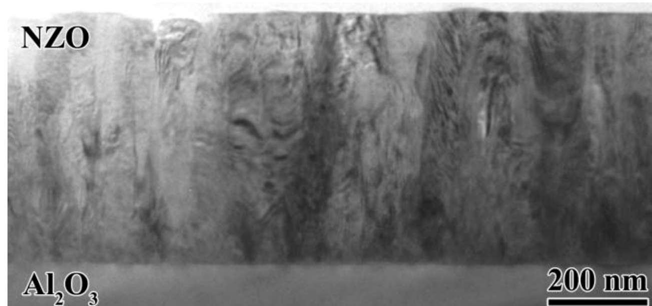

(b)

Figure 4.7 Bright-field low-magnification TEM images of (a) *p*-type nitrogen-doped ZnO fabricated at 300°C and (b) *n*-type nitrogen-doped ZnO fabricated at 400°C. Note the columnar grain microstructure of the *p*-type sample.

Chapter 5

Microstructures and Optoelectronic Properties of Phosphorus-Doped ZnO Films

5.1 Introduction

First-principles predict that in ZnO doped with As or Sb under oxygen-rich growth conditions, a complex between a group-V antisite and two zinc vacancies may have a low formation energy and introduce a 150-160 meV shallow acceptor level.[33] Lee *et al.* used the same concept to model the effect of phosphorus in ZnO.[91] The calculations predict that doping ZnO with phosphorus under oxygen-rich conditions may induce two acceptors: the zinc vacancy (V_{Zn}) and the P_{Zn}-$2V_{Zn}$ complex. The formation and ionization energies of these two acceptors depend on the chemical potential of oxygen and phosphorus during growth, the latter depending on the choice of the dopant source (P_2O_5 or Zn_3P_2). The conclusion of these theoretical studies is that large-size group-V dopants are amphoteric; they act as a donor when forming an isolated antisite, but as an acceptor when the antisite complexes with two zinc vacancies.

Experimentally, phosphorus doping has been investigated widely due to the availability of phosphorus oxide (P_2O_5) and zinc phosphide (Zn_3P_2) powders, which are used to prepare phosphorus-doped ZnO sputtering targets, or directly as dopant sources in vapor phase epitaxy. Phosphorus-doped ZnO (PZO) films have been fabricated by various methods, including pulsed laser deposition (PLD),[185,186] sputtering,[86] organo-metallic vapor phase epitaxy[187] (OMVPE) and molecular beam epitaxy.[87] Heo *et al.* achieved *p*-type conduction in phosphorus-doped ZnO films fabricated under 100-150 mtorr O_2 only when a dilute concentration of Mg was added to enlarge the band gap and increase the formation energy of donors.[85] Hwang *et al.* observed *p*-type behavior in heavily doped films deposited by sputtering and rapidly annealed in a mixture of Ar/N_2 at

elevated temperatures.[188] The level of hole conduction they achieved is the highest ever reported so far with p~10^{17}-10^{19} cm^{-3}, ρ~0.6-4.4 Ω·cm and μ=0.5-3.5 $cm^2/V\cdot s$. More recently, Xiu *et al.* reported the growth by molecular beam epitaxy of textured *p*-type films of relatively high hole concentrations ($p=6\times10^{18}$ cm^{-3}) and insisted on the inevitable competition between donors and acceptors in P-doped ZnO depending on the growth temperature.[189] Though it would appear that a great many synthesis routes leading to *p*-type conduction in P-doped ZnO exist, most of them suffer from reproducibility issues. Furthermore, there exists no report of the effect of phosphorus on the microstructure of ZnO.

The greatest challenge towards *p*-type conductivity in ZnO lies in understanding its intrinsic and doping-induced defects. For example, the pinning effect of the dopant on dislocation slip and electrical passivation by gettering can strongly affect the conductivity type of ZnO films.[190,191] Furthermore, depending on the process, *p*-type conductivity in phosphorus-doped ZnO films may require an annealing treatment. The exact role of post-growth annealing and the concept of acceptor activation are unclear in ZnO. In Mg-doped GaN grown by OMVPE, a post-deposition anneal is required to eliminate hydrogen, which is known to passivate the Mg acceptor. However, the reason for annealing ZnO layers grown by sputtering, pulsed laser deposition or molecular beam epitaxy and the annealing effect on their microstructures are unclear.

In this chapter, the microstructures of phosphorus-doped ZnO films grown heteroepitaxially on (0001) sapphire substrates and homoepitaxially on (0001) ZnO substrates are characterized. The role of defects on the epilayer electrical properties and photoluminescence is addressed. The third section focuses on a more general effort to improve the photoluminescence of P-doped ZnO by relying on oxygen plasma-assisted growth. It will be seen that the dominant acceptor in phosphorus-doped ZnO and thus the epilayer conductivity type depend on the oxygen chemical potential during growth.

5.2 Heteroepitaxial growth of P-doped ZnO on (0001) Al_2O_3

5.2.1 Introduction

In this section, the microscopic defects in heteroepitaxial ZnO films doped with phosphorus are studied, and the growth temperatures (T_G) and annealing temperatures

(T_A) at which stable p-type conductivity can be obtained are determined. The dependence of the conductivity type on T_G is a parameter that first-principles calculations, performed at 0 K, can not take into account, hence the need for systematic studies. 500 nm-thick P-doped ZnO films were deposited on (0001) sapphire at temperatures between 400 °C and 800 °C. The O_2 pressure was fixed to 2.7×10^{-2} mbar. The P_2O_5 amount in the ZnO target was fixed to 1 wt. %, corresponding to a P concentration of 1.2 at. %. The best experimental condition for p-type ZnO was determined to be T_G=600 °C, followed by annealing at T_A=600 °C in 1 atm. O_2 gas, and a P_2O_5 doping amount of 1 wt. %. The onset of good p-type conductivity is always accompanied by a considerable increase in the density of dislocations, as showed by transmission electron microscopy (TEM). Secondary ion mass spectroscopy (SIMS) shows a significant increase in phosphorus solubility. These results suggest that T_G and T_A control the density of dislocations, which in turn controls the phosphorus solubility. Furthermore, as gettering centers for zinc interstitials, the dislocations facilitate the formation of zinc vacancies that can stabilize the P_{Zn}-$2V_{Zn}$ acceptors. Electrical and photoluminescence (PL) measurements show the existence of a 135±15 meV deep acceptor level, in good agreement with theory.[33]

5.2.2 Effect of phosphorus on the optoelectronic properties of ZnO

The room temperature electrical properties of different ZnO films are shown in Fig. 5.1(a)-(c) and summarized in Table 5.1. For films as-deposited at 600 °C, the Hall mobility monotonically decreases with an increase in the phosphorus concentration $[P]$. The carrier concentration and conductivity increase as $[P]$ increases, showing that phosphorus induces donors in ZnO, either via the formation of P_{Zn} antisites[92] or via the generation of native donor defects. The Hall mobility of films deposited at 800 °C is relatively independent of the phosphorus concentration while that of films deposited at 600 °C drops when $[P]$ increases.

All as-deposited PZO films show n-type conductivity and are more conductive than the corresponding undoped films. Although the PZO films as-deposited at 600 °C using a 1 wt. % P_2O_5-doped target are n-type, they become p-type after thermal annealing in O_2 at 600 °C. Results of field-dependent Hall-effect measurements at room

temperature are shown in Fig. 5.1(d) and confirm the positive slope in the Hall coefficient. The electrical properties of the *p*-type samples are ρ=4.9×10^1 Ω·cm, μ=1 cm^2/V·s and p=1.3×10^{17} cm^{-3}.

Results of low-temperature Hall measurements of undoped ZnO, *n*-type PZO deposited at 800 °C and *p*-type PZO deposited at 600 °C are shown in Fig. 5.2. The slowly increasing mobility with measurement temperature of *p*-type PZO shows that impurity and dislocation scattering are the dominant scattering mechanisms. Note that these scattering mechanisms are consistent with the high density of crystal defects induced by heavy phosphorus doping (see section 5.2.4). For the PZO sample deposited at 800 °C, the mobility exhibits two regimes and peaks at ~100 K.

The temperature dependence of the carrier concentration of the *p*-type sample was fitted using the charge balance equation assuming a single donor-single acceptor model. For a *p*-type sample, assuming $p(T) >> n(T)$:[169]

$$p(T) + N_D = \frac{N_A}{1 + \frac{p(T)}{\phi(T)}} \tag{5.1}$$

where N_D is the residual donor level density, N_A is the acceptor concentration and under the assumption that the donor activation energy is temperature independent:

$$\phi(T) = \frac{g_1^p}{g_0^p} N_v^{'} T^{\frac{3}{2}} \exp(-\frac{E_A}{kT}) \tag{5.2}$$

$$N_v^{'} = 2\frac{(2\pi m_h^* k)^{\frac{3}{2}}}{h^3} \tag{5.3}$$

where E_A is the acceptor activation energy. Equation (5.1) can be solved for p:

$$p = \frac{(\phi + N_D)}{2}\left[\left(1 + \frac{4\phi(N_A - N_D)}{(\phi + N_D)^2})^{\frac{1}{2}}\right) - 1\right] \tag{5.4}$$

Under the assumption that $\phi << N_A$, a plot of $\ln(p(T)/T^{3/2})$ as a function of $1/kT$ yields a straight line with a slope equal to E_A. Figure 5.2(d) shows the corresponding fit, which gives an activation energy E_A~120±5 meV.

For the *n*-type PZO sample, the charge balance equation was fitted using Eq. (4.1), (4.2) and (4.3) and assuming a two donor-one acceptor model. The simulation gave

E_{D_1}=23 meV, N_{D_1}=5.7×10^{18} cm^{-3}, E_{D_2}=3 meV, N_{D_1}=2.0×10^{18} cm^{-3} and N_A=1.0×10^{16} cm^{-3}. The physical meaning of D_2 is uncertain at this point, yet the two band model is necessary to maximize the accuracy of the fit.

Figure 5.3 is a typical transmittance spectrum of a 2 μm-thick PZO film deposited at 600 °C. All phosphorus-doped ZnO films are 80 % transparent or more in the visible range. No obvious dependence of the absorption edge (381±3 nm) on the phosphorus concentration was observed.

Figure 5.4(a) shows the PL spectra at 6 K of several ZnO films. The PL spectrum of undoped ZnO [spectrum (i)] was studied in details in section 4.3. The PL spectrum of *n*-type PZO grown at 800 °C [spectrum (ii)] is characterized by broader transitions. The evolution of the energy position of the dominant recombination line in *n*-type PZO was fitted using Eq. (3.19) between 6 K and 160 K. The fit gave $E(0)$=3.369±0.002 eV, α=5.3×10^{-4} eV.K^{-1} and β=350 K. The thermal decay of the integrated intensity of this bound exciton was fitted to Eq. (4.5). The fit gave an exciton binding energy of 5.7 meV and an activation energy of 35 meV, in relatively good agreement with the energy derived from the fit to the CBE. This activation energy could be that of the P_{Zn} antisite, which forms a shallow donor according to first-principles calculations.[77] More work is needed to confirm this assumption.

In contrast, PZO samples grown at 600 °C [spectrum (iii)] show a significantly quenched and broadened near-band-edge (NBE) luminescence due to the high density of non-radiative recombination centers induced by phosphorus doping. In addition, the luminescence is redshifted from 368.2/368.9 nm (3.3673 eV/3.3609 eV) to about 369.5 nm (3.3555 eV) due to the internal deformation potentials induced by phosphorus. After annealing, the shoulder observed in as-deposited samples near 371.5 nm (3.3374 eV) becomes dominant in *p*-type PZO [spectrum (iv)].

Several interpretations of the nature of the 371.5 nm transition can be given: it may be the optical signature of an acceptor-bound exciton, which would be consistent with the electrical properties. Yet, such argument calls for magnetic-field dependent spectroscopy and measurements of the Zeeman splitting. The line could be a two-electron satellite of a donor-bound exciton with a pronounced strain effect in the film. Yet, the

absence of a donor ground state in the spectrum rules this possibility out. Thirdly, it may be an overlap of various transitions as a result of the high defect density in the PZO film.

If the 371.5 nm transition corresponds to an acceptor-bound exciton, the exciton binding energy cannot be calculated from Eq. (3.10) because of the deformation potentials induced by phosphorus. The temperature dependence of the energy position of the transition was found to follow Eq. (3.19) with $E(0)$=3.346±0.002 eV, α=6×10^{-4} eV.K^{-1}, and β=300 K. Yet, it did not follow that of the donor-bound exciton in the as-grown *n*-type PZO sample, thus excluding the possibility that the 371.5 nm line is a two-electron transition of the shallow donor. The temperature dependence of the integrated intensity of the 371.5 nm line shown in Fig. 5.3(b) was fitted to Eq. (4.5).

The localization energy E_{loc} of the acceptor corresponds to the activation energy driving the quenching of the line at low temperature. From the fitting of the data measured between 20 K and 80 K, E_{loc}=15.0 ± 2.0 meV was obtained, a value that is close to the localization energy of the I_6 transition commonly assigned to Al.[70] Depending on the nature of the transition (donor-bound exciton or acceptor-bound exciton), the application of Haynes rule[150] gives different defect activation energies. Under the assumption that the transition is of the acceptor-bound exciton type, an activation energy of 150 meV would be derived, in good agreement with our electrical measurements and first-principles calculations for the acceptor complex;[33] yet it should be taken with caution in the light of the numerous assumptions required to derive this result.

Of interest is the existence at 656 nm (1.89 eV) of a broad (FWHM=150 nm) and unstructured red band in as-deposited and *p*-type PZO films fabricated at 600 °C. Since undoped samples fabricated under the same conditions do not exhibit any red luminescence, it is natural to assign this deep level emission to a phosphorus-induced deep gap state. This result agrees with earlier work published by Heo *et al.*[192] However, the red band was not observed in PZO samples deposited above 700 °C. The microscopic origin of this deep level may therefore be related to a transition between the P_{Zn}-$2V_{Zn}$ complex and an intrinsic deep donor level in ZnO such as the oxygen vacancy.

In conclusion, while heavy doping with phosphorus is required to achieve *p*-type conductivity with p~10^{17} cm^{-3}, the visible luminescence is significantly quenched. This issue will be addressed in section 5.4.

5.2.3 Temperature dependence of the phosphorus solubility

In pulsed laser deposition, the transfer of stoichiometry from the target to the substrate depends on various parameters such as the growth temperature, the oxygen backfill pressure or the target uniformity. In this work, the oxygen pressure is fixed (2.7×10^{-2} mbar) and compositional non-homogeneities in the target are ignored.

The phosphorus depth-profiles in PZO deposited at 600 °C and 800 °C were measured by SIMS. A phosphorus-implanted ZnO sample was used as the reference. Figure 5.5 shows the SIMS measurements of P in films grown at 600 °C and 800 °C. P distributes uniformly ($[P]$ = 3.5×10^{20} cm^{-3}) in films grown at 600 °C. A 3.5×10^{20} cm^{-3} phosphorus concentration in ZnO translates into $\frac{[P]M}{\rho N_A}$=0.8 at. % P in ZnO. Compared with the nominal doping of the target (1 wt. % P_2O_5 in ZnO translates into 1.2 at. % P in ZnO), this concentration corresponds to a transfer of about 71 % of P. On the other hand, $[P]$ decreases rapidly when T_G increases. In particular, at T_G= 800 °C, there is a significant segregation of phosphorus to the film surface, where $[P]$ is as high as 2×10^{21} cm^{-3}, and to the interface with the sapphire substrate, where $[P]$ is 2×10^{20} cm^{-3}. The concentration in the interior of the film is about 6×10^{19} cm^{-3}, so that $n/[P]\approx5\times10^{-2}$, which is smaller than $\exp(-E_D/kT)$=2.5×10^{-1} using E_D=35 meV. The smaller than expected ionization ratios (*i.e.* $n/[P]$ and $p/[P]$ in *n*- and *p*-type samples, respectively) suggest heavy compensation of the free carriers.

5.2.4 Effect of phosphorus on the crystallinity and microstructure of ZnO

The crystallinity of the PZO films was characterized by X-ray diffraction (XRD) and TEM. No impurity phases were found in any of the PZO/Al_2O_3 films as shown by the representative θ-2θ scan in Fig. 5.6(a). All films studied in this work were grown epitaxially on Al_2O_3without rotational domains, as shown by the ϕ-scan of the ZnO $11\bar{2}4$ reflection in Fig. 5.6(b). The in-plane and out-of-plane crystallinities were evaluated by ω-scans of the 0002 and $10\bar{1}2$ reflections. It can be seen from Fig. 5.6(c) and 5.6(d) that PZO films grown at 600 °C have significantly broader rocking curves than films grown at 800 °C.

To understand the origin of the broadening, the tilt angles were determined by a Hall-Williamson analysis[137] and the twist angles were determined by ω-scans of off-axis planes in the skew symmetric diffraction geometry. Under the assumption of random dislocation arrangement, the tilt and twist angles can be used to calculate the dislocation densities. The density of dislocations with a Burgers vector's component parallel to the c-axis ($\rho_{//c}$) is proportional to the square of the tilt angle while the density of dislocations with a Burgers vector's component perpendicular to the c-axis ($\rho_{\perp c}$) is proportional to the square of the twist. The following formula was used:[193]

$$\rho = \frac{\beta^2}{4.35 b^2} \tag{5.5}$$

where b is the magnitude of the Burgers vector of the dislocation, β is the mosaic angle and ρ is the dislocation density. Table 5.2 summarizes the average mosaic angles and threading dislocation densities. The significant increase of both tilt and twist angles with $[P]$ indicates the degradation of the film crystallinity. In addition, these observations are consistent with the temperature dependence of the hole mobility in PZO since the effect of dislocation scattering can no longer be ignored in the layers grown at 600 °C.

The vertical line defects in Fig. 5.7(a) and 5.7(b) are dislocations that originate from the film/substrate interface due to the large lattice mismatch between ZnO and Al_2O_3, and thread to the film surface. Numerous interactions between dislocations happen within the first 500 nm. These interactions result in defect reduction via half-loop formation. By studying several cross-sectional TEM images and using the $\vec{\boldsymbol{g}} \cdot \vec{\boldsymbol{b}}$ extinction criterion in diffraction contrast, we estimated that most dislocations were either edge or mixed-type. This observation is consistent with simple energy considerations since the dislocation nucleation energy of screw dislocations in ZnO is 1.3 times larger than that of edge dislocations. It is worth noting that the TEM images of the undoped ZnO films grown at 600 °C [Fig. 5.7(a)] and PZO films grown at 800 °C [Fig. 5.7(b)] show similar densities of dislocations. Figure 5.7(c) shows the microstructure of a p-type PZO film at 600 °C. It is evident from Fig. 5.7(c) that there exists a high density of threading dislocations throughout the film. Besides the lattice mismatch, the pinning effect of phosphorus on the dislocation motion during growth could also contribute to the

dislocation density, as we found that $[P]$, $\rho_{//c}$ and $\rho_{\perp c}$ are directly related. These observations are consistent with the XRD results shown in Table 5.3.

Figure 5.8(a) is a high-resolution TEM (HRTEM) image showing the atomic structure of the interface between the PZO film grown at 600 °C and the sapphire substrate. All studied films formed atomically sharp interfaces with Al_2O_3. The most abundant defect in PZO is the interstitial-type dislocation loop, which proceeds by the insertion of half a unit cell in the basal plane. The dislocation loop segments are 10-15 nm on average. Several loops can be seen in Fig. 5.8(b). Figure 5.8(c) shows the atomic arrangement around a single interstitial dislocation, which can be simulated using a ball and stick model as shown in Fig. 5.8(d). This defect results in a distortion of the lattice with a local zincblende stacking of the basal planes around the loop. The relationship between dislocation loops and stacking faults is not trivial; however it appears that dislocation loops existing in undoped material contain a stacking fault. The so-formed fault is an extrinsic fault bound with two Frank partial dislocations with a Burgers vector of $1/2<0001>$. This fault can transform into a low-energy intrinsic fault by the nucleation and sweep of a Shockley partial according to the following reaction: $1/3[\bar{1}100]+1/2[0001]\rightarrow 1/6[\bar{2}203]$. The hexagonal basal plane is preferred for the precipitation of interstitials because it is the closest packed plane.

Stacking faults corresponding to disruptions in the -aAbB- stacking sequence along the 0001 direction with a shear of $a/3$ along the $10\bar{1}0$ direction were also observed in phosphorus-doped ZnO.[194] These faults are terminated by one or a pair of dislocations. According to our TEM observations, these have a Burgers vector $\vec{\boldsymbol{b}}=1/6<02\bar{2}\bar{3}>$ and are therefore mixed-type Frank-Shockley partial dislocations.[194] The formation mechanism of such faults in ZnO/Al_2O_3 has been discussed by Gerthsen *et al.*[195] The faults form by condensation or precipitation of native donor defects (oxygen vacancies or zinc interstitials) and their concentration depends on the II-VI ratio during growth. These defects were statistically not the dominant defects in phosphorus-doped ZnO.

5.2.5 Microscopic origin of *p*-type conduction in ZnO

Due to the large size mismatch between P and O atoms, the P dopants, existing as P_{Zn} antisites, bind with two zinc vacancies to form a complex defect P_{Zn}-$2V_{Zn}$ to relieve

the strain energy associated with the P_{Zn} antisites, as predicted by theory.[33] Such complexes are shallow acceptors and ionize holes, resulting in *p*-type conductivity provided the native donor concentration is reduced by post-deposition annealing. Figure 5.9 shows the structure of the P_{Zn}-$2V_{Zn}$ complex in the ZnO lattice. Let us assume that one thousandth of the phosphorus atoms in the film form electrically active antisites, *i.e.* $[P_{Zn}]\sim10^{17}$ at/cm^3. Assuming that the equilibrium concentration of zinc vacancies is $[V_{Zn}]_{eq}\sim10^{17}$ cm^{-3}, and that only one half will participate into energy minimization interactions with phosphorus antisites, the concentration of P_{Zn}-$2V_{Zn}$ complexes should be on the order of 10^{16}-10^{17} cm^{-3}. As the complexes form, the equilibrium concentration of zinc vacancies decreases by 50 %. This decrease is compensated by the injection of zinc vacancies, which increases the net acceptor complex concentration and induces Frenkel pair formation in order to balance the overall charge. The precipitation of excess zinc accounts for the formation of ~10^{12} cm^{-2} interstitial dislocation loops, as observed by TEM. Therefore, it can be concluded that phosphorus complexes induce interstitial dislocation loops and type-I stacking faults, hence the higher density of such defects in P-doped ZnO (~10^{12} cm^{-2}) than in undoped ZnO films (~10^{9} cm^{-2}). In addition, the gettering of shallow residual donors such as zinc interstitials by the fault results in a lower electron concentration and a compensation ratio $N_A / N_D \sim 10-100$ in agreement with the SIMS and electrical results.

For practical optoelectronic applications, the *p*-type layer is usually grown atop a multilayered homojunction structure such as that shown in Fig. 1.1. Thus, two questions are raised: (1) what are the microscopic defects in P-ZnO films grown homoepitaxially on ZnO substrates and what effects do they have on the macroscopic properties? (2) Does the model for *p*-type conduction presented in this section hold?

5.3 Homoepitaxial growth of P-doped ZnO on (0001) ZnO

5.3.1 Introduction

Homoepitaxy has the advantage of reducing the density of crystal defects, offering potentially higher quantum efficiencies in ZnO optical devices. Thus, there is a strong motivation to study and understand the role of crystal defects on the conductivity type of homoepitaxial ZnO layers doped with phosphorus, and generalize the model discussed in Ref. 196.

The homoepitaxial layers studied in this section were deposited at 600 °C on hydrothermally-grown and pressurized-melt grown ZnO substrates by laser ablation of a 1 wt. % P_2O_5-doped ZnO target in 2.7×10^{-2} mbar O_2. The growth rate was 0.5 Å/s.

5.3.2 Results and discussion

Fig. 5.10 shows the phosphorus depth profile measured by secondary-ion mass spectroscopy of a 185 nm-thick homoepitaxial PZO film. It can be seen that phosphorus distributes uniformly with a concentration of 3.8×10^{20} cm^{-3} throughout the film. A similar result (3.5×10^{20} cm^{-3}) was obtained for heteroepitaxial PZO films deposited under the same conditions.[196]

Figure 5.11 shows a 0002 θ-2θ XRD pattern for a homoepitaxial *p*-type PZO film. The *c*-axis of the homoepitaxial film is subject to a compressive strain, consistent with the lattice dilation induced by phosphorus. The full-width at half-maximum (FWHM) value is 90 arcsec in comparison with 33 arcsec for the substrate. The Pendellösung fringes indicate interface coherence and high epilayer crystallinity.[197] The angular difference $\Delta\theta$ between two consecutive fringes is inversely proportional to the epilayer thickness t via:

$$\Delta\theta = \frac{\lambda \sin(\theta \pm \varphi)}{t \sin(2\theta)} \tag{5.6}$$

where λ=1.54 Å is the wavelength of the Cu $K\alpha$ radiation, φ is the angle formed between the asymmetric plane considered and the basal plane of ZnO and the sign depends on the measurement geometry (see section 3.2.1). Eq. (5.6) gives t=193 nm, in excellent agreement with the thickness determined by SIMS and TEM.

The strains in the epilayer were estimated by asymmetric reciprocal space mapping of the $10\bar{1}5$ reflection of ZnO. Using the lattice parameters (c_{ZnO}=5.2069 Å and a_{ZnO}=3.2495 Å) of bulk ZnO as reference, the lattice constants of the homoepitaxial PZO film were determined to be c_{PZO}=5.2232 Å and a_{PZO}=3.2483 Å, corresponding to strains:

$$\varepsilon_c = \frac{c_{\mathrm{PZO}}}{c_{\mathrm{ZnO}}} - 1 = 3.1\times10^{-3} \tag{5.7a}$$

$$\varepsilon_a = \frac{a_{\mathrm{PZO}}}{a_{\mathrm{ZnO}}} - 1 = -3.7\times10^{-4} \tag{5.7b}$$

corresponding to an increase of only 0.35% in the c/a ratio. Note that the deformation induced by phosphorus is mostly concentrated along the growth axis of the epilayer. Table 5.3 compares the FWHMs of the 0002 and $10\bar{1}2$ reflections and the strains ε_c and ε_a. It can be seen that broadening and strains are dramatically reduced by homoepitaxy.

Figure 5.12(a) is a cross-sectional TEM image showing the microstructure of homoepitaxial PZO. No threading dislocations were observed, in contrast with the high density (~1.0×10^{11} cm^{-2}) observed in heteroepitaxial films grown under the same conditions.[196] The primary defects in PZO/ZnO appear to be short dislocation loops in the 0001 plane and their associated partial dislocations, consistent with our TEM observations of heteroepitaxial samples.[196] Figure 5.12(b) is a representative high-resolution TEM micrograph showing the atomic structure of a pair of partial dislocations belonging to a dislocation loop. According to our TEM observations, the density of interstitial-type dislocation loops is higher in phosphorus-doped layers than in undoped layers, most likely for the reason described in section 5.2.5.[198]

Since the (0001) ZnO substrate is semi-insulating with a resistivity of ~10^3 Ω·cm, the electrical properties of homoepitaxial PZO films can be measured. All as-grown homoepitaxial PZO films show n-type conductivity but become p-type after annealing at 600 °C in 1 atm O_2, consistent with what we observed for heteroepitaxial films. Table 5.4 provides a comparison of the electrical properties at room temperature of hetero- and homoepitaxial PZO samples.

Results from variable-temperature Hall-effect measurements of the homoepitaxial films before (n-type) and after annealing (p-type) are shown in Fig. 5.13(a) and 5.13(b). The electron concentration was fitted using the CBE and a two donor-one acceptor

model.[169] The following donor activation energies and concentrations were obtained: E_{D_1}=29 meV, N_{D_1}=5.4×10^{17} cm^{-3}, E_{D_2}=40 meV, and N_{D_2}=3×10^{16} cm^{-3} and the acceptor concentration was N_A=2×10^{16} cm^{-3}. In contrast, no good fit to the CBE could be obtained for the *p*-type homoepitaxial sample possibly because of the uncertainty of the degeneracy of holes.[89] Yet, the plateau in the hole concentration suggests freezing of the free carriers followed by gradual ionization of the neutral acceptor.

While Look *et al.* pointed out that dislocation scattering occurs primarily in epilayers containing >10^8 cm^{-2} edge-type threading dislocations, the partial dislocations with a Burgers vector $\vec{b} = 1/6 < 02\bar{2}3 >$ can also scatter carriers when charged. We included dislocation scattering in Matthiessen's rule to fit the hole mobility in Fig. 5.13(b) and found that a good fit could be obtained only between 180 and 300 K, assuming a dislocation density of ~5×10^{11} cm^{-2} and a residual donor level concentration of 10^{16} cm^{-3}. Since this dislocation density is on the same order as the density of partial dislocations we calculated by TEM, we suggest that the lines of the partial dislocations become charged as the acceptor complex gradually ionizes above 180 K. The Hall mobility in *n*-type homoepitaxial PZO shows a maximum μ_H=590 cm^2/V·s at 60 K and its temperature dependence is almost entirely dominated by piezoelectric scattering. The strength of dislocation scattering is weak possibly because the acceptor complexes are neutral or gettered at the dislocation lines.

Figure 5.14 shows the PL spectra at 12.5 K of the *p*-type homoepitaxial and heteroepitaxial PZO layers. For comparison, the PL spectra of bulk ZnO and of undoped ZnO grown on (0001) sapphire at 600 °C are also shown. Their NBE luminescence is dominated by free and bound-excitons along with their excited states and phonon replicas. The NBE luminescence of both PZO layers is dramatically quenched and broadened due to the high density of non-radiative recombination centers induced by the phosphorus dopant. The NBE luminescence of the homoepitaxial layer features two donor-bound excitons at 368.16 nm and 368.46 nm, and is dominated by a 372.56 nm transition. In a variety of heavily phosphorus-doped *n*-type and *p*-type ZnO samples, dominant transition was observed in a 372.3-373 nm range. These transitions were tentatively assigned to Y-lines. In the case of PZO/ZnO, our TEM studies show that the

dominant defects are the interstitial dislocation loops bound with Frank-Shockley partial dislocations. Thus, the 372.56 nm Y-line in homoepitaxial phosphorus-doped ZnO may correspond to excitons bound to these defects or to point defects trapped in the strain fields of the partial dislocations. Direct correlations between the dislocation loop density and the strength of the Y-line remain to be demonstrated.

In conclusion, while heavy phosphorus doping is necessary to obtain *p*-type conductivity, the epilayer photoluminescence is strongly degraded by the high density of crystal defects. One solution to minimize non-radiative recombination is to lower the phosphorus concentration in the film while ensuring annihilation of native donors, possibly with the help of an O_2 plasma during growth.

5.3.3 Generalization of the model for *p*-type conduction in P-doped ZnO

The onset of *p*-type conductivity in both hetero- and homoepitaxial P-doped ZnO films can be explained by the same model. The electrical measurements conducted on *p*-type PZO/ZnO films show that the dominant acceptor localizes in the lines of the partial dislocations. Thus, it can be concluded that the key defects responsible for the complex acceptor formation (and for the *p*-type conduction in P-doped ZnO) are the partial dislocations associated with the interstitial dislocation loops. They electrically passivate mobile zinc interstitials (donors) by gettering and localize shallow acceptors formed by the reaction between P_{Zn} antisites (which spontaneously form in P-doped ZnO) and Zn vacancies (which are induced by Frenkel pair formation). Note that the role of oxygen annealing is to further minimize the residual electron concentration and favor the acceptor complex formation so that $N_A > N_D$.

5.4 Effect of oxygen plasma on the optoelectronic properties of P-doped ZnO

5.4.1 Introduction

While *p*-type conductivity (p~1-3×10^{17} cm^{-3}) can be observed in P-doped ZnO, the epilayer luminescence yield is strongly degraded by the high density of non-radiative crystal defects induced by heavy doping with phosphorus ($[P]$~10^{20} at/cm^3). Since the internal quantum efficiency of ZnO optical devices is strongly dependent on the luminescence of the epilayers, there is a need to grow *p*-type ZnO materials with good

optical properties. Recently, various groups have investigated the optical properties of P-doped ZnO films, yet little microscopic information on the formation mechanism of the acceptor has emerged. Von Wenckstern *et al.* observed a donor-acceptor (DA) recombination between 3.21 and 3.26 eV in *n*-type films deposited by laser ablation of P_2O_5-doped ZnO targets,[186] while Kwon *et al.* observed DA recombination at 3.24 eV in sputtered *p*-type films.[199]

In an effort to improve the NBE luminescence of P-doped ZnO, light doping of ZnO by P was explored. Since compensation can be an issue in lightly doped films, oxygen plasma-assisted growth was used to maximize the formation energy of hole killers by moving toward more oxygen-rich growth conditions. A violet luminescence band at 3.1099 eV (at 12.5 K) was observed in lightly phosphorus-doped films ($[P]$~1.7×10^{19} at/cm^3) grown with oxygen-plasma. The transition was studied by excitation-intensity and temperature-dependent PL measurements, and assigned to a DA transition. In comparison with results from undoped ZnO films fabricated under the same conditions, we conclude that the acceptor is induced by doping with phosphorus. The acceptor may be the native zinc vacancy. These results bring an experimental proof to the theoretical work by Lee *et al.*[91] Yet, it is unlikely to observe *p*-type conduction in such films because the zinc vacancies are too deep to overcome the electron concentration induced by P_{Zn} donors.

The sample studied in this section was grown the following way: a 50 nm-thick undoped ZnO buffer layer was initially deposited at 350 ºC in 2.7×10^{-4} mbar O_2. A 1 μm-thick phosphorus-doped ZnO epilayer was then deposited at 600 ºC using the conditions described in the experimental section. The phosphorus concentration in the P-doped film was 1.7×10^{19} at/cm^3, according to the SIMS analysis.

5.4.2 Results and discussion

The PL spectra at 12.5 K of undoped and P-doped ZnO films are shown in Fig. 5.15. The electrical properties of the samples are summarized in Table 5.5. The spectrum of undoped ZnO is dominated by three donor-bound exciton (DX) transitions at 368.27 nm (3.3667 eV), 368.74 nm (3.3624 eV) and 369.14 nm (3.3587 eV). The other lines are longitudinal optical (LO) phonon replicas, separated by E_{LO}=72 meV, and excited states

associated with free and bound excitons. In contrast with undoped ZnO, a transition appears at 398.68 nm (3.1099 eV) in the P-doped film. The recombination band has a full-width at half-maximum of 0.04 eV and shows a pronounced phonon coupling with five visible replicas.

To identify the nature of the 3.1099 eV transition, the evolution of its normalized intensity I as a function of the excitation intensity F was studied. The experimental data was fitted to a power law, $I \propto F^{\beta}$, where β is a dimensionless exponent. For free or bound-excitons, $1<\beta<2$, while for free-to-bound and DA transitions, $\beta\leq 1$.[163] As seen in Fig. 5.16(a), a good fit to the data was obtained with β=0.65, thus eliminating bound-exciton complexes. Excitation intensity-dependent PL measurements were also conducted. It was found that the energy position of the band at 12.5 K depended on the excitation intensity as shown in Fig. 5.16(b). The transition energy is blue-shifted by 14.3 meV when F increases from 10^{-3} W/cm^2 to 5×10^{-1} W/cm^2. As discussed in section 3.6.2.4, a blueshift under increasing excitation intensity is characteristic of DA transitions.[149] Thus, the 3.1099 eV band was attributed to a DA transition.

The effect of the phosphorus concentration $[P]$ on the DA transition is summarized in Table 5.6. We found that the transition energy redshifted when $[P]$ increased, possibly because of increasing potential fluctuations and decreasing Coulomb energy. The blueshift ΔE followed a power law $\Delta E \propto [P]^{\alpha}$ where α=0.346, as determined by a least-squares fit to the data shown in Fig. 5.16(c). This observation is in good agreement with Eq. (3.16) combined with Eq. (3.17). Indeed, α=0.346 agrees with the fact that E_{DAP} scales linearly with $[P]^{1/3}$.

Figure 5.17 is a semi-log plot of the PL intensity of the DA transition as a function of inverse thermal energy. It shows that the intensity gradually decreases as the thermal energy increases. The DA transition quenches at T > 160 K and its integrated intensity was fitted to a two-step Arrhenius law using Eq. (3.22). We found C_1=1.7×10^3, C_2=7.6×10^1, E_1=42.2±0.8 meV, and E_2=6.9±0.6 meV. The quenching was therefore attributed to the thermalization of electrons bound to a donor of activation energy E_1=42.2 meV. Note that E_2 could correspond to the donor localization energy.

Since no free electron-to-conduction band transition was observed on the high-energy side of the DA band at elevated temperatures, the acceptor energy had to be estimated. Assuming infinite pair separation, the contribution of the Coulomb energy in Eq. (3.16) can be ignored. The band gap energy can be estimated using Eq. (3.19). At 12.5 K, E_G=3.4369 eV. Taking E_D=42.2 meV and $E_{DAP}(\infty)$=3.0585 eV, we find E_A=336±10 meV using Eq. (3.16).

Another approach is to use the fact that the Bohr radius of the carrier bound to a neutral defect is correlated to the free carrier-phonon coupling.[200] The Huang-Rhys factor S,[149] which characterizes the coupling strength, is determined from a Poisson distribution, as discussed in section 3.6.2.3. Using Eq. (3.14), we found S=0.29, showing a weak coupling, yet in agreement with other reports of DA transitions in ZnO.[155,181] S=0.29 corresponds to a pair separation r=3 nm, according to the model described in Ref. 200. Using Eq. (3.16), we determined a Coulomb energy of 55 meV and an activation energy E_A=339±5 meV, in excellent agreement with our previous calculation.

To further understand the acceptor characteristic, we studied the thermal stability of the DA transition by annealing at different temperatures (T_A) the P-ZnO film in O_2 for one hour. Figure 5.18 shows the effect of the annealing temperature T_A on the luminescence of phosphorus-doped ZnO. It can be seen that the violet band begins to quench at T_A=700 ºC and vanishes completely at T_A=900 ºC, suggesting that one of the gap states involved in the DA transition has been entirely annealed out or has decomposed. In parallel, the resistivity and electron concentration of the films change only slightly with annealing, from $\rho=5.9\times10^{-2}$ $\Omega\cdot$cm and $n=1.9\times10^{18}$ cm^{-3} in the as-grown P-doped film, to $\rho=9.2\times10^{-2}$ $\Omega\cdot$cm and $n=1.1\times10^{18}$ cm^{-3} in the film annealed at 900 ºC. This is consistent with the fact that the acceptor forms a deep level that cannot compensate the electrons ionized by P_{Zn} donors. Note that the increase in the green band intensity after a 900 ºC anneal in O_2 was also observed in undoped ZnO, suggesting that the enhancement of the defect-related emission is a phenomenon intrinsic to ZnO, and not induced by P-doping.

The acceptor introduced in lightly P-doped ZnO grown under O-rich conditions (created by the oxygen plasma) may be the zinc vacancy rather than the P_{Zn}-$2V_{Zn}$

complex. Depending on the charge states considered, various transition energies have been predicted for the zinc vacancy: 0.39 eV,[33] 0.27 eV,[91] 0.34 eV[60] and 0.3 eV,[201] in good agreement with the above calculations. Despite the spontaneous formation of P_{Zn} antisites (responsible for the *n*-type conduction in the as-grown films) and the injection of zinc vacancies by crystal defects, the shallow P_{Zn}-$2V_{Zn}$ complex may not form after annealing because there are no energy-minimization interactions between the V_{Zn} and P_{Zn} defects under O-rich growth conditions, in agreement with first-principles calculations.[91] Note that the quenching of the DA transition with annealing can be explained by the self-diffusion of zinc vacancies under oxygen-rich conditions leading to defect annealing.[202]

5.5 Conclusions

The conductivity type in P-doped ZnO is determined by the interactions between native point defects and doping-induced crystal defects. The role of dislocations on the formation of shallow acceptor complexes was elucidated. Heavy and uniform doping ($[P]=3.5\times10^{20}$ at/cm^3) is necessary to compensate the residual electron concentration in the films and obtain *p*-type conductivity. As a result, the NBE photoluminescence is substantially quenched because the crystal defects, mainly interstitial dislocation loops, are non-radiative recombination centers. The use of an O_2 plasma during growth results in a stronger NBE photoluminescence and introduces a violet band, which was assigned to a DA transition. Based on its activation energy, it is possible that the acceptor involved in this transition is the zinc vacancy. This illustrates one aspect of the doping limit rule, which is to induce the formation of native acceptor defects that will counteract the donor defects spontaneously formed by phosphorus. These results also bring an experimental proof to the predictions by Lee *et al.* and show that in P_2O_5-doped ZnO, moving towards oxygen-rich conditions may not lead to *p*-type conductivity because of the difficulty to ionize the dominant acceptor at room temperature.

Table 5.1 Room-temperature electrical properties of undoped and P-doped ZnO films before and after annealing at 600 °C. Each sample is 0.5 μm-thick.

Sample	T_G (℃)	*Carrier type*	*Resistivity* ($\Omega\cdot cm$)	*Carrier density* (cm^{-3})	*Hall mobility* ($cm^2/V\cdot s$)
ZnO as-grown	600	*n*	47	1.7	7.9×10^{16}
ZnO annealed	600	*n*	14	1.8×10^{2}	2.4×10^{15}
ZnO as-grown	800	*n*	117	6.6×10^{-2}	8.2×10^{17}
ZnO annealed	800	*n*	121	7.1×10^{-2}	7.3×10^{17}
PZO as-grown	600	*n*	11	1.5×10^{-1}	3.8×10^{18}
PZO annealed	600	*p*	1	4.9×10^{1}	1.3×10^{17}
PZO as-grown	800	*n*	51	3.6×10^{-2}	3.4×10^{18}
PZO annealed	800	*n*	47	5.1×10^{-2}	2.6×10^{18}

Table 5.2 Tilt angle, twist angle, and densities of threading dislocations in undoped ZnO, *n*-type PZO, and *p*-type PZO.

Sample	T_G (℃)	*Tilt* (*arcmin*)	*Twist* (*arcmin*)	$\rho_{//c}$ (cm^{-2})	$\rho_{\perp c}$ (cm^{-2})
n-type PZO	800	10.4	16.2	7.2×10^{8}	4.2×10^{9}
undoped ZnO	800	4.2	5.4	1.2×10^{8}	4.7×10^{8}
p-type PZO	600	39.6	84	1×10^{10}	1.1×10^{11}
undoped ZnO	600	13.2	14.1	1.2×10^{9}	3.2×10^{9}

Table 5.3 Comparison of X-ray diffraction rocking curve half-widths and biaxial strains in p-type heteroepitaxial and homoepitaxial films.

p-type PZO sample	*ω-FWHM (°) (002)*	*ω-FWHM (°) (102)*	ε_c ($\times 10^{-4}$)	ε_a ($\times 10^{-4}$)
heteroepitaxial	0.83	1.44	127	-119
homoepitaxial	0.025	0.067	3.95	3.83

Table 5.4 Electrical properties at room temperature of *n*-type and *p*-type heteroepitaxial and homoepitaxial PZO films.

PZO sample	*Resistivity* ($\Omega \cdot cm$)	*Carrier density* (cm^{-3})	*Hall mobility* ($cm^2/V \cdot s$)
n-type heteroepitaxial	1.5×10^{-1}	3.8×10^{18}	11
n-type homoepitaxial	1.4×10^{-1}	3.5×10^{17}	123
p-type heteroepitaxial	4.9×10^{1}	1.3×10^{17}	1
p-type homoepitaxial	4.1	1.9×10^{17}	8

Table 5.5 Electrical properties at room temperature of undoped ZnO and P-doped ZnO films grown by oxygen plasma-assisted PLD. The film thickness is ~1 μm and the anneal temperature was 900 °C.

Sample	*Resistivity* $(\Omega\cdot cm)$	*Carrier density* (cm^{-3})	*Hall mobility* $(cm^2/V\cdot s)$
Undoped ZnO	2.4	6.0×10^{16}	45
P-doped ZnO	5.9×10^{-2}	1.9×10^{18}	58
P-doped ZnO annealed	9.2×10^{-2}	1.1×10^{18}	62

Table 5.6 Effect of the phosphorus concentration on the energy position, energy shift, intensity of the DA transition and on the activation energy of the acceptor.

$[P]$ at/cm^3	E_{DAP} (eV)	$E_{DAP}(\infty)$ (eV)	ΔE (meV)	I_{DAP}/I_{DX}	E_A (meV)
1.7×10^{19}	3.1099	3.0585	14.3	0.06	336±5
3.5×10^{19}	3.1051	3.038	23.8	0.13	357±8
1.7×10^{20}	3.0841	3.0073	35.4	12.8	387±23
3.5×10^{20}	3.041	2.9903	44	13.4	404±25

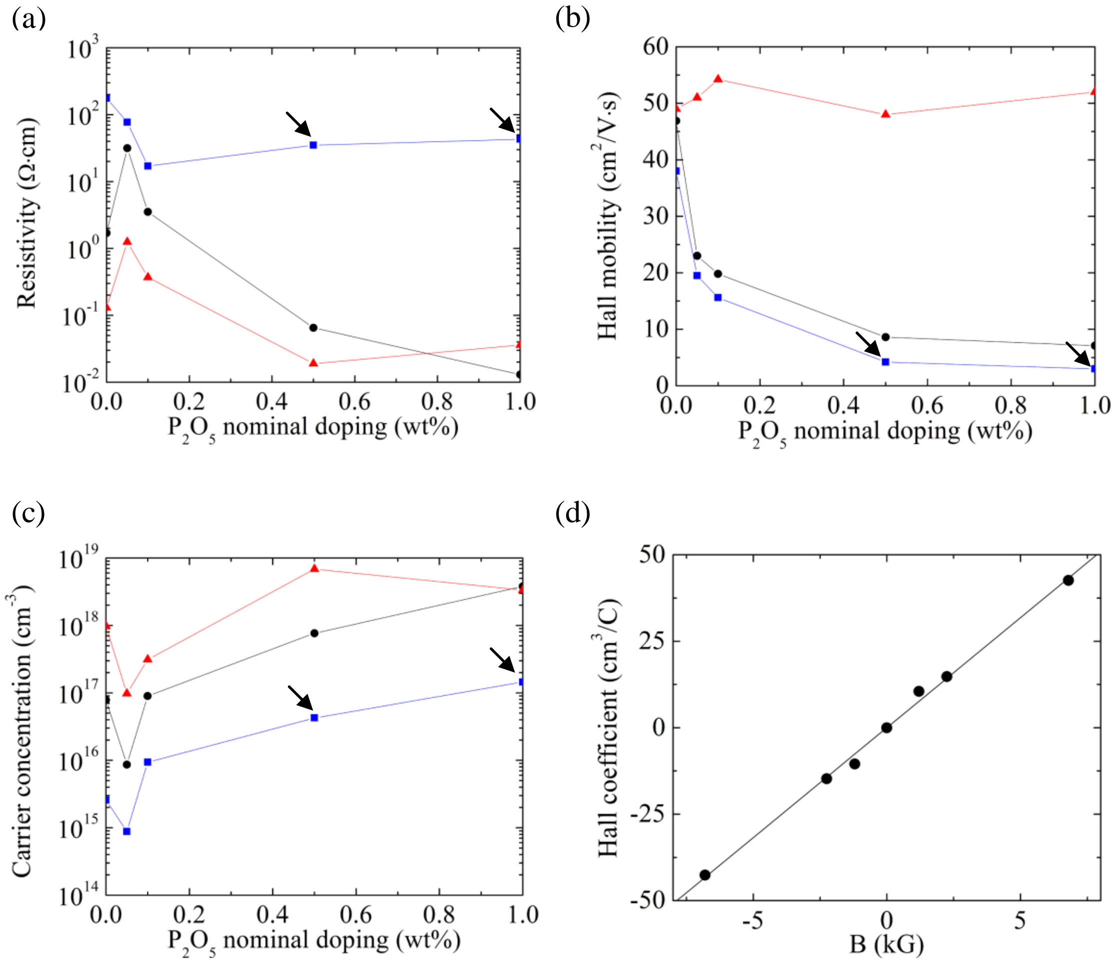

Figure 5.1 (a) Resistivity, (b) Hall mobility and (c) carrier concentration at room temperature of various ZnO films as a function of the phosphorus concentration in the P_2O_5-doped ZnO sputtering target. The triangles correspond to T_G=800°C, the circles to T_G=600°C and the squares to T_G=600°C, followed by annealing at T_A=600°C. The arrows point to the *p*-type samples. (d) Field-dependent measurement of the Hall coefficient in *p*-type PZO deposited at T_G=600°C and annealed at T_A=600°C.

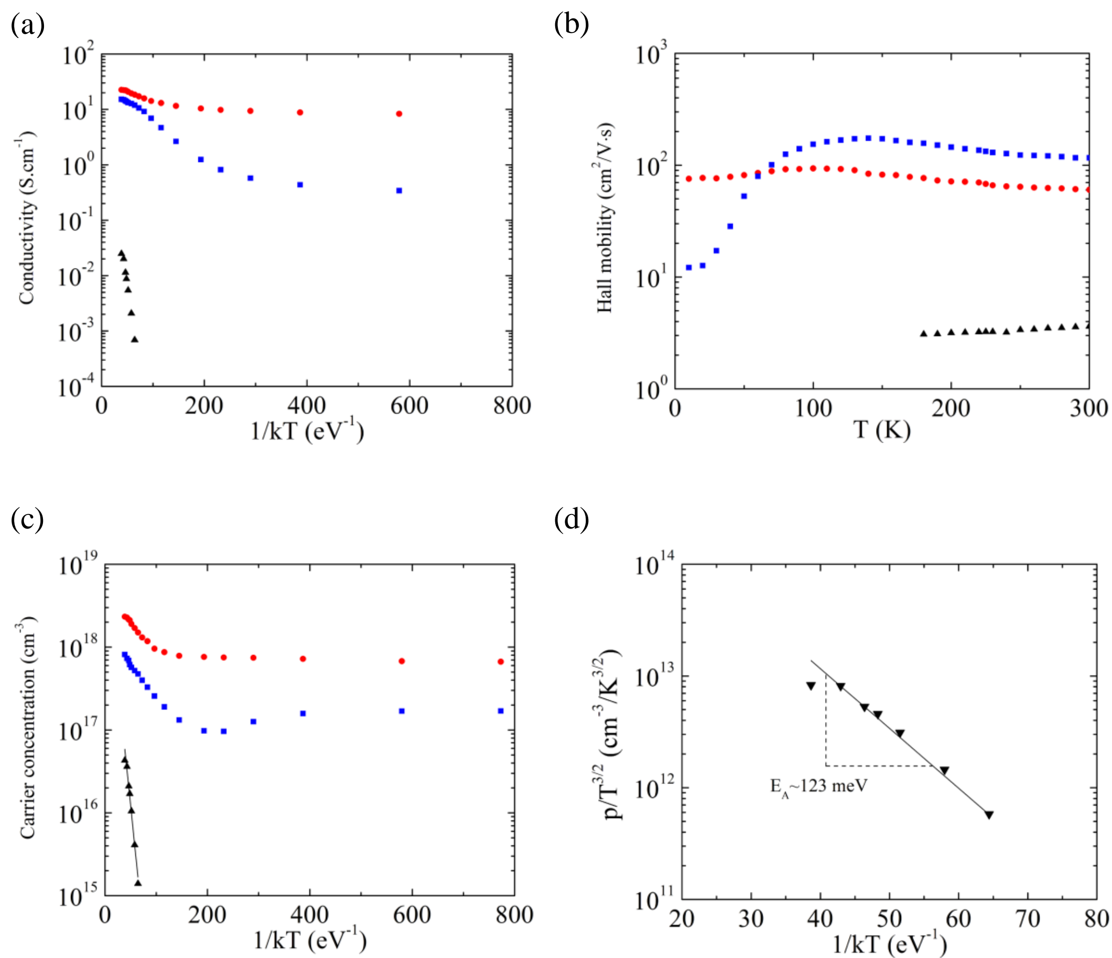

Figure 5.2 Temperature dependences of the (a) conductivity, (b) Hall-mobility and (c) carrier concentration of different ZnO films. The triangles, circles and squares correspond to *p*-type PZO, *n*-type PZO and undoped ZnO respectively. (d) Fit to the charge balance equation for a *p*-type PZO heteroepitaxial film giving an acceptor activation energy of 120 meV.

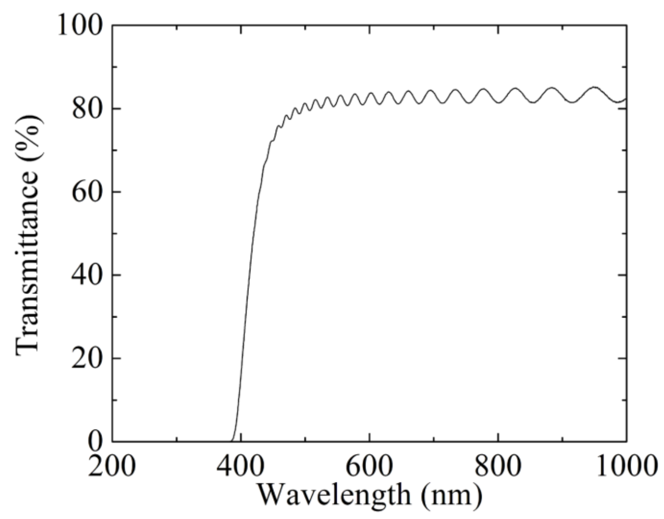

Figure 5.3 Transmittance spectrum at room temperature of a 2 μm-thick *p*-type PZO sample.

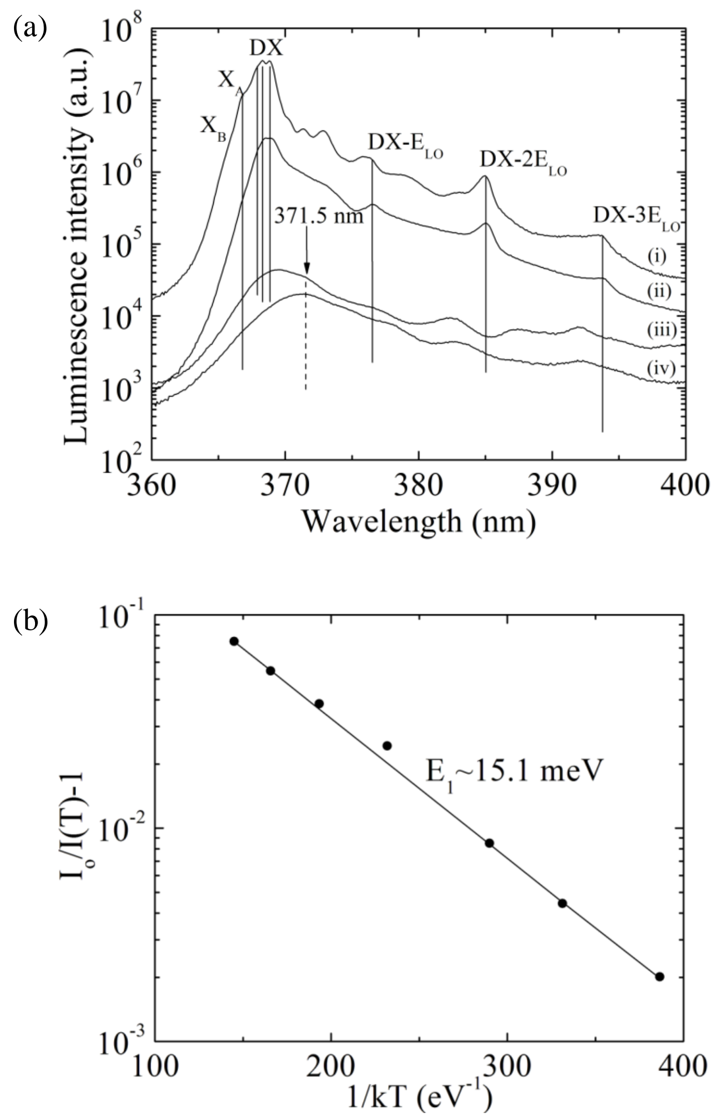

Figure 5.4 (a) PL spectra at 6 K of (i) *n*-type PZO grown at 800°C, (ii) undoped ZnO grown at 600°C, (iii) as-grown PZO at 600°C, and (iv) *p*-type PZO grown at 600°C. (b) Temperature dependence of the integrated intensity of the 371.5 nm transition. The circles are the experimental data and the solid line is the fit.

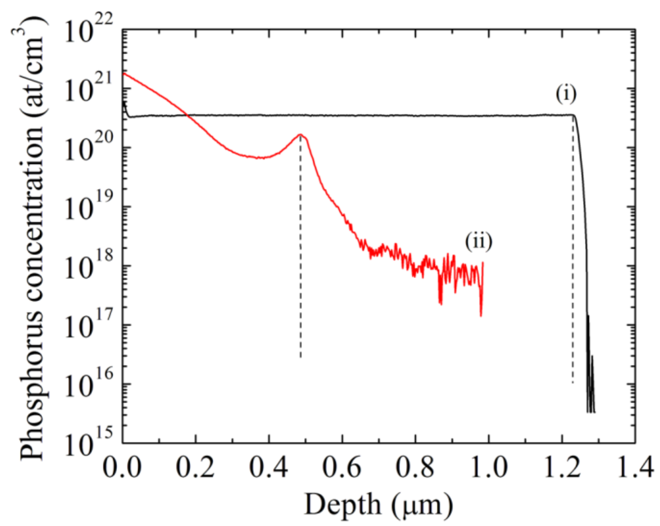

Figure 5.5 Secondary-ion mass spectroscopy of phosphorus in heteroepitaxial PZO films grown at (i) 600°C and (ii) 800°C.

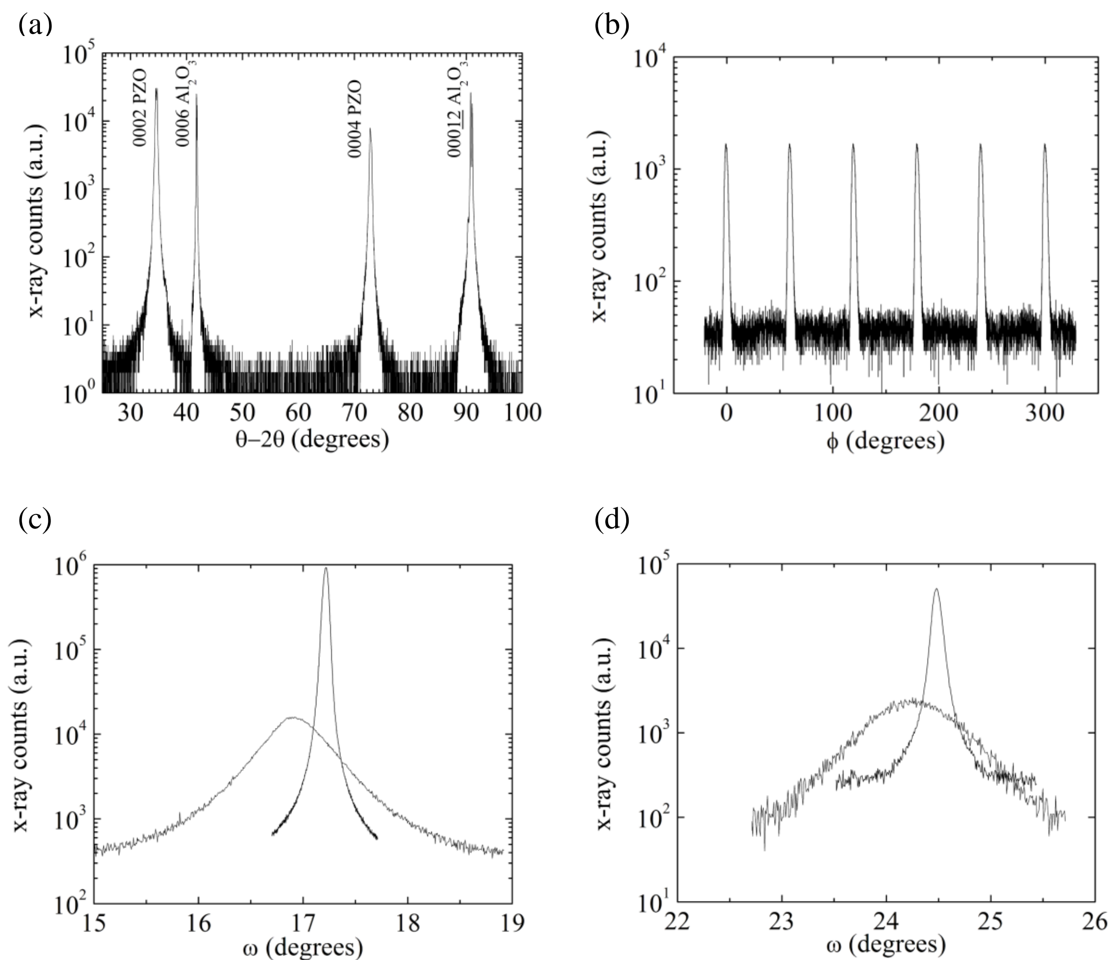

Figure 5.6 (a) Typical θ-2θ scan of PZO films grown on (0001) Al_2O_3. (b) Corresponding 11-24 ZnO ϕ-scan showing the 6-fold symmetry of the wurtzite structure and the absence of rotation domains in PZO. (c) 0002 and (d) 10-12 ω-scans of heteroepitaxial PZO films grown at 600°C (broad traces) and 800°C (narrow traces).

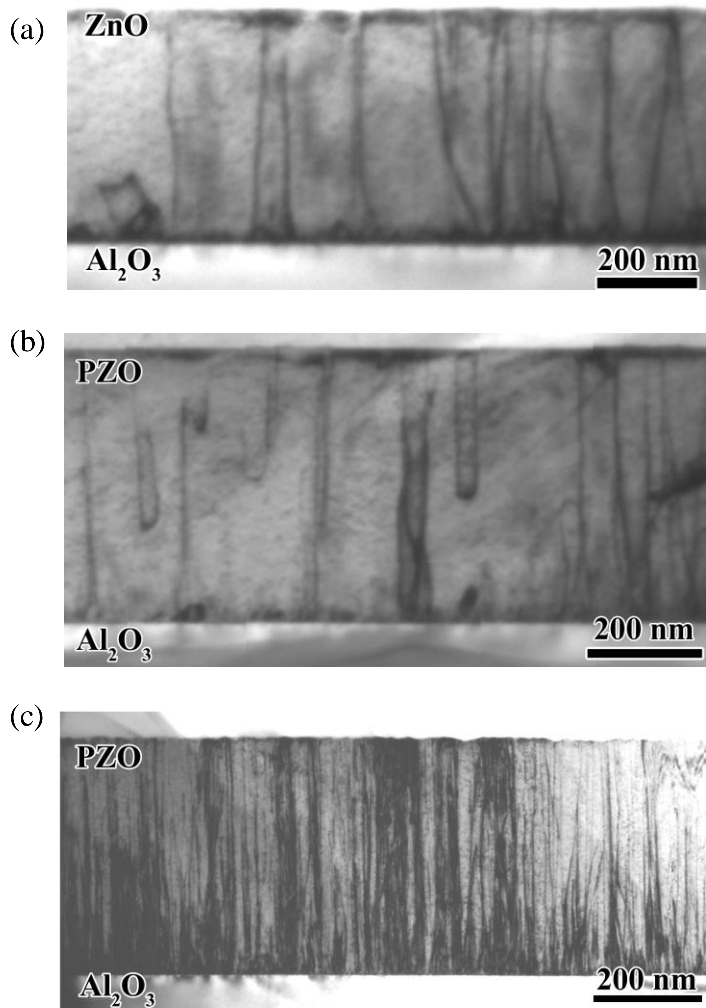

Figure 5.7 TEM images of (a) undoped ZnO grown at 600°C, (b) *n*-type PZO grown at 800°C, and (c) *p*-type PZO grown at 600°C. Note that the dislocation density increases with the increase of phosphorus doping.

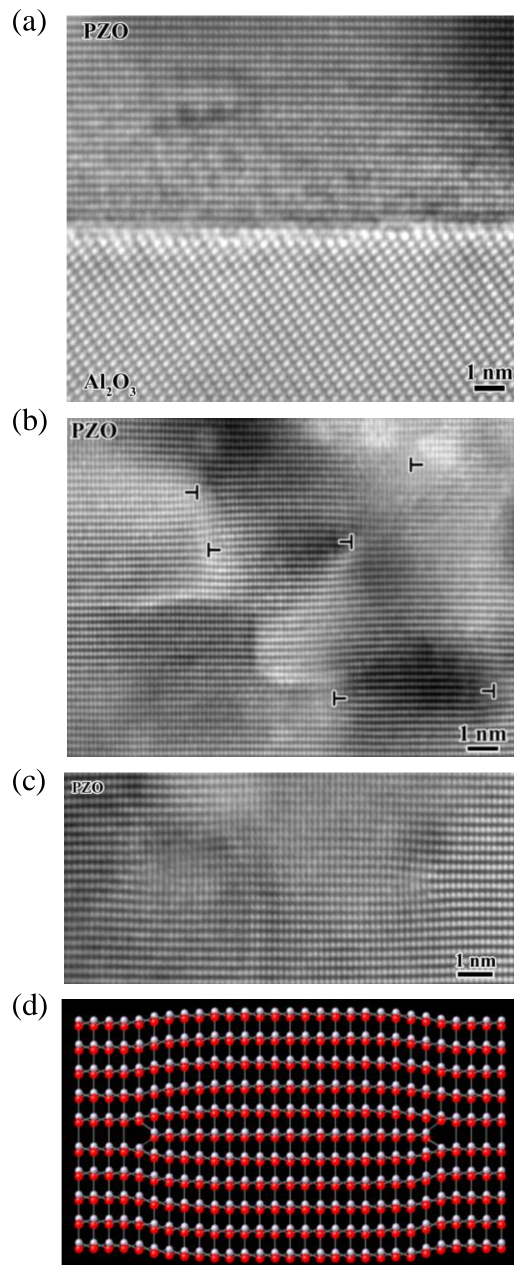

Figure 5.8 (a) HRTEM image showing the atomic structure of the interface between the PZO film grown at 600°C and the sapphire substrate. (b) HRTEM image showing the existence of partial dislocations associated with nano-sized stacking faults in the 0001 plane of *p*-type PZO. (c) Interstitial dislocation loop and (d) corresponding simulation using a ball and stick model.

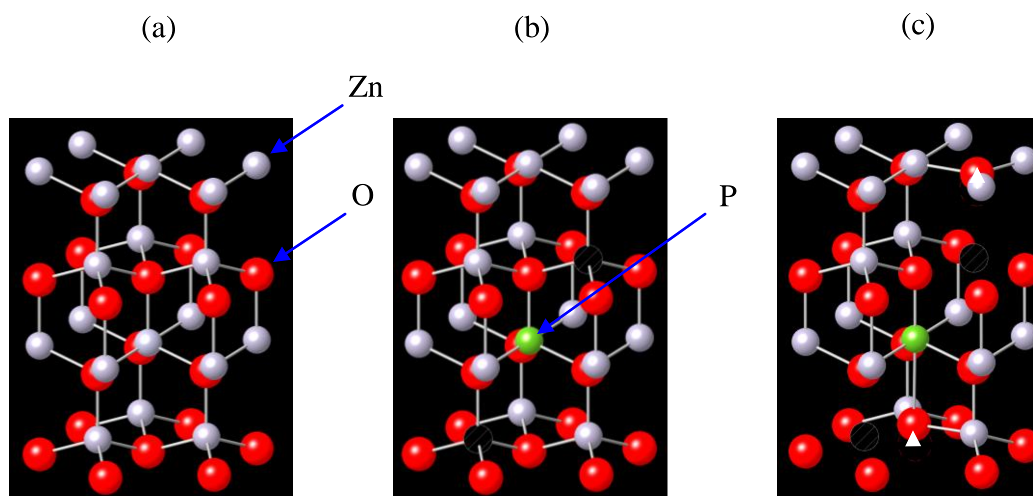

Figure 5.9 Illustration of the formation mechanism of the P_{Zn}-$2V_{Zn}$ complex in ZnO using a ball and stick model. In (a) a perfect ZnO lattice with 4 basal double layers represented, (b) the formation of a phosphorus antisite is accompanied with the formation of two zinc vacancies and (c) a rearrangement of bond lengths around the antisite. See Ref. 33 for more details.

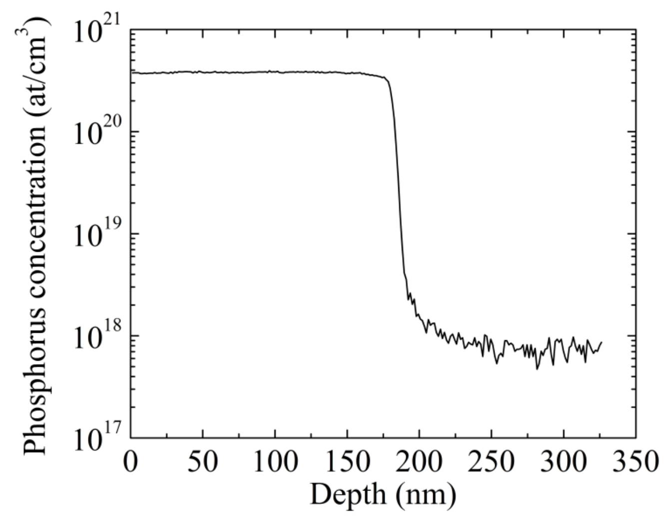

Figure 5.10 Secondary-ion mass spectroscopy of phosphorus in *p*-type homoepitaxial PZO.

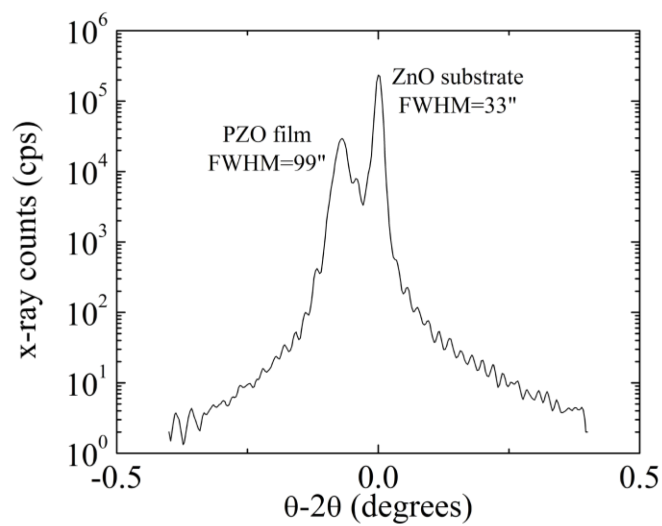

Figure 5.11 0002 θ-2θ X-ray diffraction pattern of *p*-type homoepitaxial PZO.

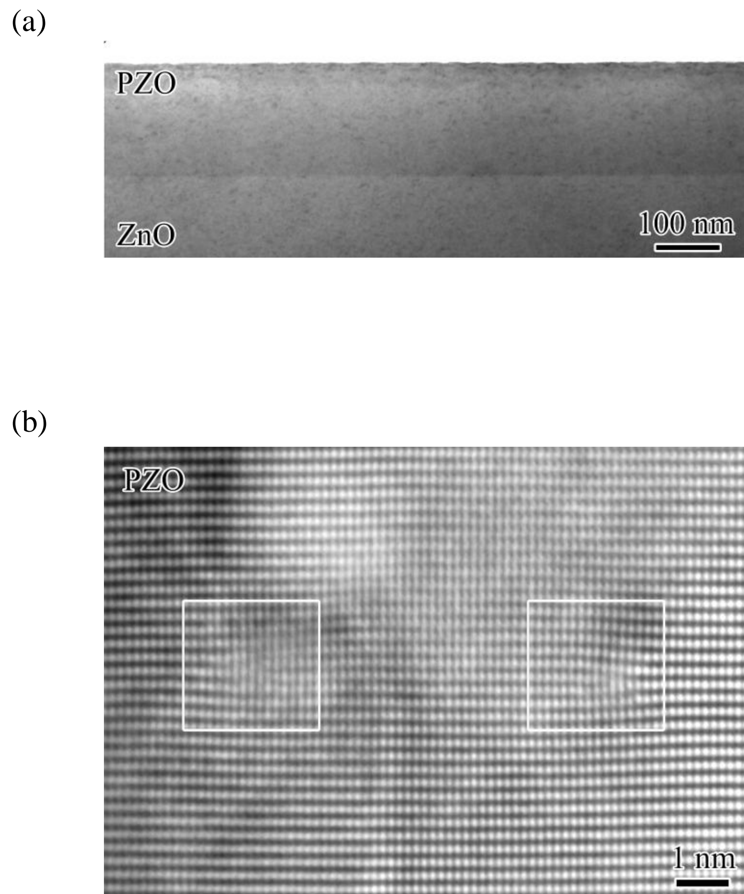

Figure 5.12 (a) TEM image of *p*-type homoepitaxial PZO highlighting a high density of short segments of stacking faults. (b) High-resolution micrograph showing the atomic structure of a pair of partial dislocations belonging to a dislocation loop.

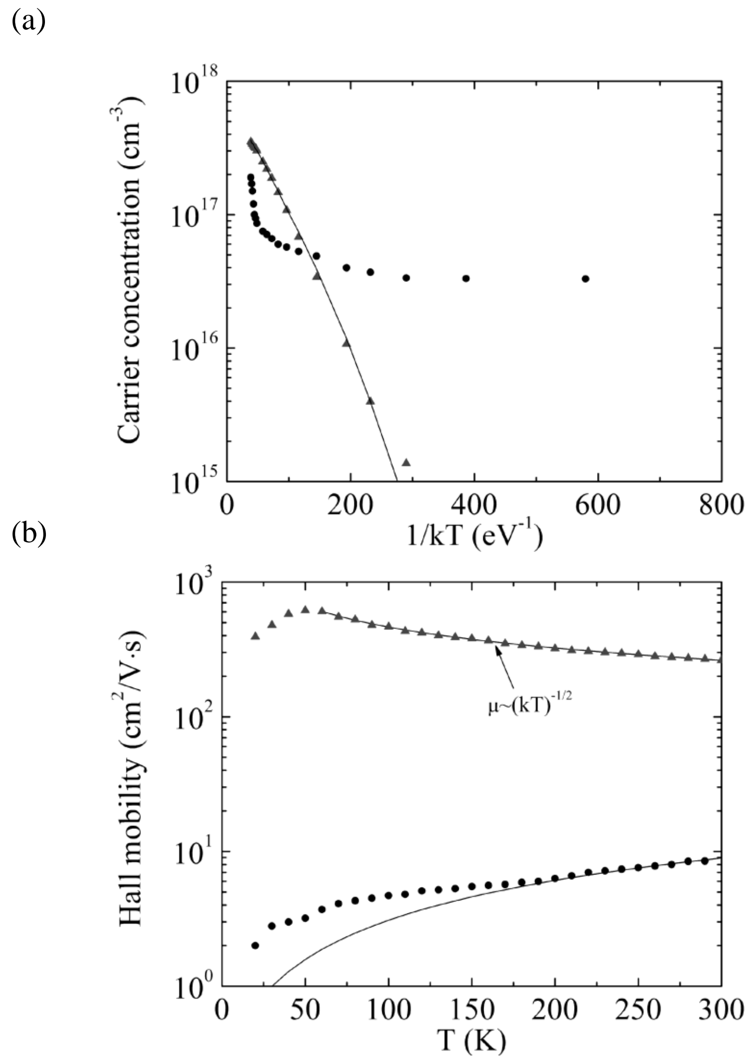

Figure 5.13 Temperature dependences of (a) the carrier concentration and (b) the Hall mobility of homoepitaxial PZO films before annealing (triangles) and after annealing in O_2 (circles).

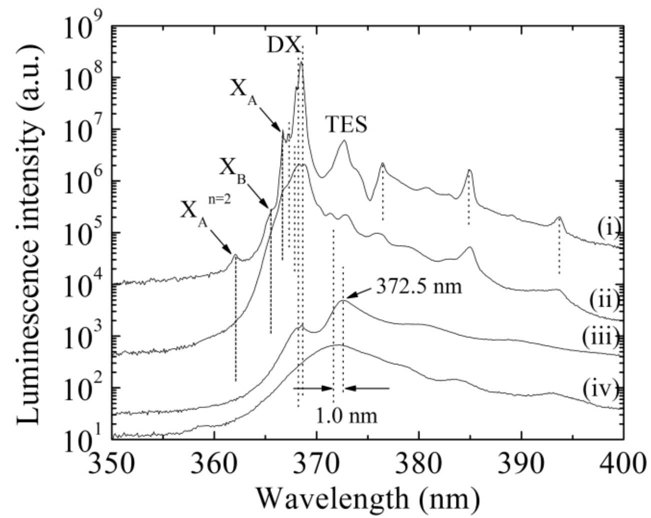

Figure 5.14 PL spectra at 12.5 K of (i) bulk ZnO, (ii) heteroepitaxial ZnO deposited on (0001) sapphire, (iii) *p*-type homoepitaxial PZO and (iv) *p*-type heteroepitaxial PZO. The comparison shows that the crystal defects induced by phosphorus doping quench the film near-band-edge luminescence.

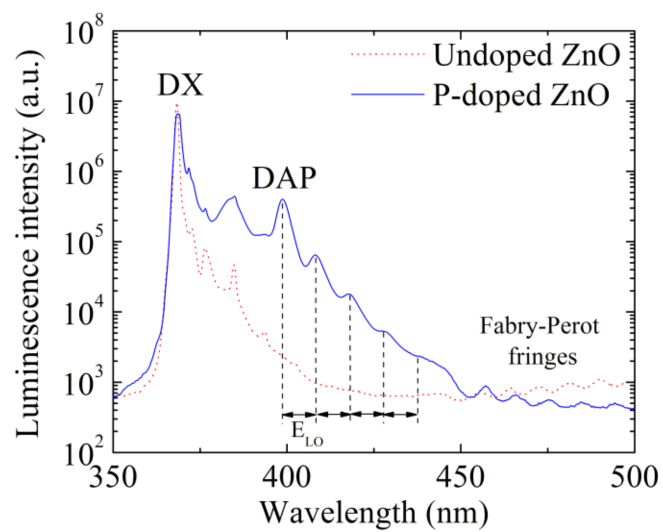

Figure 5.15 PL spectra at 12.5 K of undoped and P-doped ZnO, showing the existence of a violet luminescence band at 3.1099 eV in the P-doped sample grown by oxygen plasma-assisted pulsed laser deposition.

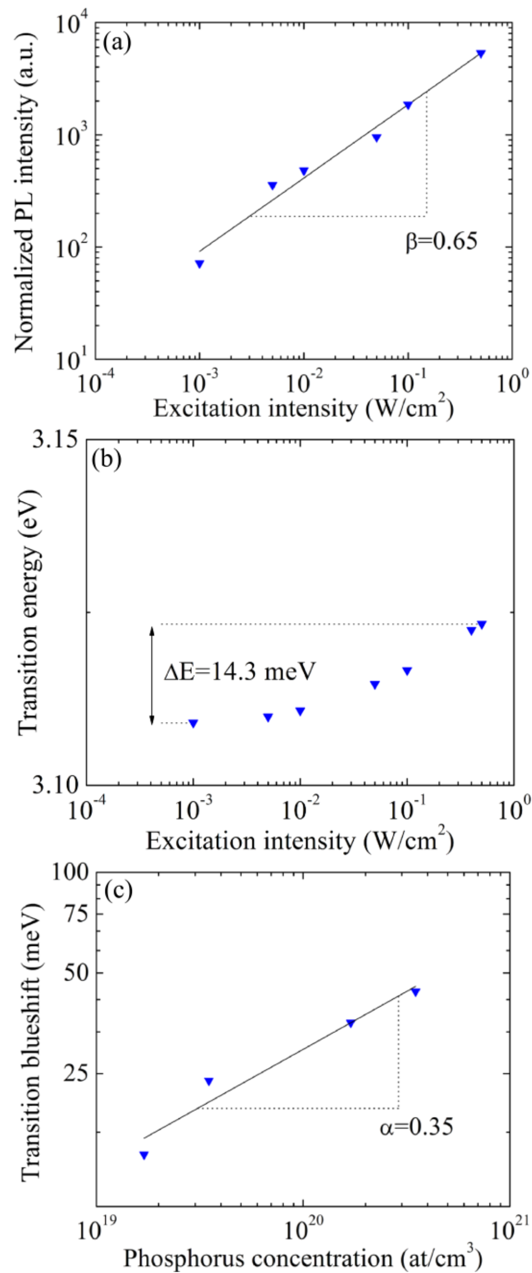

Figure 5.16 (a) Integrated intensity of the DA transition as a function of the laser excitation intensity. The triangles are the experimental data points and the solid line is the fit using a power law. (b) Energy shift of the DA transition as a function of the excitation intensity. (c) Power dependence of the DA transition on the phosphorus concentration. The triangles are experimental data points and the solid line is the fit using a power law.

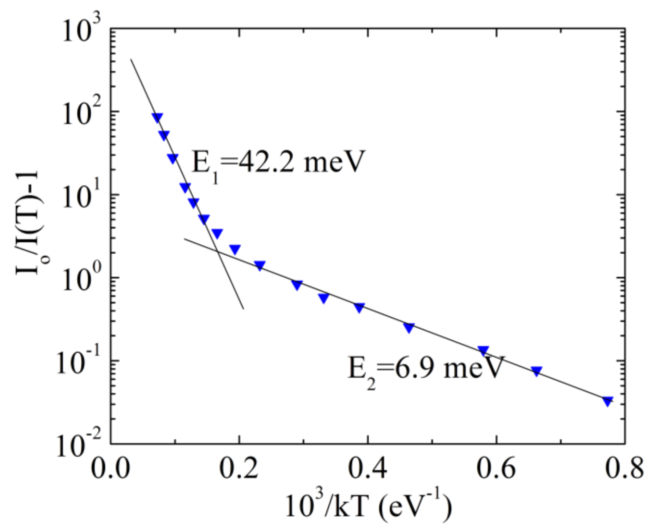

Figure 5.17 Temperature dependence of the DA transition. The triangles are the experimental data points and the curves are the corresponding fits using two Arrhenius processes.

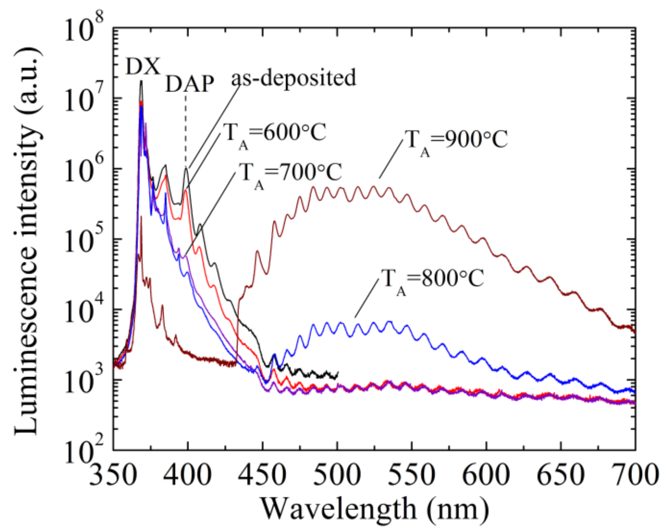

Figure 5.18 Evolution of the luminescence of P-doped ZnO as a function of the annealing temperature T_A. The violet band is entirely quenched at 900°C.

Chapter 6

Fabrication of ZnO-Based *p-n* and *p-i-n* Homojunctions

6.1 Introduction

A light-emitting device (LED) is a *p-n* junction that spontaneously emits light under a suitable forward bias. Forward bias conditions promote hole injection into the *p*-type side and electron injection into the *n*-type side. The recombination of minority carriers results in near band gap light emission. The internal quantum efficiency η_{int} depends on the radiative (τ_r) and non-radiative (τ_{nr}) carrier lifetimes:

$$\eta_{\mathrm{int}} = \frac{\tau_r^{-1}}{\tau_r^{-1} + \tau_{nr}^{-1}} \tag{6.1}$$

The lifetimes depend on the minority carrier diffusion lengths and their scattering at crystal defects, surface traps or deep levels. Minority carrier injection can be improved when band gap engineering is used to confine carriers at the *p-n* junction interface. For that reason, heterojunctions offer an interesting alternative to homojunctions despite their higher defect density. In addition, the wide gap material of an heterojunction does not reabsorb photons emitted by the active layer in the narrow gap material, thus improving the light extraction efficiency.

Due to the lack of conductive *p*-type material, most ZnO-based LEDs are heterojunctions, using ZnO as the electron injector and a different material as the hole injector. For example, Ohta *et al.* fabricated ultraviolet LEDs and detectors using *n*-type ZnO and a variety of *p*-type transparent conducting oxides ($SrCu_2O_2$, NiO and $ZnRh_2O_4$) as hole injectors.[203-207] Heterojunctions formed between *n*-type ZnO and *p*-type Si substrates have been widely investigated by Im *et al.*[208-211] Alivov *et al.* fabricated *n*-ZnO/*p*-GaN heterostructures emitting at 430 nm.[212] Taking advantage of the small lattice mismatch between ZnO and AlGaN, a heterojunction between *n*-type ZnO and *p*-AlGaN

was also fabricated.[213] The junction, emitting at 389 nm under forward bias conditions, had a turn-on voltage of 3.2 V, a low leakage current and operated at temperatures up to 500 K. Light emission at 389 nm has recently been reported in a *p*-GaN/*p*-AlGaN/*n*-ZnO/*n*-MgZnO triple heterostructure operating at temperatures up to 650 K.[214] Greenish-white emission has been observed in a *p*-$CuGaS_2$/*n*-ZnO heterojunction.[215] More recently, Rogers *et al.* reported electroluminescence at 375 nm in an *n*-ZnO/*p*-GaN/Al_2O_3 LED.[216]

Yet, the most promising ZnO LEDs so far are homojunctions and were fabricated by two hybrid growth methods. The first method alternated low-temperature growth and *in situ* rapid annealing.[73] The so-called repeated temperature modulation technique was used to enhance the solubility of nitrogen while fabricating high-quality *p*-type epitaxial films. The resulting ZnO diode was electroluminescent at 430 nm under 20 mA with a turn-on voltage of 9 V. The second *p*-*n* junction consisted of an active layer composed of seven quantum wells, with undoped ZnO and BeZnO forming the well and barrier layers respectively.[74] The diode emitted two bands between 360 and 390 nm as well as a broad defect-related band at 550 nm and had a turn-on voltage of 10 V. The luminous efficacy (or how many lumens per Watt) of these two diodes was however not measured.

In this chapter, we present our efforts to fabricate ZnO *p*-*n* homojunctions using the *p*-type material developed in chapter 5 and discuss practical issues relevant to homoepitaxial growth and *p*-*i*-*n* diode fabrication. The properties of ZnO single-crystals manufactured by various processes and *n*-type ZnO doped with various donor dopants are studied. Results of *p*-*n* homojunction growth and device fabrication are presented and some issues pertaining to electroluminescence are discussed.

6.2 ZnO substrates

One obvious advantage offered by homoepitaxial growth over the growth on (0001) Al_2O_3 is the reduction of defects induced by the lattice and thermal expansion mismatches. However, because the ZnO crystal growth technology is not yet mature, the properties of ZnO substrates vary greatly depending on the process used to fabricate them.

Prior to the growth of homojunctions, the properties of three 1×1 cm^2 Zn-face ZnO single crystals were studied. In the following, S_1 and S_2 designate crystals grown by

the hydrothermal solution method while S_3 refers to substrates fabricated by a pressurized melt growth process.[217] Figures 6.1(a)-(c) show the symmetric 0002 rocking curves of these crystals. S_1 produces the narrowest curve with a full-width at half-maximum (FWHM) of 34 arcsec. Curvature measurements (2θ-scans along directions parallel to the edges) showed almost no curvature. The FWHM of S_2 was 36 arcsec. Several measurements of S_3 revealed a large scatter in the rocking curve linewidths. Most samples were characterized by a 3-4° miscut parallel to the basal plane and showed various tilt boundaries with a relative misorientation in the range of 0.02-0.05°. Some samples were similar to polycrystals. Note that the half-width of the rocking curve was on the order of 0.1°

The surface readiness for homoepitaxial growth was studied by atomic force microscopy. As seen in Fig. 6.2(a)-(c), no step and terrace structures were observed in as-received substrates, consistent with other reports.[31] Yet, most substrates had relatively smooth surfaces with root-mean-square roughnesses on the order of 2 Å. The chemico-polishing lines were visible in S_1 and S_2. The surface of S_3 was the most irregular, sometimes with visible damage and defects. Note that the surface of each substrate was systematically treated prior to growth by a 30 minute-anneal in vacuum at 800 °C.

The electrical properties at 300 K are summarized in Table 6.1. The substrates grown hydrothermally are always semi-insulating, possibly because of the compensation induced by group-I elements. Group-I elements are residues of the growth solvent and behave as deep acceptors in ZnO.[181] Recent reports have shown that these substrates become n-type with electron concentrations on the order of 10^{16} cm^{-3} after thermal annealing above 1100 °C in O_2.[31] Despite poor surface and crystalline properties, S_3 was n-type conductive and suitable for top-to-bottom contacting.

Figure 6.3 compares the near-band-edge photoluminescence at 10 K of the substrates. The observation of free-excitonic transitions and the sharpness of bound excitons are taken as an indication of material optical quality. We therefore conclude that S_3 is optically the least perfect crystal.

6.3 Homojunction fabrication

Three elements (Al, Ga and P) were investigated as potential *n*-type dopants in ZnO. The donor-doped layers were grown at a rate of 1 Å per second on a 150 nm-thick ZnO buffer layer deposited at 600 °C in 2.7×10^{-4} mbar O_2. The *n*-type layers had a thickness of 0.9-1.1 μm.

The first homojunction was fabricated by depositing an *n*-type PZO layer at 800 °C on both Al_2O_3 and S_3 substrates and a *p*-type PZO layer grown at 600 °C atop the *n*-type layer. The homojunction was then annealed in O_2 at 600 °C. Figure 6.4 shows the corresponding I-V characteristics of the *n*-type layer (curve a), *p*-type layer (curve b) and *p*-n junction on sapphire (curve c) and on ZnO (curve d). The Shockley diode equation can be written as:

$$\frac{i(V)}{i_s} = (\exp(\frac{eV}{\zeta kT}) - 1) \qquad (6.2)$$

where i_s is the saturation current and ζ is the ideality factor. By fitting the linear segment of the curve under positive bias, we obtained a turn-on voltage of ~6.5 V and an ideality factor of ζ=1.7±0.2. The threshold is relatively large possibly because of the low level of hole conduction in the *p*-type layer. It should also be noted that above the threshold, the current does not increase exponentially with the bias voltage but is limited by a resistance of about 30 Ω. This resistance is on the same order as that across the electrodes of the *n*-type layer, suggesting that its current spread resistance limits the current. Note that a conductive ZnO substrate in place of the *n*-type layer would reduce this resistance and considerably simplify the device structure. The junction had a breakdown voltage of 13 V with a leakage current that increased slightly under increasing reverse bias. Finally, in order to study the stability of the *p*-n junction, the I-V characteristics across the homojunctions were measured after four and eight months (curves e and f). The measurements show that the *p*-n junction behavior did not change within the eight-month period.

As discussed in chapter 5, phosphorus-doped ZnO layers deposited at 800 °C on ZnO-buffered (0001) sapphire are characterized by a severe surface roughening due to the segregation of phosphorus to the surface. Besides, these layers exhibit relatively broad excitonic transitions and impurity-dominated conduction.

Group-III elements can be thought as excellent alternatives to P for *n*-type doping of ZnO. Al suffers from its high reactivity, which in some processes such as molecular beam epitaxy can cause oxidation of the aluminum source during growth.[218] Rapid diffusion of Al to the surface of ZnO films heteroepitaxially grown on Al_2O_3 above 650 °C was observed by SIMS. Growth at lower temperatures resulted in large X-ray and PL broadening, therefore these layers were not further studied for homojunction application. The size mismatch between Ga-O (1.92 Å) and Zn-O (1.94 Å) bonds is small, therefore substitution of Ga to the Zn site should result in a smaller lattice deformation than that induced by In-O (2.1 Å) or Al-O (1.8 Å). A 0.1 wt. % Ga_2O_3-doped ZnO target was used for the growth of Ga-doped ZnO films. The layers were deposited at 780 °C.

The requirements for homojunction applications include a smooth surface, an electron density above 10^{18} cm^{-3}, a large transmittance to minimize photon absorption and a low density of threading dislocations propagating to the interface with the next layer. The surface of *n*-type Ga-doped ZnO was typically granular with spherical grains of 50-150 nm scale and a roughness around 3 nm. Electrical measurements at room temperature gave: $\rho=2.6\times10^{-2}$ $\Omega\cdot$cm, $\mu=45$ cm^2/V·s and $n= 5\times10^{18}$ cm^{-3}. We measured rocking curve half-widths for (0002) and $(10\bar{1}2)$ of 0.067° and 0.217°, corresponding to dislocation densities in the low 10^9 cm^{-2} range. Finally, the 12.5 K photoluminescence spectrum of Ga-doped ZnO was dominated by three donor-bound excitons, with the deepest donor being the most intense, thus implying that it is directly related to Ga. Note that a higher Ga concentration resulted in a significant X-ray broadening and a decrease of the NBE/DL intensity ratio, possibly because of the generation of doping-induced defects, or local clustering of Ga dopants.

The interface between the *n*-type layer and the *p*-type layer was affected by the formation of droplets. 100 nm-scale droplets of hexagonal shape were observed and their surface density depended on the target surface quality (5×10^7 cm^2 at most without careful target preparation). It is standard to polish the target to improve on the stability of the plume during growth and avoid effects of splashing induced by surface ripples and cones. Yet, this polishing step generally introduces impurities, hence the need to ablate the target prior to growth, which inevitably results in new surface modification. For

multilayer growth, it was thus critical to systematically polish the targets and minimize the duration of the pre-ablation step.

The *p*-type layers were grown following the procedure outlined in chapter 5. An important parameter to decide is the thickness of the *p*-type layer. For simple homojunction structures fabricated without patterning, the thickness of the *p*-type layer should be relatively small in order to avoid photon re-absorption, yet it should be thick enough to prevent depletion. Assuming $N_D >> N_A$ where N_D is the donor level density in the *n*-type layer and N_A is the acceptor level density in the *p*-type layer, the depletion width W into the *p*-type layer is given by:

$$W = \left(\frac{2\varepsilon_s \varepsilon_o kT(N_A + N_D)}{eN_A N_D} \ln(\frac{N_A N_D}{n_i^2}) \right)^{1/2} \qquad (6.3)$$

where n_i=5×10^{16} cm^{-3} is the intrinsic concentration of ZnO. Figure 6.5 shows the dependence of the depletion width on the electron concentration of the *n*-type layer. It can be seen that for an electron concentration of 5×10^{18} cm^{-3}, which is that of the *n*-type layer employed in this study, the thickness of the *p*-type layer should be at least 170 nm. Note that another approach is to directly grow the *p*-type layer on the sapphire substrate and then grow an *n*-type layer atop. However, issues of contact resistance and process prevent the realization of such device.

6.4 Issues pertaining to electroluminescence

Figure 6.6(a) is a schematic cross-section of the device structure while Fig. 6.6(b) is an optical micrograph of the real device structure. The diameter of the outer ring is on the order of 50 μm. Despite the good I-V characteristic and stability of the junction shown in Fig. 6.4, no electroluminescence (EL) was observed at room temperature. The hole concentration in the *p*-type layer may not be high enough (<10^{18} cm^{-3}) to turn on any near-band-edge emission. Secondly, the role of crystal defects on the device performance is critical. The leakage current in junctions grown on sapphire is slightly larger than on ZnO highlights the detrimental effect of crystal defects such as threading dislocations on the recombination efficiency and junction property. Furthermore, the high-density (10^{11} cm^{-2}) of threading dislocations in the *p*-type layer provides radiative recombination traps, especially since the dislocation spacing, as small as 3 nm in some areas, is much less than

the minority carrier diffusion length in *p*-type ZnO, which is typically 0.5-1 μm.[219] In particular, the low luminescence yield at 300 K of the *p*-type layer in the device, shown in Fig. 6.7 in comparison with that of homoepitaxially-grown undoped ZnO, is possibly the major reason why no electroluminescence has been observed.

For the junctions grown on ZnO substrates, the low-angle tilt boundaries observed by X-ray diffraction at the surface of the substrate act as leakage paths. In addition, the mobility of dislocation loops upon application of a bias may also degrade the *p-n* junction, as observed in ZnSe-based devices.[220] In P-doped ZnO, the acceptor complexes responsible for the *p*-type conductivity are stabilized in the vicinity of the lines of the partial dislocations and may be destabilized by their motion.

6.5 Conclusions

Though the rectifying characteristic of ZnO homojunctions confirms the *p*-type behavior of the P-doped epilayers, the achievement of electroluminescence is challenging based on the above process-related issues. Another issue comes from the necessity to dope ZnO heavily to achieve *p*-type conductivity. The high density of crystal defects such as dislocation loops provides radiative recombination traps. One approach to improve on the hole concentration of *p*-type P-doped ZnO is to rely on band gap engineering and use (MgO-P_2O_5) co-doped ZnO targets. Another possibility is to fabricate type-I heterostructures using Ga-doped ZnO as electron injector and a hybrid *p*-type oxide. These approaches will be described in chapter 8.

Table 6.1 Electrical properties at room temperature of the ZnO substrates.

Substrate	*Thickness* (μm)	*Resistiviy* ($\Omega \cdot cm$)	*Carrier density* (cm^{-3})	*Hall mobility* ($cm^2/V \cdot s$)
S_1	525	6.5×10^{3}	6.1×10^{12}	160
S_2	525	8.5×10^{1}-1.6×10^{3}	3.5×10^{13}-6.7×10^{14}	110
S_3	325	3.5×10^{-1}	9.2×10^{16}	190

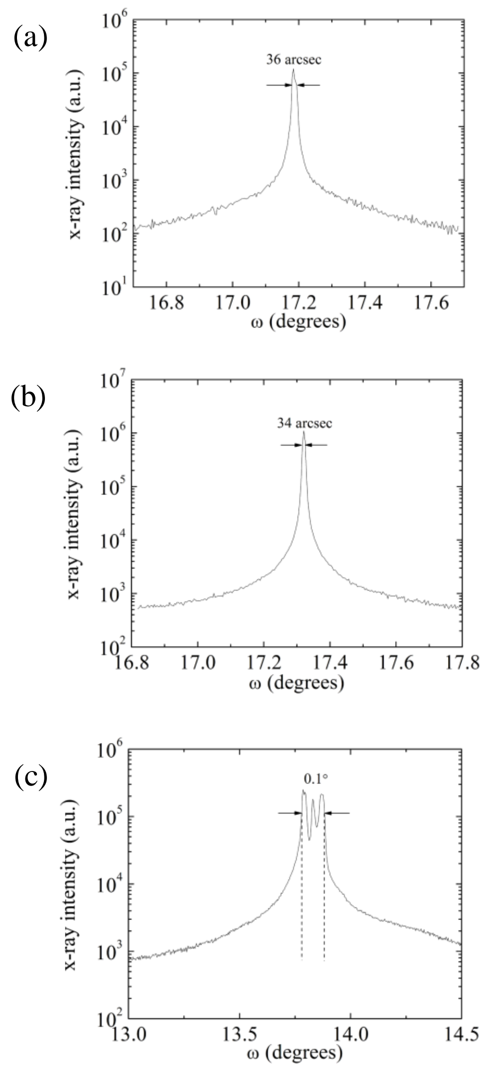

Figure 6.1 0002 ω-scans of the (a) S_1, (b) S_2 and (c) S_3 ZnO crystals. Note the large miscut in S_3 and the existence of low tilt angle boundaries.

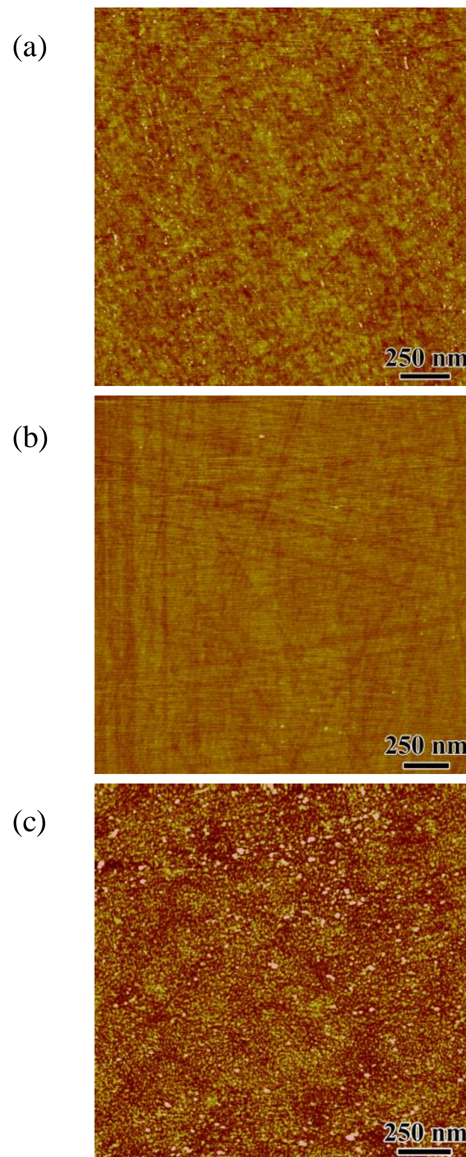

Figure 6.2 2×2 μm^2 AFM scans of the as-received surfaces of the (a) S_1, (b) S_2 and (c) S_3 ZnO crystals. The Z-height is 5 nm.

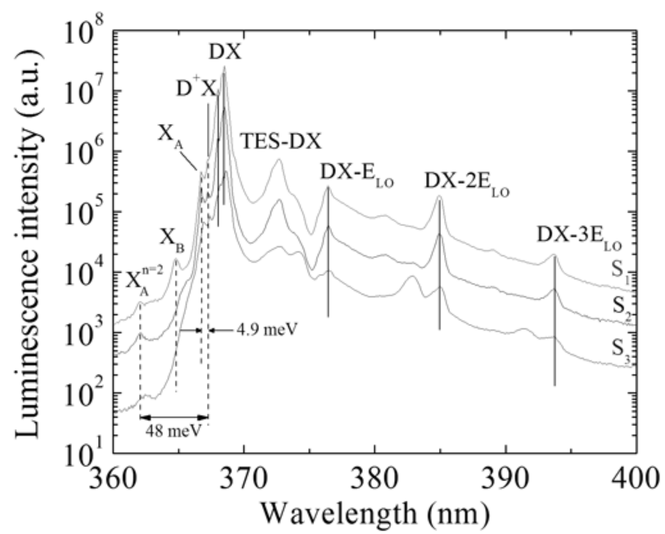

Figure 6.3 Comparison of the NBE photoluminescence at 10 K of the ZnO substrates. Note the broader excitonic transitions and the higher background level in S_3.

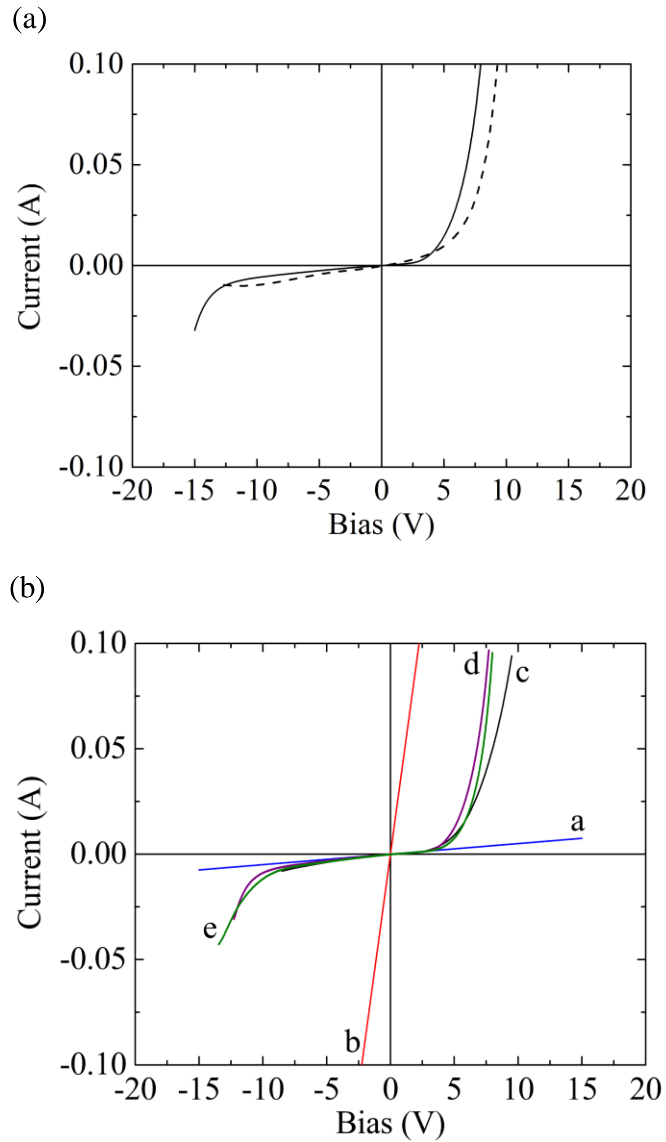

Figure 6.4 (a) Comparison between the I-V curves of *p*-*n* junctions grown on sapphire (dashed line) and ZnO (solid line). (b) I-V characteristics of a) Ti/Au contacts on the bottom *n*-type PZO layer and b) Ni/Au contacts on the top *p*-type PZO layer. c), d) and e) The rectifying I-V characteristics of the corresponding *p*-*n* homojunction grown on ZnO measured over a period of eight months.

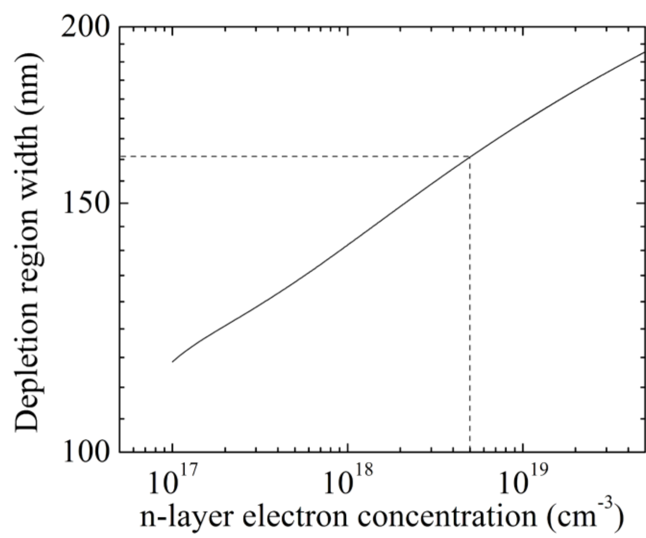

Figure 6.5 Depletion width of the *p*-type layer as a function of the electron concentration in the *n*-type layer. In this work, the electron concentration of the *n*-type layer is at least 5×10^{18} cm^{-3}.

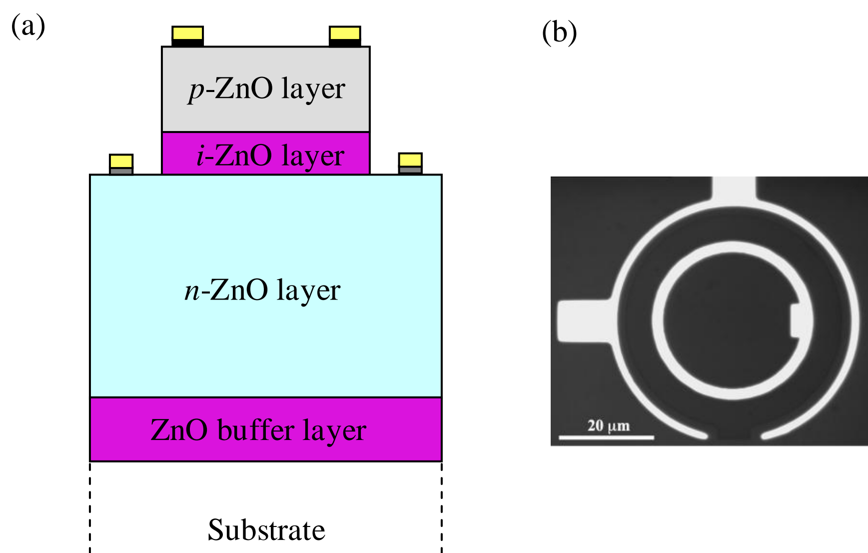

Figure 6.6 (a) Cross-sectional illustration of the ZnO-based *p-n* homojunction. (b) Top-view of the mesa device. The outer ring provides two bonding pads for bottom contacting while the inner ring contacts on the *p*-type layer.

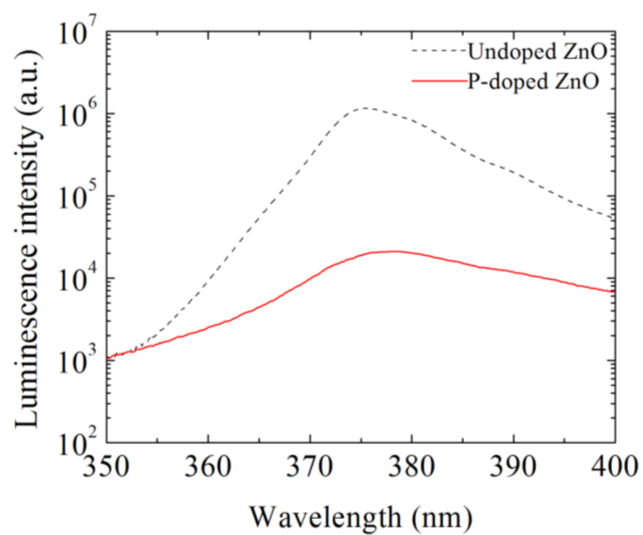

Figure 6.7 NBE photoluminescence spectra at 300 K of the *p*-type layer grown on top of the device (solid curve) and of undoped ZnO grown on a ZnO substrate (dotted curve).

Chapter 7

Thesis Conclusions

This thesis focused on the relationships between the microstructures and the optoelectronic properties of *p*-type ZnO epilayers. The objectives were to fabricate *p*-type ZnO material, understand the role of crystal defects on the onset of *p*-type conductivity and explore the potential of *p*-type ZnO for light-emitting diode applications. The following conclusions are drawn.

7.1 Effect of doping on the microstructure of ZnO

Doping ZnO with acceptors to achieve *p*-type conductivity increases the density of crystal defects. In heteroepitaxial films doped with phosphorus, the low diffusivity of the phosphorus atom and its large size mismatch with host atoms result in a considerable increase in the density of threading dislocations. A similar conclusion was drawn for Sb-doped ZnO films.[221] In homoepitaxial films, the primary defects are interstitial dislocation loops bound with two partial dislocations. These abundant defects (10^{11}-10^{12} cm^{-2}) result from the precipitation of excess zinc interstitials which form in order to balance the loss of zinc vacancies complexed with P_{Zn}. Two zinc vacancies and an antisite, the latter being most likely located in the vicinity of the partial dislocation lines, can stabilize shallow complex acceptors, resulting in *p*-type conductivity after a post-growth annealing in oxygen. When an oxygen plasma is used during growth, the dominant acceptor is the zinc vacancy. The complex formation is thermodynamically not favorable. The films remain *n*-type because the zinc vacancy is too deep to overcome the electron concentration induced by native defects and phosphorus antisites. In heteroepitaxial films doped with nitrogen, the solubility of nitrogen is limited by the substrate temperature, which affects the stability of the Zn-N bond. The columnar grains

in samples grown at low temperature result from the high density of Zn-N clusters at the growth front and the limited surface diffusion. These grains can pin the nitrogen atoms at their boundaries, hence the uniform nitrogen depth-profile.

7.2 Effect of doping on the optoelectronic properties of ZnO

The optical and electrical properties of ZnO are very sensitive to minute concentrations of impurities. The transition at 371.5 nm and the red band at 640 nm in *p*-type phosphorus-doped ZnO involve the P_{Zn}-$2V_{Zn}$ acceptor level. When an oxygen plasma is used during growth, the photoluminescence features a strong but deep donor-acceptor transition. Despite the quasi elimination of threading dislocations in homoepitaxial phosphorus-doped ZnO samples, the near-band-edge luminescence is still quenched. The crystal defects such as dislocation loops or the point defects gettered at these crystal defects introduce deep and strongly localized transitions (*Y*-lines) at 372-373 nm. Heavy doping ($>5\times10^{19}$ at/cm^{-3}) with phosphorus quenches the near-band-edge luminescence due to the doping-induced non-radiative recombination centers

Heavy doping results in degenerate electrical behavior, as observed in *n*-type nitrogen-doped ZnO. Ionized impurity scattering dominates in non-stoichiometric layers while dislocation scattering dominates in layers with edge-type dislocation densities above 10^8 cm^{-2}. The conductivity type results from the interplay between doping-induced crystal defects and native point defects. Without O_2 plasma, phosphorus doping induces crystal defects that can stabilize shallow acceptors with the aid of a native acceptor (V_{Zn}). Annealing helps minimize the concentration of native hole killers. In contrast, when an O_2 plasma is used, phosphorus doping induces native acceptors (V_{Zn}). These are compensated by doping-related donors and disappear upon annealing.

7.3 Impact of this work

The impact of this work is to offer some understanding of the microscopic effects of doping and correlate these effects with the macroscopic properties of ZnO. This work addresses fundamental issues pertaining to *p*-type doping of ZnO and proposes solutions to tackle these issues. For example, in chapter 4, the low nitrogen solubility issue was overcome by developing a one step process that produced epitaxial *p*-type material of

reasonable quality. Evidence was brought that phosphorus is an amphoteric dopant in ZnO and a mechanism explaining the role of defects on the formation of acceptors was proposed. While donor defects form spontaneously, the formation of shallow acceptors results from the interactions between P_{Zn} donors, V_{Zn} native acceptors and dislocations. Finally, the realization of simple ZnO devices was explored by developing a process to fabricate mesas. Practical issues against electroluminescence, which are of interest to researchers developing ZnO-based homojunctions for LED applications, were discussed. While the P-doped ZnO epilayers studied in chapter 6 show stable *p*-type conductivity (p~10^{17} cm^{-3}), defect-mediated transport and luminescence quenching induced by crystal defects such as dislocation loops and threading dislocations reduce the internal quantum efficiency of the device so that no light can be observed with the naked eye.

Chapter 8

Future Work Recommendations

8.1 Band gap engineering in the low doping limit

One obvious way to verify that doping introduces acceptors is the observation by photoluminescence of donor-acceptor transitions. Donors are so shallow in ZnO (30-65 meV) that the energy position of the donor-acceptor transition determines how deep the energy level of the acceptor is. An interesting question is whether or not it is possible to experimentally "shift" the donor-acceptor transition towards smaller wavelengths. In the case of phosphorus doping, our results show that acceptors are shallower when growth is carried out in the low doping limit ($[P]\sim10^{19}$ cm^{-3}).[182] Therefore, it is of interest to further explore the effect of phosphorus doping in the low doping limit (10^{18}-10^{19} cm^{-3}).

It is experimentally almost impossible to predict the recombination energy of a DA pair. Band gap engineering can however be used to increase the energy separation between the conduction band edge and the Fermi level pinning energy. Band gap engineering can be done via dilute alloying with BeO or MgO gap.[17,18] In the case of MgO, a 30 at. % solubility limit has been reported. Because it is the competition between donors and acceptors in P-doped ZnO that accounts for the difficulty to obtain *p*-type conductivity, band gap engineering may be a reliable method to maximize the ionization energies of donors (ideally so that E_D>150 meV) and promote hole concentrations of more than 10^{17} cm^{-3}. Note that band gap engineering is an important step in device fabrication because it can be used for minority carrier confinement for improved recombination efficiency and thus higher internal quantum efficiency.

8.2 Epitaxial growth on alternative substrates for increased functionality

8.2.1 Epitaxy in non-polar directions

Recent groundbreaking reports[10] of enhanced LED efficiency stimulate the growth of devices and epilayers in a non-polar direction in order to avoid the scattering effects of spontaneous and piezoelectric polarization fields on excitons (Stark effect), which limit the luminous efficiency. The growth of ZnO layers and devices in a non-polar direction sapphire (such that the ZnO layer grows with its *c*-axis in the plane) is therefore of technological interest. For example, transverse acting devices such as surface acoustic wave devices should be more functional when the ZnO layer grows in a non-polar direction. The [0001] axis of the ZnO wurtzite structure is anisotropic and polar. Any direction orthogonal to [0001] does not carry any spontaneous polarization. Piezoelectric polarization can itself be minimized by reducing the strain in the epilayer.

In analogy with the growth of epitaxial GaN on (100) $LiAlO_2$,[122] it should be possible to grow epitaxial and single-crystalline ZnO on tetragonal $LiAlO_2$ with $(1\bar{1}00)_{ZnO} // (100)_{LiAlO_2}$. However, such material may suffer from the thermal instability of Li at elevated temperatures. While ZnO epitaxy is possible, the non-controllable migrations of Li and Al into the ZnO layer would be significant issues against high-purity epitaxial growth.

8.2.2 Epitaxy on YSZ and Si

It is worth mentioning about the epitaxial growth of ZnO on Y_2O_3-ZrO_2 (YSZ). YSZ crystallizes in the CaF_2-structure (space group Fm3m) with a lattice parameter a_{YSZ}=5.1347 Å. When (0001) ZnO grows on the (111) surface of YSZ, the lattice mismatch is ~-10.6%. This number is unfortunately still relatively large and should result in dislocation densities on the order of 10^8 cm^{-2} or more in the epilayer. While YSZ offers similar properties to Al_2O_3 in terms of transparency and chemical robustness, its unique advantage comes from its atomically flat surface

Though Al_2O_3 and SiC are substrates of choice for ZnO epitaxy, the applicability of ZnO devices into the microelectronics industry calls for the growth on Si. Growth of device-quality ZnO epilayers on Si can be challenging because of the large lattice and thermal expansion mismatches with the substrate, and the resulting tensile strain in the

epilayer. Yet, single-crystalline ZnO films have seldom been achieved[222-224] and other issues such as crack formation upon post-growth cooling and complicated multi-step buffer layer processing also exist. Novel rare-earth intervening layers can be developed to achieve the fabrication of single crystalline, crack-free, epitaxial (0001) ZnO films grown on (111) Si substrates using intervening epitaxial Lu_2O_3.[225] While most devices are grown on the (100) face of Si, the choice of (111) Si is dictated by the crystal structures of Lu_2O_3 and ZnO. The lattice mismatch between $[1\bar{2}10]$ ZnO and $[\bar{1}10]$ Lu_2O_3 is 11.4 %, which is smaller than that between ZnO and Si. Lu_2O_3 epilayers with excellent crystallinity (9 arcsec for the rocking curve of 220 Lu_2O_3) can be grown on Si by molecular beam epitaxy. Other rare earth oxides such as Sc_2O_3 or Gd_2O_3 can be selected to further improve on the epitaxial quality of the ZnO films. Sc_2O_3 has a 6.6% lattice mismatch with ZnO and a 9.4% mismatch with Si, while Gd_2O_3 has a 15% mismatch with ZnO and a 0.4% with Si. It may be possible to reduce the phosphorus concentration in order to achieve *p*-type conductivity and improve the luminescence yield in ZnO, simply because the crystallinity of $ZnO/X_2O_3/Si$ layers (X=Gd, Lu, Sc) surpasses that of ZnO/Al_2O_3 layers. One requirement, however, is to reduce the electron concentration in undoped $ZnO/X_2O_3/Si$ layers.

With the growth of epitaxial ZnO on Si made possible, new applications open up, and in particular, the fabrication of *p-n* homojunction devices on Si. Using the processing route discussed in chapter 6 for *p*-type P-doped ZnO, it should be possible to grow epitaxial *p-n* junctions on (111) Si. One issue to address, however, is the small critical thickness before cracking in ZnO occurs, which for a growth on Lu_2O_3/Si at 600 °C has been estimated to be about 600 nm.[225] This obstacle can be overcome by reducing the thickness of the *n*-type layer to about 300 nm; that of the *p*-type layer should at least exceed the thickness for depletion (~200 nm depending on the electron concentration in the *n*-type layer).

Appendix A

Lattice parameters and epilayer strain analysis using asymmetric XRD measurements

A.1 Lattice parameters and strain

XRD in the glancing incidence geometry is a powerful technique to accurately determine the lattice parameters, percentage of relaxation and strain state in epilayers grown on substrates.

In all of the following, the subscript "s" refers to the substrate while the subscript "l" refers to the epilayer.

Let us assume that the normal to the epilayer surface is parallel to [0001].

Let θ_l the Bragg angle of the epilayer for an $hk\overline{h+k}l$ plane.

Let ϕ_l the inclination angle between the $hk\overline{h+k}l$ plane and the 0001 surface plane of the epilayer.

In the hexagonal lattice:

$$\tan(\phi_l) = \sqrt{\frac{4}{3}} \frac{\sqrt{h^2 + hk + k^2}}{l} \frac{c}{a} \qquad \text{(A.1)}$$

The interplanar spacing d_{hkl} is given by the following matricial relationship:

$$\frac{1}{d_{hkl}^2} = \begin{bmatrix} h & k & l \end{bmatrix} \begin{vmatrix} \frac{4}{3a^2} & \frac{4}{6a^2} & 0 \\ \frac{4}{6a^2} & \frac{4}{3a^2} & 0 \\ 0 & 0 & \frac{1}{c^2} \end{vmatrix} \begin{bmatrix} h \\ k \\ l \end{bmatrix} \qquad \text{(A.2)}$$

$$\frac{1}{d_{hkl}^2} = \frac{4}{3a^2}\left[h^2 + hk + k^2\right] + \frac{l^2}{c^2} \qquad \text{(A.3)}$$

Using Bragg law for the epilayer:

$$\frac{4\sin^2(\theta_l)}{\lambda^2} = \frac{4}{3a_l^2}\left[h^2 + hk + k^2\right] + \frac{l^2}{c_l^2} \tag{A.4}$$

Combining Eq. (A.3) and Eq. (A.4):

$$\frac{4\sin^2(\theta_l)}{\lambda^2} = \frac{l^2}{c^2}(\tan^2(\phi_l) - 1) \tag{A.5}$$

Solving for the epilayer lattice parameter c_l:

$$c_l = \frac{l\lambda}{2\cos(\phi_l)\sin(\theta_l)} \tag{A.6}$$

Using Eq. (A.1) to extract a_l:

$$a_l = \frac{\lambda}{2\sin(\theta_l)}\sqrt{h^2 + k^2} \tag{A.7}$$

Under the assumption that the layer is fully strained, the strain along the *c*- and *a*- axes are defined as follows:

$$\varepsilon_{cc} = \frac{c_l - c_s}{c_s}$$
$$\varepsilon_{aa} = \frac{a_l - a_s}{a_s} \tag{A.8}$$

Under the biaxial strain approximation, the Poisson ratio ν is defined as:

$$\frac{\varepsilon_{cc}}{\varepsilon_{aa}} = -\frac{2\nu}{1-\nu} \tag{A.9}$$

A.2 Reciprocal space mapping

A reciprocal space map is a loop scan where the scanning axis is ω-2θ and the incremental axis is ω. The data is collected in a square grid in reciprocal space and allows to distinguish between tilt and strain. In the hexagonal lattice, the reciprocal vectors can be expressed as:

$$\vec{a}* = 2\pi\frac{2}{\sqrt{3}a}\vec{a}$$
$$\vec{b}* = 2\pi\frac{2}{\sqrt{3}a}\vec{b} \tag{A.10}$$
$$\vec{c}* = \frac{2\pi}{c}\vec{c}$$

Symmetric ($h = k = 0$) X-ray diffraction can only determine lattice variations in the perpendicular direction of the sample surface. However, an asymmetric reciprocal space map gives information on both the in-plane and out-of-plane lattice constants. In the triple-axis geometry, the contributions of tilt and strain can be separated.

As an example, considering an asymmetric reciprocal map around the $11\bar{2}4$ reflection, the relative changes of the lattice parameters in ZnO can be obtained from:

$$\begin{aligned} \frac{l}{4} \times \left\| [0001]_{ZnO} \right\| &= \frac{2\pi}{c_{ZnO}} \\ \frac{h}{1} \times \left\| [11\bar{2}0]_{ZnO} \right\| &= \frac{2\pi}{a_{ZnO}} \end{aligned} \tag{A.11}$$

It is convenient to plot the $11\bar{2}4$ map against the coordinates of the deviation vector $\vec{Q}$. Any point on the map with coordinates (Q_y, Q_z) corresponds to a set of lattice parameters (a_{ZnO}, c_{ZnO}):

$$\begin{aligned} Q_y &= \frac{4\pi}{a_{ZnO}} \sqrt{\frac{2}{3}} \sqrt{h^2 + k^2} \\ Q_z &= \frac{2\pi}{c_{ZnO}} l \end{aligned} \tag{A.12}$$

Appendix B

Scattering theory in ZnO epitaxial films

In this section, we review the principal scattering mechanisms in n-type ZnO, express each mobility component in $cm^2/V\cdot s$ and generalize the equations to p-type ZnO.

B.1 Lattice scattering

The localized vibrations of the lattice in the presence of phonons create potential fluctuations that scatter free electrons. ZnO is an ionic II-VI semiconductor therefore Coulombic potential fluctuations result in polar optical phonon scattering. The corresponding mobility μ_{PO} can be expressed as:[226]

$$\mu_{PO}(T) = 10^4 \frac{4}{3E_o\sqrt{\pi}} \sqrt{\frac{2kT}{m_e^*}} [\exp(\frac{T_o}{T}) - 1] \quad \text{(B.1)}$$

where:

$$E_o = \frac{m_e^* ekT_o}{\varepsilon_o \hbar^2} \left(\frac{1}{\varepsilon_\infty} - \frac{1}{\varepsilon_s} \right) \quad \text{(B.2)}$$

Dilation or contraction of the lattice with temperature creates deformation potentials, resulting in acoustic phonon scattering. The corresponding mobility μ_{AC} is:[227]

$$\mu_{AC}(T) = 10^4 \frac{2^{2/3}\sqrt{\pi} e\hbar^4 \rho s^2}{3E_1^2 \sqrt{m_e^{*5}(kT)^3}} \quad \text{(B.3)}$$

Phonons can also scatter electrons through piezoelectric behavior since ZnO is a non-centrosymmetric semiconductor. The mobility for piezoelectric scattering μ_{PE} is:[228]

$$\mu_{PE}(T) = \frac{1.44\varepsilon_s}{P^2} \sqrt{\frac{300}{T}} \left(\frac{m_o}{m_e^*} \right)^{3/2} \quad \text{(B.4)}$$

B.2 Ionized impurity scattering

Carrier scattering by the long range Coulomb potentials created by charged impurities in the epilayer should be considered. The mobility component μ_{II} is:[229]

$$\mu_{II}(T) = 10^4 \frac{128\sqrt{2\pi}\varepsilon_o^2\varepsilon_s^2(kT)^{3/2}}{e^3\sqrt{m_e^*}(2N_A + n(T))} \times \frac{1}{\ln(1+y(n(T))) - \frac{y(n(T))}{1+y(n(T))}} \quad \text{(B.5)}$$

where:

$$y(n(T)) = \frac{24\varepsilon_o\varepsilon_s m_e^*(kT)^2}{e^2\hbar^2 n(T)} \quad \text{(B.6)}$$

B.3 Dislocation scattering

The mosaic structure formed by heteroepitaxial ZnO films epitaxially grown on sapphire contains edge-type dislocations. These dislocations create electric fields that scatter the free carriers. The corresponding mobility μ_{DIS} is given by:[230]

$$\mu_{DIS}(T) = 10^4 \frac{\hbar^3 c^2 n^2(T) e}{N_{DIS} m_e^{*2}(kT)^2}\left(1 + \frac{8\varepsilon_o\varepsilon_s m_e^*(kT)^2}{e^2 n(T)\hbar^2}\right)^{3/2} \quad \text{(B.7)}$$

B.4 Theoretical temperature dependence of the mobility

The total mobility is obtained by combining the various scattering mechanisms discussed above. According to Matthiessen's rule:

$$\frac{1}{\mu(T)} = \frac{1}{\mu_{PO}(T)} + \frac{1}{\mu_{AC}(T)} + \frac{1}{\mu_{PE}(T)} + \frac{1}{\mu_{II}(T)} + \frac{1}{\mu_{DIS}(T)} \quad \text{(B.8)}$$

The fitting parameters are the electron concentration $n(T)$, which is fitted by the charge balance equation, the acceptor level density N_A and the dislocation density N_{DIS}.

B.5 Hole mobility in *p*-type ZnO

The above equations hold for p-type samples modulo the following permutations:

$$n(T) \leftrightarrow p(T) \quad \text{(B.9)}$$

$$2N_A + n(T) \leftrightarrow 2N_D + p(T) \quad \text{(B.10)}$$

$$m_e^* \leftrightarrow m_h^* \quad \text{(B.11)}$$

Bibliography

[1] U.S. Department of Energy, "The promise of solid state lighting for general illumination", Conclusions and recommendations from OIDA technology roadmaps, 2001.

[2] J. A. Edmond, H. S. Kang and C. H. Carter Jr., "Blue LEDs, UV photodiodes and high-temperature rectifiers in 6H-SiC", *Physica B* **185**, 453 (1993).

[3] M. A. Haase, J. Qiu, J. M. Depuydt and H. Cheng, "Blue-green laser diodes", *Appl. Phys. Lett.* **59**, 1272 (1991).

[4] S. Nakamura, T. Mukai and M. Senoh, "High-power GaN *p-n* junction blue light emitting diodes", *Jpn. J. Appl. Phys.* **30**, L1998 (1991).

[5] T. Minami, "Transparent conducting oxide semiconductors for transparent electrodes", *Semicond. Sci. Technol.* **20**, S35 (2005).

[6] H. Morkoç, S. Strite, G. B. Bao, M. E. Lin, B. Sverdlov and M. Burns, "Large-band-gap SiC, III-V nitride, and II-VI ZnSe-based semiconductor device technologies", *J. Appl. Phys.* **76**, 1363 (1994).

[7] S. Nakamura, Y. Harada and M. Seno, "Novel metalorganic chemical vapor deposition system for GaN growth", *Appl. Phys. Lett.* **58**, 2021 (1991).

[8] H. Amano, N. Sawaki, I. Akasaki and Y. Toyoda, "Metalorganic vapor phase epitaxial growth of a high quality GaN film using an AlN buffer layer", *Appl. Phys. Lett.* **48**, 353 (1986).

[9] S. Nakamura, "GaN growth using GaN buffer layer", *Jpn. J. Appl. Phys.* **30**, L1705 (1991).

[10] K. C. Kim, M. C. Schmidt, H. Sato, F. Wu, N. Fellows, M. Saito, K. Fujito, J. S. Speck, S. Nakamura and S. P. DenBaars, "Improved electroluminescence on nonpolar *m*-plane InGaN/GaN quantum wells LEDs", *Phys. Status Solidi (RRL)* **1**, 125 (2007).

[11] S. Nakamura, T. Mukai, M. Senoh and N. Iwasa, "Thermal annealing effects on *p*-type Mg-doped GaN films", *Jpn. J. Appl. Phys.* **31**, L139 (1992).

[12] S. Nakamura, M. Senoh and T. Mukai, "P-GaN/N-InGaN/N-GaN double-

heterostructure blue-light-emitting diodes", *Jpn. J. Appl. Phys.* **32**, L8 (1993).

[13] M. W. Hodapp, "Applications for high-brightness light-emitting diodes", in *Semiconductor and semimetals*, (Volume 48, page 228, Academic Press, London, 1997).

[14] E. Monroy, F. Calle, C. Angulo, P. Vila, A. Sanz, J. A. Garrido, E. Calleja, E. Muñoz, S. Haffouz, B. Beaumont, F. Omnes and P. Gibart, "GaN-based solar-ultraviolet detection instrument", *Appl. Opt.* **37**, 5058 (1998).

[15] C. G. Granqvist, "Window coatings for the future", *Thin Solid Films* **193-194**, 730 (1990) and references therein.

[16] T. Minami, H. Nanto and S. Takata, "Highly conductive and transparent aluminum doped zinc oxide thin films prepared by RF magnetron sputtering", *Jpn. J. Appl. Phys.* **23**, L280 (1984).

[17] Y. R. Ryu, T. S. Lee, J. A. Lubguban, A. B. Corman, H. W. White, J. H. Leem, M. S. Han, Y. S. Park, C. J. Youn and W. J. Kim, "Wide-band gap oxide alloy: BeZnO", *Appl. Phys. Lett.* **88**, 052103 (2006).

[18] A. Ohtomo, M. Kawasaki, T. Koida, K. Masubuchi, H. Koinuma, Y. Sakurai, Y. Yoshida, T. Yasuda and Y. Segawa, "$Mg_xZn_{1-x}O$ as a II–VI widegap semiconductor alloy", *Appl. Phys. Lett.* **72**, 2466 (1998).

[19] T. Makino, Y. Segawa, M. Kawasaki, A. Ohtomo, R. Shiroki, K. Tamura, T. Yasuda and H. Koinuma, "Band gap engineering based on $Mg_xZn_{1-x}O$ and $Cd_yZn_{1-y}O$ ternary alloy films", *Appl. Phys. Lett.* **78**, 1237 (2001).

[20] D. M. Bagnall, Y. F. Chen, Z. Zhu, T. Yao, S. Koyama, M. Y. Shen and T. Goto, "Optically pumped lasing of ZnO at room temperature", *Appl. Phys. Lett.* **70**, 2230 (1997).

[21] Y. Segawa, A. Ohtomo, M. Kawasaki, H. Koinuma, Z. K. Tang, P. Yu and G. K. L. Wong, "Growth of ZnO thin film by laser MBE: lasing of exciton at room temperature", *Phys. Status Solidi B* **202**, 669 (1997).

[22] H. D. Li, S. F. Yu, A. P. Abiyasa, C. Yuen, S. P. Lau, H. Y. Yang and E. S. P. Leong, "Strain dependence of lasing mechanisms in ZnO epilayers", *Appl. Phys. Lett.* **86**, 261111 (2005).

[23] H. Cao, Y. G. Zhao, H. C. Ong, S. T. Ho, J. Y. Dai, J. Y. Wu and R. P. H. Chang, "Ultraviolet lasing in resonators formed by scattering in semiconductor polycrystalline films", *Appl. Phys. Lett.* **73**, 3656 (1998).

[24] A. Ohtomo, K. Tamura, M. Kawasaki, T. Makino, Y. Segawa, Z. K. Tang, G. Wong, Y. Matsumoto and H. Koinuma, "Room-temperature stimulated emission of excitons in ZnO/(Mg, Zn)O superlattices", *Appl. Phys. Lett.* **77**, 2204 (2000).

[25] M. H. Huang, S. Mao, H. Feick, H. Yan, Y. Wu, H. Kind, E. Weber, R. Russo and P. Yang, "Room-temperature ultraviolet nanowire nanolasers", *Science* **8**, 1897 (2001).

[26] L. M. Levinson and H. R. Philipp, "Zinc oxide varistors – A review", *Am. Ceram. Soc. Bull.* **65**, 639 (1986).

[27] J. D. Albrecht, P. P. Ruden, S. Limpijumnong, W. R. L. Lambrecht and K. F. Brennan, "High field electron transport properties of bulk ZnO", *J. Appl. Phys.* **86**, 6864 (1999).

[28] D. C. Look, D. C. Reynolds, J. R. Sizelove, R. L. Jones, C. W. Litton, G. Cantwell and W. C. Harsch, "Electrical properties of bulk ZnO", *Solid. State. Commun*. **105**, 399 (1998).

[29] D. C. Look, D. C. Reynolds, J. W. Hemsky, R. L. Jones and J. R. Sizelove, "Production and annealing of electron irradiation damage in ZnO", *Appl. Phys. Lett.* **75**, 811 (1999).

[30] A. Y. Polyakov, N. B. Smirnov, A. V. Govorkov, E. A. Kozhukhova, S. J. Pearton, D. P. Norton, A. Osinsky and A. Dabiran, "Electrical properties of undoped bulk ZnO substrates", *J. Electron. Mater.* **35**, 663 (2006).

[31] S. Graubner, C. Neumann, N. Volbers, B. K. Meyer, J. Bläsing and A. Krost, "Preparation of ZnO substrates for epitaxy: Structural, surface and electrical properties", *Appl. Phys. Lett.* **90**, 042103 (2007).

[32] H. J. Queisser and E. E. Haller, "Defects in Semiconductors: some fatal, some vital", *Science* **281**, 945 (1998).

[33] S. Limpijumnong, S. B. Zhang, S. H. Wei and C. H. Park, "Doping by large-size-mismatched impurities: The microscopic origin of arsenic- or antimony-doped *p*-type zinc oxide", *Phys. Rev. Lett.* **92**, 155504 (2004).

[34] R. D. Shannon and C. T. Prewitt, "Effective ionic radii in oxides and fluorides", *Acta. Cryst. B* **25**, 925 (1969).

[35] W. Hume Rothery and H. M. Powell, "On the theory of superlattice structures in alloys", *Z. Krist.* **91**, 23 (1935).

[36] S. B. Zhang, S. H. Wei and A. Zunger, "Intrinsic *n*-type versus *p*-type doping asymmetry and the defect physics of ZnO", *Phys. Rev. B* **63**, 075205 (2001).

[37] H. D. Jung, C. D. Song, S. Q. Wang, K. Arai, Y. H. Wu, Z. Zhu, T. Yao, H. Katayama-Yoshida, "Carrier concentration enhancement of *p*-type ZnSe and ZnS by codoping with active nitrogen and tellurium by using a δ-doping technique", *Appl. Phys. Lett.* **70**, 1143 (1997).

[38] Y. Kashiwaba, H. Kirita, H. Abe and T. Ikeda, "Fabrication of Cu-doped CdS cell by an all-evaporation process and its photovoltaic properties", *Jpn. J. Appl. Phys.* **29**, 1733 (1990).

[39] S. J. Pearton, F. Ren, A. P. Zhang and K. P. Lee, "Fabrication and performance of GaN electronic devices", *Mater. Sci. Eng. R* **30**, 55 (2000).

[40] C. Kilic, A. Zunger, "*n*-type doping of oxides by hydrogen", *Appl. Phys. Lett.* **81**, 73 (2002).

[41] I. W. Tao, M. Jurkovic and W. I. Wang, "Doping of ZnTe by molecular beam epitaxy", *Appl. Phys. Lett.* **64**, 1848 (1994).

[42] R. W. Birkmire and E. Eser, "Polycrystalline thin films solar cells: present status and future potential", *Ann. Rev. Mater. Sci.* **27**, 625 (1997).

[43] A. Zunger, "Practical doping principles", *Appl. Phys. Lett.* **83**, 57 (2003).

[44] G. F. Neumark, "Defects in wide band gap II-VI crystals", *Mater. Sci. Eng. R* **21**, 1 (1997).

[45] C. G. Van de Walle, D. B. Laks, G. F. Neumark and S. T. Pantelides, "First-principles calculations of solubilities and doping limits: Li, Na, and N in ZnSe", *Phys. Rev. B* **47**, 9425 (1993).

[46] T. Yamamoto and H. Katayama-Yoshida, "Solution using a codoping method to unipolarity for the fabrication of *p*-type ZnO", *Jpn. J. Appl. Phys.* **38**, L166 (1999).

[47] C. H. Park and D. J. Chadi, "Bulk lattice instability in II-VI semiconductors and its effects on impurity concentration", *Phys. Rev. Lett.* **75**, 1134 (1995).

[48] G. Mandel, "Self-compensation limited conductivity in binary semiconductors. I. Theory*", *Phys. Rev.* **134**, A1073 (1964).

[49] Y. Marfaing, "Fundamental studies on compensation mechanisms in II-VI compounds", *J. Cryst. Growth* **161**, 205 (1996).

[50] D. J. Chadi, "Predictor of *p*-type doping in II-VI semiconductors", *Phys. Rev. B* **59**, 15181 (1999).

[51] G. F. Neumark, "Achievement of well conducting wide-band-gap semiconductors, role of solubility and nonequilibrium impurity incorporation", *Phys. Rev. Lett.* **62**, 1800 (1989).

[52] S. B. Zhang, "The microscopic origin of the doping limits in semiconductors and wide-gap materials and recent developments in overcoming these limits: a review", *J. Phys.: Condens. Matter* **14**, R881 (2002).

[53] S. B. Zhang, S. H. Wei and A. Zunger, "A phenomenological model for systematization and prediction of doping limits in II–VI and I–III–VI_2 compounds", *J. Appl. Phys.* **83**, 3192 (1998).

[54] S. B. Zhang, S. H. Wei and A. Zunger, "Microscopic origin of the phenomenological equilibrium "doping limit rule" in *n*-type III-V semiconductors", *Phys. Rev. Lett.* **84**, 1232 (2000).

[55] J. M. Langer and H. Heinrich, "Deep-level impurities: a possible guide to prediction of band-edge discontinuities in semiconductor heterojunctions", *Phys. Rev. Lett.* **55**, 1414 (1985).

[56] W. Walukiewicz, "Intrinsic limitations to the doping of wide-gap semiconductors", *Physica B* **302-303**, 123 (2001).

[57] S. Lany, J. Osorio-Guillén and A. Zunger, "Origins of the doping asymmetry in oxides: hole doping in NiO versus electron doping in ZnO", *Phys. Rev. B* **75**, 241203 (2005).

[58] D. C. Look, G. C. Farlow, P. Reunchan, S. Limpijumnong, S. B. Zhang and K. Nordlund, "Evidence for native-defect donors in *n*-type ZnO", *Phys. Rev. Lett.* **95**, 225502 (2005).

[59] Y. V. Gorelkinskii and G. D. Watkins, "Defects produced in ZnO by 2.5-MeV electron irradiation at 4.2 K: Study by optical detection of electron paramagnetic resonance", *Phys. Rev. B* **69**, 115212 (2004).

[60] A. F. Kohan, G. Ceder, D. Morgan and C. G. Van de Walle, "First-principles study of native point defects in ZnO", *Phys. Rev. B* **61**, 15019 (2000).

[61] A. Janotti and C. G. Van de Walle, "Native point defects in ZnO", *Phys. Rev. B* **76**, 165202 (2007).

[62] J. Sann, J. Stehr, A. Hofstaetter, D. M. Hoffman, A. Neumann, M. Lerch, U. Haboeck, A. Hoffmann and C. Thomsen, "Zn interstitial related donors in ammonia-treated ZnO powders", *Phys. Rev. B* **76**, 195203 (2007).

[63] J. I. Pankove and N. M. Johnson, "Hydrogen in semiconductors", in *Semiconductors and Semimetals*, (Volume 34, Academic Press, 1991).

[64] C. G. Van de Walle, "Hydrogen as a cause of doping in zinc oxide", *Phys. Rev. Lett.* **85**, 1012 (2000).

[65] S. J. Jokela and M. D. McCluskey, "Structure and stability of O-H donors in ZnO from high-pressure and infrared spectroscopy", *Phys. Rev. B* **72**, 113201 (2005).

[66] F. A. Selim, M. H. Weber, D. Solodovnikov and K. G. Lynn, "Nature of native defects in ZnO", *Phys. Rev. Lett.* **99**, 085502 (2007).

[67] H. Takenaka and D. J. Singh, "Bonding of H in O vacancies of ZnO: Density functional calculations", *Phys. Rev. B* **75**, 241102 (2007).

[68] X. Li, B. Keyes, S. Asher, S. B. Zhang, S. H. Wei, T. J. Coutts, S. Limpijumnong and C. G. Van de Walle, "Hydrogen passivation effect in nitrogen-doped ZnO thin films", *Appl. Phys. Lett.* **86**, 122107 (2005).

[69] K. Minegishi, Y. Koiwai. Y. Kikuchi, K. Yano, M. Kasuga and A. Shimizu, "Growth of *p*-type zinc oxide films by chemical vapor deposition, *Jpn. J. Appl. Phys.* **36**, L1453 (1997).

[70] B. K. Meyer, H. Alves, D. M. Hoffman, W. Kriegseis, D. Forster, F. Bertram, J. Christen, A. Hoffman, M. Strassburg, M. Dworzak, U. Haboeck and A. V. Rodina, "Bound exciton and donor-acceptor pair recombinations in ZnO", *Phys. Status Solidi B* **241**, 231 (2004).

[71] A. Tsukazaki, A. Ohtomo and M. Kawasaki, "High-mobility electronic transport in ZnO thin films", *Appl. Phys. Lett.* **88**, 152106 (2006).

[72] T. Makino, Y. Segawa, S. Yoshida, A. Tsukazaki, A. Ohtomo and M. Kawasaki, "Gallium concentration dependence of room-temperature near-band-edge luminescence in *n*-type ZnO:Ga", *Appl. Phys. Lett.* **85**, 759 (2004).

[73] A. Tsukazaki, A. Ohtomo, T. Onuma, M. Ohtani, T. Makino, M. Sumiya, K. Ohtani, S. F. Chichibu, S. Fuke, Y. Segawa, H. Ohno. H. Koinuma and M. Kawasaki, "Repeated temperature modulation epitaxy for *p*-type doping and light-emitting diode based on ZnO", *Nat. Mater.* **4**, 42 (2005).

[74] Y. R. Ryu, T. S. Lee, J. A. Lugbugan, H. W. White, B. J. Kim, Y. S. Park and C. J. Youn, "Next generation of oxide photonic devices: ZnO-based ultraviolet light emitting diodes", *Appl. Phys. Lett.* **88**, 241108 (2006).

[75] F. Oba, S. R. Nishitani, S. Isotani, H. Adachi and I. Tanaka, "Energetics of native defects in ZnO", *J. Appl. Phys.* **90**, 824 (2001).

[76] F. Tuomisto, V. Ranki, K. Saarinen and D. C. Look, "Evidence of the Zn vacancy acting as the dominant acceptor in *n*-type ZnO", *Phys. Rev. Lett.* **20**, 205502-1 (2003).

[77] C. H. Park, S. B. Zhang and S. H. Wei, "Origin of *p*-type doping difficulty in ZnO: The impurity perspective", *Phys. Rev. B* **66**, 073202 (2002).

[78] D. C. Look, D. C. Reynolds, C. W. Litton, R. L. Jones, D. B. Eason and G. Cantwell, “Characterization of homoepitaxial *p*-type ZnO grown by molecular beam epitaxy”, *Appl. Phys. Lett.* **81**, 1830 (2002).

[79] S. Graubner, C. Neumann, N. Volbers, B. K. Meyer, J. Bläsing and A. Krost, “Preparation of ZnO substrates for epitaxy: structural, surface and electrical properties”, *Appl. Phys. Lett.* **90**, 042103 (2007).

[80] A. Kobayashi, O. F. Sankey and J. D. Dow, “Deep energy levels of defects in the wurtzite semiconductors AlN, CdS, CdSe, ZnS, and ZnO”, *Phys. Rev. B* **28**, 946 (1983).

[81] X. Li, Y. Yan, T. A. Gessert, C. Dehart, C. L. Perkins, D. Young and T. J. Coutts, “*p*-type ZnO thin films formed by CVD reaction of diethylzinc and NO gas”, *Electrochem. Solid State Lett.* **6**, C56 (2003).

[82] A. Dadgar, N. Oleynik, J. Bläsing, S. Deiter, D. Forster, F. Bertram, A. Diez, M. Seip, A. Greiling, J. Christen and A. Krost, “Heteroepitaxy and nitrogen doping of high-quality ZnO”, *J. Cryst. Growth* **272**, 800 (2004).

[83] E. C. Lee, Y. S. Kim, Y. G. Jin and K. J. Chang, “Compensation mechanism for N acceptors in ZnO”, *Phys. Rev. B* **64**, 085120 (2001).

[84] B. Claflin, D. C. Look, S. J. Park and G. Cantwell, “Persistent *n*-type photoconductivity in *p*-type ZnO”, *J. Cryst. Growth* **287**, 16 (2006).

[85] Y. W. Heo, Y. W. Kwon, Y. Li, S. J. Pearton and D. P. Norton, “*p*-type behavior in phosphorus-doped (Zn,Mg)O device structures”, *Appl. Phys. Lett.* **84**, 3474 (2004).

[86] K. K. Kim, H. S. Kim, D. K. Hwang, J. H. Lim and S. J. Park, “Realization of *p*-type ZnO thin films via phosphorus doping and thermal activation of the dopant”, *Appl. Phys. Lett.* **83**, 63 (2003).

[87] F. X. Xiu, Z. Yang, L. J. Mandalapu, J. L. Liu and W. P. Beyermann, “*p*-type ZnO films with solid-source phosphorus doping by molecular-beam epitaxy”, *Appl. Phys. Lett.* **88**, 052106 (2006).

[88] Y. R. Ryu, T. S. Lee and H. W. White, “Properties of arsenic-doped *p*-type ZnO grown by hybrid beam deposition”, *Appl. Phys. Lett.* **83**, 87 (2003).

[89] D. C. Look, G. M. Renlund, R. H. Burgener II and J. R. Sizelove, “As-doped *p*-type ZnO produced by an evaporation/sputtering process”, *Appl. Phys. Lett.* **85**, 5269 (2004).

[90] F. X. Xiu. Z. Yang, L. J. Mandalapu, D. T. Zhao and J. L. Liu, “High-mobility Sb-doped *p*-type ZnO by molecular-beam epitaxy”, *Appl. Phys. Lett.* **87**, 152101 (2005).

[91] W. J. Lee, J. Kang and K. J. Chang, "Defect properties and *p*-type doping efficiency in phosphorus-doped ZnO", *Phys. Rev. B* **73**, 024117 (2006).

[92] U. Wahl, E. Rita, J. G. Correia, A. C. Marques, E. Alves and J. C. Soares, "Direct evidence for As as a Zn-site impurity in ZnO", *Phys. Rev. Lett.* **95**, 215503 (2006).

[93] S. D. Lester, F. A. Ponce, M. G. Craford and D. A. Steigerwald, "High-dislocation densities in high efficiency GaN-based light-emitting diodes", *Appl. Phys. Lett.* **66**, 1249 (1995).

[94] H. M. Ng, D. Doppalapudi, T. D. Moustakas, N. G. Weimann and L. F. Eastman, "The role of dislocation scattering in *n*-type GaN films", *Appl. Phys. Lett.* **73**, 821 (1998).

[95] J. W. P. Hsu, M. J. Manfra, D. V. Lang, S. Richter, S. N. G. Chu, A. M. Sergent, R. N. Kleiman, L. N. Pfeiffer, R. J. Molnar, "Inhomogeneous spatial distribution of reverse bias leakage in GaN Schottky diodes", *Appl. Phys. Lett.* **78**, 1685 (2001).

[96] P. J. Dean, "Comparison of MOCVD-grown with conventional II-VI materials parameters for EL thin films", *Phys. Status Solidi A* **81**, 625 (1984).

[97] S. Fujii, T. Terada, Y. Fujita and T. Iuchi, "New deep-level photoluminescence bands of homoepitaxial CdTe films grown by metalorganic chemical vapor deposition, *Jpn. J. Appl. Phys.* **28**, L1712 (1989).

[98] A. Naumov, K. Walf, T. Reisinger, H. Stanzl and W. Gebhardt, "Luminescence due to lattice-mismatch defects in ZnTe layers grown by metalorganic vapor phase epitaxv", *J. Appl. Phys.* **73**, 2581 (1998).

[99] M. A. Reshchikov and H. Morkoç, "Luminescence properties of defects in GaN", *J. Appl. Phys.* **97**, 061301 (2005).

[100] G. Salviati, M. Albrecht, C. Zanotti-Fregonara, N. Armani, M. Mayer, Y. Shreter, M. Guzzi, Y. V. Melnik, K. Vassilevski, V. A. Dmitriev and H. P. Strunk, "Cathodoluminescence and transmission electron microscopy study of the influence of crystal defects on optical transitions in GaN", *Phys. Status Solidi A* **171**, 325 (1999).

[101] Y. G. Shreter, Y. T. Rebane, T. J. Davis, J. Barnard, M. Darbyshire, J. W. Steeds, W. G. Perry, M. D. Bremser and R. F. Davis, "Dislocation luminescence in wurtzite GaN", *Mater. Res. Soc. Symp. Proc.* **449**, 683 (1997).

[102] P. J. Schuck, M. D. Mason, R. D. Grober, O. Ambacher, A. P. Lima, C. Miskys, R. Dimitrov and M. Stutzmann, "Spatially resolved photoluminescence of inversion domain boundaries in GaN-based lateral polarity heterostructures", *Appl. Phys. Lett.* **79**, 952 (2001).

[103] M. A. Reshchikov, D. Huang, F. Yun, P. Visconti, L. He, H. Morkoç, J. Jasinski, Z. Liliental-Weber, R. J. Molnar, S. S. Park and K. Y. Lee, "Unusual luminescence lines in GaN", *J. Appl. Phys.* **94**, 5623 (2003).

[104] V. Swaminathan and A. S. Jordan, "Dislocations in III/V compounds", in *Semiconductors and Semimetals*, (Volume 38, Academic Press, 1993, page 324).

[105] M. Ettenberg, "Effects of dislocation density on the properties of liquid phase epitaxial GaAs", *J. Appl. Phys.* **45**, 901 (1974).

[106] J. D. Weeks, J. C. Tully and L. C. Kimerling, "Theory of recombination-enhanced defect reactions in semiconductors", *Phys. Rev. B* **12**, 3286 (1975).

[107] P. M. Petroff, O. G. Lorimor and J. M. Ralston, "Defect structure induced during forward-bias degradation of GaP green-light-emitting diodes", *J. Appl. Phys.* **47**, 1583 (1976).

[108] S. Guha, J. M. Depuydt, M. A. Haase, J. Qiu and H. Cheng, "Degradation of II-VI based blue green light emitters", *Appl. Phys. Lett.* **63**, 3107 (1993).

[109] L. Sugiura, "Dislocation motion in GaN light-emitting devices and its effects on device lifetime", *J. Appl. Phys.* **81**, 1633 (1997).

[110] R. W. G. Wyckoff, *Crystal structures*, Volume 1, (John Wiley & Sons, New York, London, 1963).

[111] M. Sumiya, K. Yoshimura, K. Ohtsuka and S. Fuke, "Dependence of impurity incorporation on the polar direction of GaN film growth", *Appl. Phys. Lett.* **76**, 2098 (2000).

[112] D. A. Porter and K. E. Easterling, *Phase Transformation in metals and alloys, second edition*, (Nelson Thornes, 1992, page 143).

[113] T. Matsuoka, N. Yoshimoto, T. Sasaki and A. Katsui, "Wide-gap semiconductor InGaN and InGaAlN grown by MOVPE", *J. Electron. Mater.* **21**, 157 (1992).

[114] A. Ohtomo, K. Tamura, K. Saikusa, K. Takahashi, T. Makino and Y .Segawa, "Single crystalline ZnO films grown on lattice-matched $ScAlMgO_4$ (0001) substrates", *Appl. Phys. Lett.* **75**, 2635 (1999).

[115] A. Tsukazaki, A. Ohtomo, M. Kawasaki, T. Makino, C. H. Chia, Y. Segawa and H. Koinuma, "Emission from the higher-order excitons in ZnO films grown by laser molecular-beam epitaxy", *Appl. Phys. Lett.* **84**, 3858 (2004).

[116] Y. Ogo, K. Nomura, H. Yanagi, H. Ohta, T. Kamiya, M. Hirano and H. Hosono, "Growth and structure of heteroepitaxial thin films of homologous compounds

$RAO_3(MO)_m$ by reactive solid-phase epitaxy: Applicability to a variety of materials and epitaxial template layers", *Thin solid films* **496**, 64 (2006).

[117] M. W. Cho, A. Setiawan, H. J. Ko, S. K. Hong and T. Yao, "ZnO epitaxial layers grown on c-sapphire substrate with MgO buffer by plasma-assisted molecular beam epitaxy (P-MBE)", *Semicond. Sci. Technol.* **20**, S13 (2005).

[118] X. L. Du, M. Murakami, H. Iwaki and A. Yoshikawa, "Complete elimination of multi-angle rotation domains in ZnO epilayers grown on (0001) sapphire substrates", *Phys. Status Solidi A* **192**, 183 (2002).

[119] M. Ying, X. Du, Z. Mei, Z. Zeng, H. Zheng, Y. Wang, J. Jia, Z. Zhang and Q. Xue, "Effect of sapphire substrate nitridation on the elimination of rotation domains in ZnO epitaxial films", *J. Phys. D: Appl. Phys.* **37**, 3058 (2004).

[120] X. Du, M. Murakami, H. Iwaki, Y. Ishitani and A. Yoshikawa, "Effects of sapphire (0001) surface modification by gallium pre-exposure on the growth of high-quality epitaxial ZnO film", *Jpn. J. Appl. Phys.* **41**, L1043 (2002).

[121] A. B. M. Almamum Ashrafi, B. P. Zhang, N. T. Binh, K. Wakatsuki and Y. Segawa, "High-quality ZnO layers grown on 6H-SiC substrates by metalorganic chemical vapor deposition", *Jpn. J. Appl. Phys.* **3**, 1114 (2004).

[122] J. Zou, S. Zhou, C. Xia, Y. Hang, J. Xu, S. Gu and R. Zhang, "Structural, optical and electrical properties of ZnO films grown on *c*-plane sapphire and (100)γ-$LiAlO_2$ by pulsed laser deposition", *J. Crystal Growth* **280**, 185 (2005).

[123] K. Matsubara, P. Fons, A. Yamada, M. Watanabe, S. Niki, "Epitaxial growth of ZnO thin films on $LiNbO_3$ substrates", *Thin Solid Films* **347**, (1999) 238.

[124] X. H. Wu, L. M. Brown, D. Kapolnek, S. Keller, B. Keller, S. P. DenBaars and J. S. Speck, "Defect structure of metal-organic chemical vapor deposition-grown epitaxial (0001) GaN/Al_2O_3", *J. Appl. Phys.* **80**, 3228 (1996).

[125] D. Hull and D. J. Bacon, *Introduction to dislocations, fourth edition*, (Butterworth Heinemann, 2001, page 102).

[126] C. Stampfl and C. G. Van de Walle, "Energetics and electronic structure of stacking faults in AlN, GaN and InN", *Phys. Rev. B* **57**, R15052 (1998).

[127] Y. Yan, G. M. Dalpian, M. M. Al-Jassim and S. H. Wei, "Energetics and electronic structure of stacking faults in ZnO", *Phys. Rev. B* **70**, 193206 (2004).

[128] R. K. Singh and J. Narayan, "Pulsed-laser evaporation technique for deposition of thin films: Physics and theoretical model", *Phys. Rev. B* **41**, 8843 (1990).

[129] D. B. Chrisey and G. K. Hubler, *Pulsed Laser Deposition of Thin Films*, (John Wiley and Sons, New York, 1994).

[130] P. P. Pronko, S. K. Dutta, D. Du and R. K. Singh, "Thermophysical effects in laser processing of materials with picosecond and femtosecond pulses", *J. Appl. Phys.* **78**, 6233 (1995).

[131] ZnO wafer specification sheet, Cermet, available at *www.cermetinc.com*.

[132] O. Madelung, U. Rössler and M. Schulz, "Zinc oxide (ZnO) optical properties and spectra", in II-VI and I-VII Compounds; Semimagnetic Compounds, Volume 41B, pages 1-18, Springer-Verlag, Berlin, 1995.

[133] P. Mukherjee, S. Chen, J. B. Cuff, P. Sakthivel and S. Witanachchi, "Evidence for the physical basis and universality of the elimination of particulates using dual-laser ablation. I. Dynamic time-resolved target melt studies, and film growth of Y_2O_3 and ZnO", *J. Appl. Phys.* **91**, 1828 (2002).

[134] J. Perrière, E. Millon, W. Seiler, C. Boulmer-Leborgne, V. Craciun, O. Albert, J. C. Loulergue and J. Etchepare, "Comparison between ZnO films grown by femtosecond and nanosecond laser ablation", *J. Appl. Phys.* **91**, 690 (2002).

[135] J. E. Dominguez, Ph.D. Thesis, University of Michigan, 2003.

[136] M. J. Reason, Ph.D Thesis, University of Michigan, 2006.

[137] G. K. Williamson and W. H. Hall, "X-ray line broadening from filed aluminium and wolfram", *Acta Metall.* **1**, 22 (1953).

[138] V. Srikant, J. S. Speck and D. R. Clarke, "Mosaic structure in epitaxial films having large lattice mismatch", *J. Appl. Phys.* **82**, 4286 (1997).

[139] H. Sun, Ph.D. Thesis, University of Michigan, 2005.

[140] L. C. Feldman and J. W. Mayer, *Fundamentals of surface and thin film analysis*, (North-Holland, 1986).

[141] J. I. Pankove and N. M. Johnson, "Hydrogen in semiconductors", in *Semiconductors and semimetals*, (Volume 34, Academic Press, New York, 1991).

[142] P. D. T. Huibers and D. O. Shah, "Multispectral determination of soap film thickness", *Langmuir* **13**, 5995 (1997).

[143] Ü. Özgür, Y. I. Alivov, C. Liu, A. Teke, M. A. Reshchikov, S. Dogan, V. Avrutin, S. J. Cho and H. Morkoç, "A comprehensive review of ZnO materials and devices", *J. Appl. Phys.* **98**, 041301 (2005).

[144] S. Perkowitz, *Optical characterization of semiconductors; infrared, Raman and photoluminescence spectroscopy*, (Academic Press, 1991).

[145] P. T. Landsberg, *Recombination in semiconductors*, (Cambridge University Press, 1991).

[146] G. H. Wannier, "The structure of electronic excitation levels in insulating crystals", *Phys. Rev.* **52**, 191 (1937).

[147] G. Coli and K. K. Bajaj. "Excitonic transitions in ZnO/MgZnO quantum well heterostructures", *Appl. Phys. Lett.* **78**, 2861 (2001).

[148] H. Barry Bebb and E. W. Williams, "Photoluminescence I: Theory", in *Semiconductors and Semimetals*, (Volume 8, Academic Press, 1972).

[149] C. F. Klingshirn, *Semiconductor optics*, (Springer, Berlin, 1995).

[150] J. R. Haynes, "Experimental proof of the existence of a new excitonic complex in silicon", *Phys. Rev. Lett.* **4**, 361 (1960).

[151] J. Gutowski, N. Presser and I. Broser, "Acceptor-exciton complexes in ZnO: A comprehensive analysis of their electronic states by high-resolution magnetooptics and excitation spectroscopy", *Phys. Rev. B* **38**, 9746 (1988).

[152] K. Thonke, T. Gruber, N. Teofilov, R. Schönfelder, A. Waag and R. Sauer, "Donor-acceptor pair transitions in ZnO substrate material", *Physica B* **308-310**, 945 (2001).

[153] K. Tamura, T. Makino, A. Tsukazaki, M. Sumiya, S. Fuke, T. Furumochi, M. Lippmaa, C. H. Chia, Y. Segawa, H. Koinuma and M. Kawasaki, "Donor-acceptor pair luminescence in nitrogen-doped ZnO films grown on lattice-matched $ScAlMgO_4$ (0001) substrates", *Solid State Commun.* **127**, 265 (2003).

[154] A. Zeuner, H. Alves, D. M. Hofmann, B. K. Meyer, A. Hoffmann, U. Haboeck, M. Strassburg and M. Dworzak, "Structural and optical properties of epitaxial and bulk ZnO", *Phys. Status Solidi B* **234**, R7 (2002).

[155] L. Wang and N. C. Giles, "Determination of the ionization energy of nitrogen acceptors in zinc oxide using photoluminescence spectroscopy", *Appl. Phys. Lett.* **84**, 3049 (2004).

[156] D. C. Reynolds, D. C. Look, B. Jogai and R. J. Molnar, "Evidence for shallow acceptors in GaN", *J. Appl. Phys.* **89**, 6272 (2001).

[157] K. Huang and A. Rhys, "Theory of light absorption and non radiative transitions in F centres", *Proc. Roy. Soc. (London)* **A204**, 406 (1950).

[158] J. J. Hopfield, "A theory of edge-emission phenomena in CdS, ZnS and ZnO", *J. Phys. Chem. Solids* **10**, 110 (1959).

[159] J. J. Hopfield, D. G. Thomas and M. Gershenzon, "Pair spectra in GaP", *Phys. Rev. Lett.* **10**, 162 (1963).

[160] Y. P. Varshni, "Temperature dependence of the energy gap in semiconductors", *Physica* **34**, 149 (1967).

[161] Y. S. Jung, W. K. Choi, O. V. Kononenko and G. N. Panin, "Luminescence of bound excitons in epitaxial ZnO thin films grown by plasma-assisted molecular beam epitaxy", *J. Appl. Phys.* **99**, 013502 (2006).

[162] A. Manoogian and J. C. Wooley, "Temperature dependence of the energy-gap in semiconductors", *Can. J. Phys* **62**, 285 (1984).

[163] T. Schmidt, "Excitation-power dependence of the near-band-edge photoluminescence of semiconductors", *Phys. Rev. B* **45**, 8989 (1992) and references therein.

[164] M. A. Reshchikov and R. Y. Korotkov, "Analysis of the temperature and excitation intensity dependencies of photoluminescence in undoped GaN films", *Phys. Rev. B* **64**, 115205 (2001).

[165] L. J. Van der Pauw, "A method of measuring specific resistivity and Hall effect of discs of arbitrary shape", *Phillips Research Reports* **13**, 1 (1958).

[166] L. J. Van der Pauw, "A method of measuring the resistivity and Hall coefficient on lamellae of arbitrary shape", *Phillips Technical Review* **20**, 220 (1958).

[167] R. Chwang, B. J. Smith and C. R. Crowell, "Contact size effects on the van der Pauw method for resistivity and Hall coefficient measurement", *Solid. State. Electron.* **17**, 1217 (1974).

[168] E. H. Putley, *The Hall effect and related phenomena*, (Butterworth & Co, 1960).

[169] D. C. Look, *Electrical characterization of GaAs materials and devices*, (John Wiley and Sons, New York, 1989).

[170] D. A. Anderson and N. Apsley, "The Hall effect in III-V semiconductor assessment", *Semicond. Sci. Technol.* **1**, 187 (1986).

[171] H. Matsui, H. Saeki, T. Kawai, H. Tabata, B. Mizobuchi, "N doping using N_2O and NO sources: From the viewpoint of ZnO", *J. Appl. Phys.* **95**, 5882 (2004).

[172] N. Y. Garces, L. Wang, N. C. Giles, L. E. Halliburton, G. Cantwell and D. B. Eason, “Molecular nitrogen (N_2^-) acceptors and isolated nitrogen (N^-) acceptors in ZnO crystals”, *J. Appl. Phys.* **94**, 519 (2003).

[173] B. S. Li, Y. C. Liu, Z. Z. Zhi, D. Z. Shen, Y. M. Lu, J. Y. Zhang, X. W. Fan, R. X. Mu and D. O. Henderson, “Optical properties and electrical characterization of *p*-type ZnO thin films prepared by thermally oxidizing Zn_3N_2 thin films”, *J. Mater. Res.* **18**, 8 (2003).

[174] A. Allenic, W. Guo, Y. B. Chen, G. Y. Zhao, X. Q. Pan, Y. Che, Z. D. Hu and B. Liu, “Synthesis and properties of *p*-type nitrogen doped ZnO thin films by pulsed laser ablation of a Zn-rich Zn_3N_2 target”, *J. Mater. Res.* **10**, 2339 (2007).

[175] M. Sumiya, S. Fuke, A. Tsukazaki, K. Tamura, A. Ohtomo, M. Kawasaki and H. Koinuma, “Quantitative control and detection of heterovalent impurities in ZnO thin films grown by pulsed laser deposition”, *J. Appl. Phys.* **93**, 2562 (2003).

[176] L. M. Kukreja, A. Rohlfing, P. Misra, F. Hillenkamp and K. Dreisewerd, “Cluster formation in UV laser ablation plumes of ZnSe and ZnO studied by time-of-flight mass spectrometry”, *Appl. Phys. A* **78**, 641 (2004).

[177] C. L. Perkins, S. H. Lee, X. Li, S. E. Asher and T. J. Coutts, “Identification of nitrogen chemical states in N-doped ZnO via x-ray photoelectron spectroscopy”, *J. Appl. Phys.* **97**, 034907 (2005).

[178] R. L. Petritz, “Theory of photoconductivity in semiconductor films”, *Phys. Rev.* **104**, 1508 (1956).

[179] K. Tamura, T. Makino, A. Tsukazaki, M. Sumiya, S. Fuke, T. Furumochi, M. Lippmaa, C. H. Chia, Y. Segawa, H. Koinuma and M. Kawasaki, “Donor-acceptor pair luminescence in nitrogen-doped ZnO films grown on lattice-matched $ScAlMgO_4$ (0001) substrates”, *Solid State Commun.* **127**, 265 (2003).

[180] A. Zeuner, H. Alves, D. M. Hofmann, B. K. Meyer, A. Hoffmann, U. Haboeck, M. Strassburg and M. Dworzak, “Structural and optical properties of epitaxial and bulk ZnO”, *Phys. Status Solidi B* **234**, R7 (2002).

[181] B. K. Meyer, N. Volbers, A. Zeuner, S. Lautenschläger, J. Sann, A. Hoffmann and U. Haboeck, “Group I elements in ZnO”, *Mater. Res. Soc. Symp. Proc.* Vol. **891**, EE10-24 (2006).

[182] A. Allenic, Y. B. Chen, X. Q. Pan, Y. Che, Z. D. Hu and B. Liu, “Violet luminescence in phosphorus-doped ZnO epitaxial films”, *Appl. Phys. Lett.* **92**, 022107 (2008).

[183] E. Kaminska, A. Piotrowska, J. Kossut, A. Barcz, R. Butkute, W. Dobrowolski, E. Dynowska, R. Jakiela, E. Przezdziecka, R. Lukasiewicz, M. Aleszkiewicz, P. Wojnar, E. Kowalczyk, "Transparent *p*-type ZnO films obtained by oxidation of sputter-deposited Zn_3N_2", *Solid State Commun.* **135**, 11 (2005).

[184] C. Wang, Z. Ji, K. Liu, Y. Xiang, Z. Ye," *p*-type ZnO thin films prepared by oxidation of Zn_3N_2 thin films deposited by DC magnetron sputtering", *J. Cryst. Growth* **259**, 279 (2003).

[185] Y. W. Heo, S. J. Park, K. Ip, S. J. Pearton and D. P. Norton, "Transport properties of phosphorus-doped ZnO thin films", *Appl. Phys. Lett.* **83**, 1128 (2003).

[186] H. Von Wenckstern, G. Benndorf, S. Heitsch, J. Sann, M. Brandt, H. Schmidt, J. Lenzner, M. Lorenz, A. Y. Kuznetsov, B. K. Meyer and M. Grundmann, "Properties of phosphorus doped ZnO", *Appl. Phys. A* **88**, 125 (2007).

[187] H. Tampo, H. Shibata, P. Fons, A. Yamada, K. Matsubara, K. Iwata, K. Tamura, H. Takasu and S. Niki, "The effects of thermal treatments on the electrical properties of phosphorus doped ZnO layers grown by MBE", *J. Cryst. Growth* **278**, 268 (2005).

[188] J. H. Yang, H. S. Kim, J. H. Lim, D. K. Hwang, J. Y. Oh and S. J. Park, "The effect of Ar/O_2 sputtering gas on the phosphorus-doped *p*-type ZnO thin films", *J. Electrochem. Soc.* **153**, G242 (2006).

[189] F. X. Xiu, Z. Yang, L. J. Mandalapu and J. L. Liu, "Donor and acceptor competitions in phosphorus-doped ZnO", *Appl. Phys. Lett.* **88**, 152116 (2006).

[190] F. A. Ponce, D. P. Bour, W. Götz and P. J. Wright, "Spatial distribution of the luminescence in GaN thin films", *Appl. Phys. Lett.* **68**, 57 (1997).

[191] D. C. Look and J. R. Sizelove, "Dislocation scattering in GaN", *Phys. Rev. Lett.* **82**, 1237 (1999).

[192] Y. W. Heo, K. Ip, S. J. Park, S. J. Pearton, D. P. Norton, "Shallow donor formation in phosphorus-doped ZnO thin films", *Appl. Phys. A* **78**, 53 (2004).

[193] C. G. Dunn and E. F. Koch, "Comparison of dislocation densities of primary and secondary recrystallization grains on Si-Fe", *Acta Metall.* **1**, 548 (1957).

[194] H. P. Sun, X. Q. Pan, X. L. Du, Z. X. Mei, Z. Q. Zeng and Q. K. Xue, "Microstructure and crystal defects in epitaxial ZnO film grown on Ga modified (0001) sapphire surface", *Appl. Phys. Lett.* **85**, 4385 (2004).

[195] D. Gerthsen, D. Livitnov, Th. Gruber, C. Kirchner and A. Waag, "Origin and consequences of a high stacking fault density in epitaxial ZnO layers", *Appl. Phys. Lett.* **81**, 3972 (2002).

[196] A. Allenic, W. Guo, Y. B. Chen, M. B. Katz, G. Y. Zhao, Y. Che, Z. D. Hu, B. Liu and X. Q. Pan, "Amphoteric phosphorus doping for stable *p*-type ZnO", *Adv. Mater.* **19**, 3333 (2007).

[197] D. K. Bowen and B. K. Tanner, *High resolution X-ray diffractometry and topography*, (Taylor and Francis, London, 1990).

[198] A. Allenic, W. Guo, Y. B. Chen, Y. Che, Z. D. Hu, B. Liu and X. Q. Pan, "Microstructures and electrical properties of *p*-type phosphorus-doped ZnO films epitaxially grown on sapphire and ZnO substrates", *J. Phys. D: Appl. Phys*. **41**, 025103 (2008).

[199] B. J. Kwon, H. S. Kwack, S. K. Lee, Y. H. Cho, D. K. Hwang and S. J. Park, "Optical investigation of *p*-type ZnO epilayers doped with different phosphorus concentrations by radio-frequency magnetron sputtering", *Appl. Phys. Lett.* **91**, 061903 (2007).

[200] M. Germain, E. Kartheuser, A. L. Gurskii, E. V. Lutsenko, I. P. Marko, V. N. Pavlovskii, G. P. Yablonskii, K. Heime, M. Heuken and B. Schineller, "Effects of electron–phonon interaction and chemical shift on near-band-edge recombination in GaN", *J. Appl. Phys.* **91**, 9827 (2002).

[201] B. Lin, Z. Fu and Y. Jia, "Green luminescent center in undoped zinc oxide films deposited on silicon substrates", *Appl. Phys. Lett.* **79**, 943 (2001).

[202] P. Erhart and K. Abe, "Diffusion of zinc vacancies and interstitials in zinc oxide", *Appl. Phys. Lett.* **88**, 201918 (2006).

[203] H. Ohta, K. Kawamura, M. Orita, M. Hirano, N. Sarukura and H. Hosono, "Current injection emission from a transparent *p-n* junction composed of *p*-$SrCu_2O_2$/*n*-ZnO", *Appl. Phys. Lett.* **77**, 475 (2000).

[204] H. Hosono, H. Ohta, K. Hayashi, M. Orita and M. Hirano, "Near-UV emitting diodes based on a transparent *p-n* junction composed of heteroepitaxially grown *p*-$SrCu_2O_2$ and *n*-ZnO", *J. Crystal Growth* **237-239**, 496 (2002).

[205] H. Ohta, M. Kamiya, T. Kamiya, M. Hirano and H. Hosono, "UV-detector based on pn-heterojunction diode composed of transparent oxide semiconductors", *p*-NiO/*n*-ZnO, *Thin Solid Films* **445**, 317 (2003).

[206] H. Ohta, H. Mizoguchi, M. Hirano, S. Narushima, T. Kamiya and H. Hosono", "Fabrication and characterization of heteroepitaxial *p-n* junction diode composed of wide-gap oxide semiconductors *p*-$ZnRh_2O_4$/*n*-ZnO, *Appl. Phys. Lett.* **82**, 823 (2003).

[207] H. Ohta, M. Hirano, K. Nakahara, H. Maruta, T. Tanabe, M. Kamiya, T. Kamiya and H. Hosono, "Fabrication and photoresponse of a *pn*-heterojunction diode composed of transparent oxide semiconductors, *p*-NiO and *n*-ZnO", *Appl. Phys. Lett.* **83**, 1029 (2003).

[208] Y. S. Choi, J. Y. Lee, S. Im and S. J. Lee, "Photoresponse characteristics of *n*-ZnO/*p*-Si heterojunction photodiodes", *J. Vac. Sci. Technol.* B **20**, 2384 (2002).

[209] J. Y. Lee, Y. S. Choi, W. H. Choi, H. W. Yeom, Y. K. Yoon, J. H. Kim and S. Im, "Characterization of films and interfaces in *n*-ZnO/*p*-Si photodiodes", *Thin Solid Films* **420-421**, 112 (2002).

[210] I. S. Jeong, J. H. Kim and S. Im, "Ultraviolet-enhanced photodiode employing *n*-ZnO/*p*-Si structure, *Appl. Phys. Lett.* **83**, 2946 (2003).

[211] C. H. Park, I. S. Jeong, J. H. Kim and S. Im, "Spectral responsivity and quantum efficiency of *n*-ZnO/*p*-Si photodiode fully isolated by ion-beam treatment", *Appl. Phys. Lett.* **82**, 3973 (2003).

[212] Y. I. Alivov, J. E. Van Nostrand, D. C. Look, M. V. Chukichev and B. M. Ataev, "Observation of 430 nm electroluminescence from ZnO/GaN heterojunction light-emitting diodes", *Appl. Phys. Lett.* **83**, 2943 (2003).

[213] Y. I. Alivov, E. V. Kalinina, A. E. Cherenkov, D. C. Look, B. M. Ataev, A. K. Omaev, M. V. Chukichev and D. M. Bagnall, "Fabrication and characterization of *n*-ZnO/*p*-AlGaN heterojunction light-emitting diodes on 6H-SiC substrates", *Appl. Phys. Lett.* **83**, 4719 (2003).

[214] A. Osinsky, J. W. Dong, M. Z. Kauser, B. Hertog, A. M. Dabiran, P. P. Chow, S. J. Pearton, O. Lopatiuk and L. Chernyak, "MgZnO/AlGaN heterostructure light-emitting diodes", *Appl. Phys. Lett.* **85**, 4272 (2004).

[215] S. F. Chichibu, T. Ohmori, N. Shibata, T. Koyama and T. Onuma, "Greenish-white electroluminescence from *p*-type $CuGaS_2$ heterojunction diodes using *n*-type ZnO as an electron injector", *Appl. Phys. Lett.* **85**, 4403 (2004).

[216] D. J. Rogers, F. Hosseini Teherani, A. Yasan, K. Minder, P. Kung and M. Razeghi, "Electroluminescence at 375 nm from a ZnO/GaN: Mg/c-Al_2O_3 heterojunction light emitting diode", *Appl. Phys. Lett.* **88**, 141918 (2006).

[217] J. Nause and B. Nemeth, "Pressurized melt growth of ZnO boules", *Semicond. Sci. Technol.* **20**, S45 (2005).

[218] H. J. Ko, Y. F. Chen, S. K. Hong, H. Wenisch, T. Yao and D. C. Look, "Ga-doped ZnO films grown on GaN templates by plasma-assisted molecular-beam epitaxy", *Appl. Phys. Lett.* **77**, 3761 (2000).

[219] O. Lopatiuk-Tirpak, L. Chernyak, F. X. Xiu, J. L. Liu, S. Jang, F. Ren, S. J. Pearton, K. Gartsman, Y. Feldman, A. Osinsky and P. Chow, "Studies of minority carrier diffusion length increase in *p*-type ZnO:Sb", *J. Appl. Phys.* **100**, 086101 (2006).

[220] S. Guha, H. Cheng, M. A. Haase, J. M. Depuydt, J. Qiu, B. J. Wu and G. E. Hofler, "<100> dark line defect in II-VI blue-green emitters", *Appl. Phys. Lett.* **65**, 801 (1994).

[221] W. Guo, A. Allenic, Y. B. Chen, X. Q. Pan, Y. Che. Z. D. Hu and B. Liu, "Microstructure and properties of epitaxial antimony-doped *p*-type ZnO films", *Appl. Phys. Lett.* **90**, 242108 (2007).

[222] A. Nahhas, H. K. Kim, J. Blachere, "Epitaxial growth of ZnO films on Si substrates using an epitaxial GaN buffer", *Appl. Phys. Lett.* **78**, 1511 (2001).

[223] L. Wang, Y. Pu, Y. F. Chen, C. L. Mo, W. Q. Fang, C. B. Xiong, J. N. Dai, F. Y. Jiang, "MOCVD growth of ZnO films on Si(111) substrate using a thin AlN buffer layer", *J. Cryst. Growth* **284**, 459 (2005).

[224] X. N. Wang, Y. Wang, Z. X. Mei, J. Dong, Z. Q. Zeng, H. T. Yuan, T. C. Zhang, X. L. Du, J. F. Jia, Q. K. Xue, X. N. Zhang, Z. Zhang, Z. F. Li, W. Lu, "Low-temperature interface engineering for high-quality ZnO epitaxy on Si(111) substrate", *Appl. Phys. Lett.* **90**, 151912 (2007).

[225] W. Guo, A. Allenic, Y. B. Chen X. Q. Pan, W. Tian, C. Adamo and D. G. Schlom, "ZnO epitaxy on (111) Si substrates using intervening epitaxial Lu_2O_3 buffer layers", in press, (2008).

[226] C. Hammar and B. Magnusson, "Low field mobility in polar semiconductors", *Physica Scripta* **6**, 206 (1972).

[227] J. D. Wiley, "Mobility of holes in III-V compounds", in *Semiconductors and semimetals*, (Vol. 10, Academic Press, London, 1975, page 127).

[228] A. R. Hutson, "Piezoelectric scattering and phonon drag in ZnO and CdS", *J. Appl. Phys.* **32**, 2287 (1961).

[229] J. D. Wiley, "Mobility of holes in III-V compounds", in *Semiconductors and semimetals*, (Vol. 10, Academic Press, London, 1975, page 139).

[230] N. G. Weimann, L. F. Eastman, D. Doppalapudi, H. M. Ng and T. D. Moustakas, "Scattering of electrons at threading dislocation in GaN", *J. Appl. Phys.* **83**, 3656 (1998).